Study of the origin of HI asymmetries of the highly isolated galaxy CIG 96 by means of deep optical and HI observations.

UNIVERSIDAD
DE GRANADA

Pablo Ramírez Moreta

Advisors: Lourdes Verdes-Montenegro Atalaya, Stéphane Leon Tanne

Programa de Doctorado en Física y Matemáticas

Universidad de Granada

Instituto de Astrofísica de Andalucía (IAA−CSIC)

This dissertation is submitted for the degree of

Doctor of Philosophy

June 2018

Editor: Universidad de Granada. Tesis Doctorales
Autor: Pablo Ramírez Moreta
ISBN: 978-84-9163-977-0
URI: http://hdl.handle.net/10481/53152

Sin duda alguna, a mi madre y a mi padre.

Acknowledgements

Mi madre y mi padre son los auténticos responsables de que hoy yo pueda escribir estas líneas aquí, sin ningún matiz ni duda al respecto. Lo han sido desde hace mucho tiempo, más del que ha llevado hacer esta tesis. Son, sin duda, las raíces invisibles que, incondicional e incansablemente, han nutrido el tallo, las ramas y las hojas del metafórico árbol que soy hoy en día. De una forma paralela, también son responsables de que haya llegado hasta aquí unas pocas personas más. Mi hermana Alicia que, aun estando casi todo este tiempo a $\sim 7700 \pm 500\,\mathrm{km}$ de distancia junto a mi cuñado Sameer, sé que me ha/han apoyado a tope desde el primer hasta el último momento y la distancia no ha hecho que se notara menos. Clara, quien, literalmente a diario, con una fuerza inagotable, sin flaquear ni un solo día y de forma totalmente sincera e incondicional, ha estado a mi lado en todo buen momento y, en especial, en los no tan buenos, en los que me ha tolerado, tranquilizado, querido y ayudado cuando más lo necesitaba. Y María, una escudera en los tiempos difíciles que me ha enseñado a usar la espada de nuevo. Nunca sabréis del todo lo mucho que cada uno de vosotros, cada una de vosotras, habéis hecho por mí. Esta tesis es tan mía como vuestra.

La amistad, las risas, el cariño y el apoyo diario e incondicional de mis amigos y amigas del IAA (en su mayor parte) desde hace tanto tiempo les ha convertido a todos en personas −cada una a su manera− fundamentales para que yo haya llegado hasta aquí. Huelga decir que son lo mejor que me ha ofrecido Granada en este tiempo, además de las tapas y los shawarmas. Víctor, Alba, Ark, Laura, Darío, Mirian, Pedro (¡sus canijos!), Ana Karla, Jesús, Marta, Javi, Pique, Isa, Manu, Stef, Antonio, Angela, Fran, Naím, Ancor, Maia, René y varios más que seguro me dejo, gracias por tanto y por tantas cosas, gracias, gracias y gracias.

Alejados del IAA pero muy cercanos en otros ámbitos, también hay personas que me han acompañado y que han puesto su granito de arena en esta tesis − o incluso más que un granito. Entre ellos están mis amigos de armas (Pedro, Fer, Fran, Antonio, Ale, Antoñico, Laura, Enrique...), mis amigos jugones y roleros (Cris − autora de la preciosa cubierta de la tesis, Álvaro, Renata, Dani, Ana, Enrique, Nono, Rosana, Jose, Raquel...), La Vida Moderna y el extinto estado mental de Moderdonia, mis amigos 'de la biblio' (Carlos, Feri, David, Premu, Víctor, Chavo, Fusta, Borja y Alvarito) y, por supuesto, mis amigos de siempre, 'los de Majadahonda', los de '*quedamos en el 9*' (Pablo, Gustavo, Jorge, Dani, Íñigo, e Isma). Gracias a todos por haber estado y estar ahí.

No puedo terminar sin agradecer al personal del IAA, a los miembros de mi grupo de investigación (Jack, Susana, Julián, Mike, Marina y Juande), y a los colaboradores 'lejanos' (Aku y Min, entre otros). Por último, en especial, agradezco a mis directores de tesis todo lo que me han ofrecido, enseñado y proporcionado a lo largo de estos años. Son co−responsables de que yo haya conseguido llegar hasta aquí. Gracias por tantas y tantas cosas, gracias por todo.

Abstract

Throughout the years, many studies have addressed the numerous questions raised when trying to understand how the galaxies assemble and evolve. This topic constitutes one of the most studied fields of modern astronomy and, as we expand our knowledge of the different elements of a galaxy and their evolutionary roles, new problems arise. Some of them may be solved with deeper and higher resolution observations that let us detect the fine print of the processes shown in the different evolutionary stages. The Analysis of the interstellar Medium of Isolated GAlaxies project (AMIGA) seeks to provide a better understanding on the formation and evolution of galaxies focusing on those that lie in relatively uninhabited environments in comparison with denser ones, including the field galaxies. AMIGA has been performing a systematic multi−wavelength study of a selected and statistically significant sample of extremely isolated galaxies based on a refined version of the Catalog of Isolated Galaxies (CIG). In absence of companions, the CIG galaxies constitute an ideal laboratory to study secular evolution and. Since the foundation, the AMIGA project has been investigating the internal and environmental processes of these galaxies, as well as the implication in the theories of galaxy formation and evolution. This project constitutes the framework for the present dissertation. Asymmetries in the atomic hydrogen (HI) of galaxies are often caused by the interaction with close companions. The AMIGA project has demonstrated that isolated galaxies show the lowest levels of asymmetry in their HI integrated profiles compared to other samples, even field galaxies. However, some galaxies present high asymmetry ratios whose origins are poorly understood. Aiming to investigate the source of the asymmetries, we selected a sample that consists of 184 isolated galaxies from the CIG catalog. Out of them, the highly isolated galaxy CIG 96 (NGC 864) shows a 16% asymmetry level in its HI integrated profile, representing a model case and main target of this study. In order to try to reveal the causes of the asymmetry, we performed

deep optical observations of CIG 96 with the CAHA1.23m, CAHA2.2m and VST (with the OmegaCAM wide field camera) telescopes. We reach surface brightness limits of $\mu_{CAHA2.2m} = 27.5\,\mathrm{mag\,arcsec^{-2}}$ (Cousins R) and $\mu_{VST} = 28.7\,\mathrm{mag\,arcsec^{-2}}$ (SDSS r) that show the pseudoring of the galaxy and its star forming regions in detail. Additionally, a wavelet filtering of the HI data cube from our deep observations with VLA/EVLA telescope allowed us to reach a column density of $N_{HI} = 8.9 \times 10^{18}\,\mathrm{cm^{-2}}$ (5σ, 28" × 28" beam), the lowest of any isolated galaxy to date. We confirm that the HI extends farther than $4 \times r_{25}$ in all directions and also detect two previously undetected gaseous structures ($\sim 10^6\,M_\odot$) in the outskirts of the galaxy. The SDSS $g-r$ colour index image from CAHA1.23m shows extremely blue colours in certain regions of the pseudoring (suggesting regions with star formation) where $N_{HI} > 8.5 \times 10^{20}\,\mathrm{cm^{-2}}$, whereas the rest show red colours. Galactic cirrus contaminate some regions of the field, setting an unavoidable detection limit at $28.5\,\mathrm{mag\,arcsec^{-2}}$ (SDSS r). At the current surface brightness (SB) and HI column density (N_{HI}) limit levels, we detect no stellar link within 1°×1° neither gaseous link within 40'×40' between CIG 96 and any companion. The isolation criteria rule out interactions with other similar sized galaxies for at least ∼2.7 Gyr. Using existing stellar evolution models, the age of the pseudoring is estimated to be 1 Gyr or older. Undetected companions previously accreted and cold gas accretion remain as the main hypothesis to explain its optical pseudoring and HI features. The deep optical and HI observations have let us unveil previously undetected features of CIG 96, showing they are a key tool for the study of the HI distribution asymmetry and their causes in isolated galaxies. Hence, all the deep optical data of CIG 96 and other targets presented in this dissertation guarantee the continuation of the project, they may potentially open new research paths within the AMIGA project and, in the end, help us to expand our knowledge on galaxy formation and evolution.

Table of contents

List of figures

List of tables

Nomenclature

$\mathcal{A}_{1/h}$	Asymmetry parameter, see Sect. 2.2.1.
A13	Abbreviation of Argudo-Fernández et al. (2013).
AMIGA	Analysis of the Interstellar Medium of Isolated Galaxies.
CAHA	Centro Astronómico Hispano-Alemán, Calar Alto Observatory (MPIA-CSIC).
CIG	Catalog of Isolated Galaxies.
E05	Abbreviation of Espada et al. (2005).
E11a	Abbreviation of Espada et al. (2011a).
E11b	Abbreviation of Espada et al. (2011b).
EVLA	Extended-Very Large Array (NRAO Karl G. Jansky Very Large Array Observatory).
FUV / NUV	Near and Far Ultraviolet.
HI	Atomic hydrogen.
INT	Isaac Newton Telescope (ING).
MS	Measurement Set of the interferometric data, see Sect.3.1.2.
NOT	Nordic Optical Telescope.
OLR	Outer Lindblad Resonance.

OR	Outer Rings
PA	Position Angle.
Planck857	Planck image at 857 GHz.
Pseudoring	Partial XUV ring of CIG 96 with SF regions.
SB	Surface brightness.
SF	Star Formation.
SFE	Star Formation Efficiency.
SFH	Star Formation History.
SFR	Star Formation Rate.
SNR	Signal−to−noise ratio.
UV	Ultraviolet.
V07	Abbreviation of Verley et al. (2007c).
VLA	Very Large Array (NRAO Karl G. Jansky Very Large Array Observatory).
VST	VLT Survey Telescope (ESO).
WISE3	WISE image at 12 μm, band 3.
XUV	Extended Ultraviolet (in reference to the disc or pseudoring of CIG 96).

Chapter 1

Introduction

The formation and evolution of galaxies constitutes one of the most studied fields of modern astronomy. The current approaches do not agree on a single explanation for many of the physical phenomena that take place in the galaxies. In this situation, deeper insights are necessary to provide answers to the pending questions, to find out the true implication of the different factors and to narrow down the possibilities towards a common theory that helps us get a better understanding of our Universe.

1.1 General considerations

Galaxies are celestial bodies composed of stars, gas, dust, radiation and dark matter. They carry a massive amount of information from different epochs of the Universe that can help us develop our knowledge of the Universe itself. For instance, they keep footprints of many physical events that take place within them, such as the life cycles of the stars or the interactions with other galaxies. Also, they have let us −indirectly− detect the gravitational interaction between the baryonic matter and the dark matter that, as far as we know, carries no electromagnetic signature. In a wider spatial range, galaxies are the minimum units in which the Large Scale Structure (or LSS) of the Universe is arranged.

Understanding how galaxies assemble and evolve is a topic that has motivated a long and dynamical debate for decades. The discussion has been developing throughout the last century along with the improvement of the technical and theoretical constraints. Both are interlaced in such a way that the improvement of one constantly challenges the update of the other. The capabilities of the observatories and their instrumentation are in constant development. Moreover, the exponential growth of the computational power has drastically shortened the time necessary for the massive calculations that accurate numerical simulations demand. By receiving constant feedback from the observations, the simulations are necessary in order to build stable models capable of providing a physical explanation and, in consequence, to elaborate reliable theories on how the galaxies behave and evolve. Up to date, models keep demanding further observational studies to confirm −or reject− the theoretical predictions. No theoretical consensus has been found yet, but the closely entwined action between observations and models is pushing forward the advances on the current and new theories that aim to explain how the galaxy form and evolve.

1.1.1 Open questions and state of the art

Throughout the years, many studies have addressed the numerous questions raised when trying to understand galaxy evolution. For instance, how the density of galaxies and their star formation (hereafter SF) have changed with time, what processes lead to the formation of lenticular galaxies, for how long galaxies manage to retain their morphology, whether or not the elliptical galaxies are an evolved stage of old spiral galaxies, where is the missing population of dwarf galaxies, among many other.

Addressing these evolutionary questions demands an extensive knowledge of the structural aspects that, in most cases, are still being studied. The processes of SF, the distribution of the gas, the effects of supernovae in the surrounding environment, the dynamical effects of arms, bars or bulges, to name a few, are all open questions that the theories of galaxy evolution depend on. Additionally, as explained in detail in Sect. 1.2, the environment of a galaxy may also heavily affect the evolution in both a local or a global scale by adding or removing gas, enhancing or quenching the SF, breaking or creating structural features like rings or even disrupting the whole galaxy. Together,

the structural and environmental characteristics are key factors for the evolution of the galaxies.

However, the usually unique conditions of each galaxy may assign different weight to the agents involved, i.e. the same physical effects may come from different sources, entangling them and complicating the discussion. For instance, the formation mechanisms proposed for lenticular (S0) galaxies are as different as the collapse of the bar of a spiral galaxy (Davidge, 2015), the merger of satellite galaxies (Katkov et al., 2016) or extremely old mergers (Tapia et al., 2017). As another example, the outskirts of many galaxies present regions with high concentrations of stars, even SF regions, but their origin can be explained by very different effects like the stellar migration from transient spiral arms (Sellwood and Binney, 2002), or the accretion of gas and stars from dwarf galaxies with similar angular momentum forming warps (Binney, 1992) at the 'proto-disc' of the galaxy (Bland-Hawthorn et al., 2017), or in−situ formation out of gas clouds with longer depletion times, or a mix of all of them (Sellwood and Binney, 2002; Cormier et al., 2016; J. Zhang et al., 2018). To explain the assembly of galaxies, an agreement between the monolithic collapse (Eggen et al., 1962) or hierarchical model (White and Rees, 1978) is still to be found. In terms of evolution, many candidate drivers have been proposed in different works throughout the years by using both observations and simulations. Whether the primitive conditions of the galaxies lead their evolution ('nature') or the environmental effects are the dominant drivers instead ('nurture') (Irwin, 1995), or even a combination of both effects, it is still an open discussion with no consensus so far (e.g. White, 1983; Mateus et al., 2007; Athanassoula, 2010; Annibali et al., 2011; Niemi, 2011; Jones et al., 2018).

In order to investigate how galaxies evolve it is necessary to have a precise classification. The first step in this regard was taken by Hubble (1926), who proposed the morphological classification of galaxies, later synthesised in the Tuning Fork diagram (Hubble, 1936; Sandage, 1961). In the following decades, the classification of galaxies was expanded with the growing number of observations of close and more distant objects that have allowed a more precise detection of relevant dynamical elements like the rotation speed of the early−type galaxies or ETG (slow or fast rotators) or the arms, rings or bars of spiral galaxies. For instance, the dynamical structure of the spiral galaxies was demonstrated later by C. C. Lin and Shu (1964), who proposed

that the stars and gas can maintain a density wave through gravitational interaction along the disc of a galaxy with differential rotation, i.e. the density wave provides an underlying and stable spiral gravitational field so the matter can be arranged accordingly throughout the whole disc and form the spiral pattern of the late−type galaxies. Moreover, the bars present in nearly two−thirds of the spiral galaxies (e.g. Buta et al. 2015), whether initially from external or internal origin, are among the inner structures that can crucially affect the evolution of the galaxy via the bar−disc redistribution of the angular momentum (Little and Carlberg, 1991; Athanassoula, 2013), i.e. from their bulges or pseudobulges out to the outer bulge stars, the spiral structure, resonances or halos (e.g. Athanassoula, 2003; Kormendy and Kennicutt, 2004; Buta et al., 2005). Hence, these elements have been included to refine the galaxy classification in further schemes (e.g. de Vaucouleurs, 1959; Sandage et al., 1975; Buta, 2013).

Other aspects like the positions where the star forming regions appear or the changes in the star formation rates (hereafter SFR) constitute key aspects to understand how galaxies formed and evolved. Currently, galaxies are being studied in a wide range of redshifts (z) that spans back to the early Universe at $z \sim 8-11$ (see Fig. 1.1), where the findings of the first candidate galaxies after the reionisation epoch have been reported (Oesch et al., 2016; Salmon et al., 2018).

The observations reveal that the galaxies at the highest redshifts are generally smaller, of irregular and peculiar morphology and undergo high SFR that grew to peak in later stages between $2 < z < 4$ (Shapley, 2011). At $z \sim 2$, active ($SFR > 100 M_{\odot} yr^{-1}$) galaxies of high stellar mass ($M > 10^{11} M_{\odot}$) are found coexisting with passive evolved galaxies (approximately 50% of the current stars were born at $z < 1.3$). The latter are undergoing very little SF (P. G. van Dokkum et al., 2008) and they constituted a red sequence of massive field galaxies that would account for the evolved galaxies we see today. In the usually quiescent galaxies of the nearby Universe ($z < 0.3$), galaxies of all morphological types are found yet the SFR have strongly decreased to reach densities close to those found at $z \sim 7$. Among those galaxies more luminous than $M_B =$ -20, about 75% are spirals (late−types), 22% are lenticular and elliptical (early−types) and only 2% are irregular or peculiar (q.v. Blanton and Moustakas 2009 and Conselice 2014). In other words, it is necessary to trace back the star formation history (hereafter

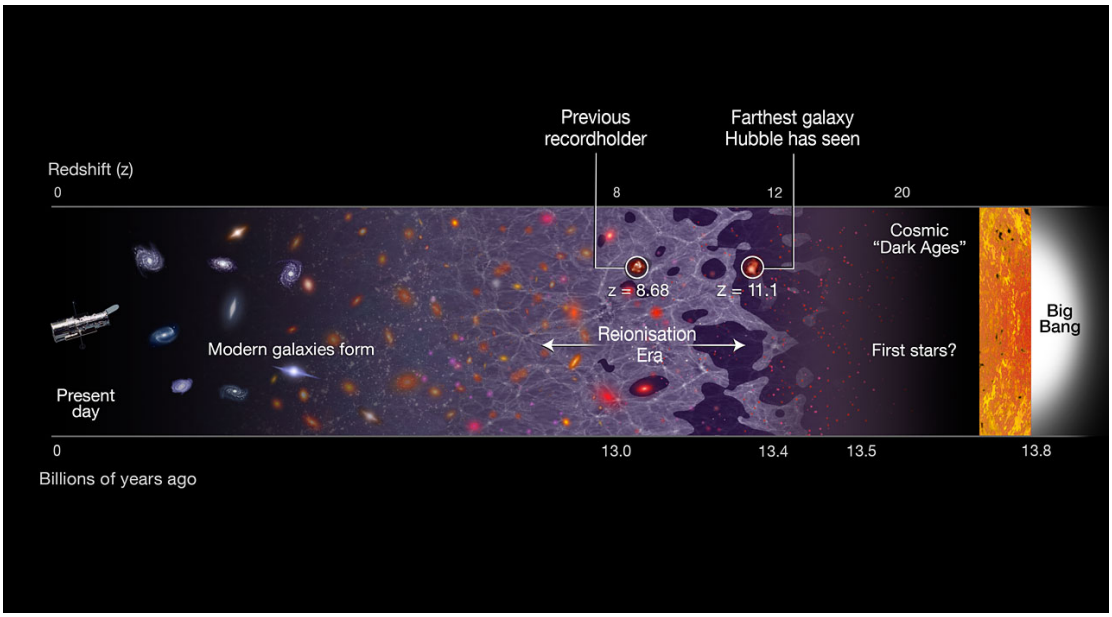

Fig. 1.1 Timeline of the Universe. Copyright: NASA, ESA, and A. Feild (STScI).

SFH) and the morphological patterns followed by the galaxies throughout the different cosmological stages in order to elaborate a comprehensive theory of the evolution of galaxies.

Currently, the observational strategies of galaxies may arguably be divided into three wide categories: specific targets, surveys and samples selected with a specific criterion or set of criteria. The visions provided by each one, either the targeted observations or larger samples with or without selection criteria, are fully complementary.

The targeted observations are those that focus on a specific galaxy and, usually, provide a deep insight of one or a number of the particular stellar, gaseous, chemical, morphological or dynamical characteristics. The state−of−the−art with respect to observations of single targets is probably too extensive as to name just a few examples but, in the context of this work, the deep observations of galaxies in different bands have produced remarkable results in the last few years, like the discoveries of numerous ultra diffuse galaxies (UDF), faint gaseous and stellar tidal tails or structures previously hidden. The results of the deep optical observations are commented further in Sect. 1.1.2.

The surveys aim to gather complete samples by covering large areas of the sky and to offer a statistical approach. Many already settled surveys and missions in different wavelengths have established a fundamental framework for most of the astronomical discoveries in the last decades. In terms of relevance for extragalactic studies, we find numerous examples; here we mention a few in the optical, infrared and radio wavelengths. In the optical range, for instance, we find the Sloan Digital Sky Survey (SDSS, York et al. 2000) up to the latest data release DR14 (Abolfathi et al., 2018), the LSS observations of the 2−degree Field (2dF, Colless et al. 2001), the Calar Alto Legacy Integral Field Area Survey in the optical (CALIFA, Sánchez et al. 2012), the Pan-Andromeda Archaeological Survey (PAndAS, e.g. Crnojević et al. 2014; Martin et al. 2016, 2017, among others) of M31 and the companions, the Dark Energy Survey (DES, The Dark Energy Survey Collaboration 2005) or the VIMOS-VLT Deep Survey of galaxies at $z \sim 6-7$ (VVDS, Ilbert et al. 2005), among others brought by the Very Large Telescope (VLT, ESO), to name just a few. In the infrared (IR), there are surveys of remarkable relevance like the 2−micron All−Sky Survey (2MASS, Skrutskie et al. 1997) and its high precision and dynamic range (over 20 magnitudes) and key wide sky coverage, the deep wide and narrow band ULTRA-VISTA survey (McCracken et al., 2012) of the Visible and Infrared Survey Telescope for Astronomy (VISTA, ESO), as well as space missions like Herschel (former FIRST) (Pilbratt, 2003), Spitzer (Werner et al., 2004) or the Planck mission (Planck Collaboration et al., 2014) that have been and still are of capital relevance in this wavelength. For instance, the full sky coverage of Planck mission in four bands has brought up new insights on the the Hubble constant and the age of the Universe (Planck Collaboration et al., 2016). In centimeter, millimeter and submillimeter wavelengths, many single−dish, interferometers and other telescopes have powered large surveys. Currently, in the milimeter and submilimeter range, some state−of−the−art ground based interferometers are performing surveys studying the formation, evolution and properties of the protoplanetary disks (Ansdell et al., 2018) and galaxy evolution in COSMOS fields (Brisbin et al., 2017) with the Atacama Large Millimeter/submillimeter Array (ALMA, ESO) and studying the star forming histories and gas fractions of galaxies from z =1−3 in the IRAM Plateau de Bure HIgh-z Blue Sequence Survey (PHIBSS, Tacconi et al. 2013) with the IRAM Northern Extended Millimeter Array (IRAM, PdBI-NOEMA), to mention a few. In the centimeter and larger wavelengths, the KSP or multi−purpose key science projects

(star formation in the early Universe, galaxy formation, intercluster magnetic fields, etc.) to be obtained with the Low-Frequency Array (LOFAR, Astron), the Green Bank Ammonia Survey (GAS, Friesen et al. 2017) with the Green Bank telescope (GBT), the Effelsberg Bonn HI all−sky survey (EBHIS, Winkel et al. 2016) which aims to perform a blind survey of the Milky Way HI distribution with the 100 m Effelsberg telescope, the Arecibo Legacy Fast ALFA Survey in the HI line at 21 cm (ALFALFA, Giovanelli et al. 2005) with the Arecibo telescope (NAIC, UMET and USRA), the NRAO VLA Sky Survey for continuum at 1.4 GHz (NVSS, Condon et al. 1998), the HI Nearby Galaxy Survey in the 21 cm line (THINGS, Walter et al. 2008), the Continuum Halos in Nearby Galaxies: An EVLA Survey (CHANG-ES, Irwin et al. 2012), the COSMOS HI Large Extragalactic Survey (CHILES, X. Fernández et al. 2013), or the more recent Karl G. Jansky Very Large Array Sky Survey (VLASS, Myers et al. 2014) with the NRAO Very Large Array (VLA), among other present and future surveys to be performed with the Square Kilometer Array (SKA, q.v. Bourke et al. 2015; Perez-Torres et al. 2015, for reference), soon to be built.

The samples built upon the specific selection of their targets with physical criteria may provide particular and statistical results of certain scientific problems or characteristics shared by their members. For instance, two state−of−the−art projects working with selected samples in the nearby Universe are the multiwavelength ATLAS^{3D} project (Cappellari et al., 2011), that focuses on the study of a selected sample of ETG in the radio, infrared and optical wavelengths and the AMIGA project, a multiwavelength study of a large sample of highly isolated galaxies selected with physical parameters that define the environment. This dissertation is part of the latter and the role of the environment and the project are discussed further in Sect. 1.2) and 2.1.

1.1.2 Deep optical observations of galaxies

The more we understand about the different elements of a galaxy and their roles on the evolution, the more questions are raised. Some of them may be answered with more numerous, precise, detailed and demanding observations, i.e. deeper and higher resolution observations that let us see farther as well as the fine print of the processes shown by the different evolutionary stages. The Hubble Deep Field and

Hubble Ultra-Deep Field (HDF and HUDF, Williams et al., 1996; Beckwith et al., 2006, respectively) constitute two flagship deep observations. The implications of the HDF showing a large number of young galaxies in an also young Universe had a profound impact on the discussion of galaxy formation and evolution (e.g. Madau et al., 1996; Connolly et al., 1997; Phillips et al., 1997; Hughes et al., 1998, among many others), representing one of the most relevant breakthroughs in modern cosmology.

Concerning the study of galaxy evolution in the nearby Universe in the optical range, some particular observations and surveys are showing impressive new images and results by taking the current instruments to the limit. The pioneering works of de Vaucouleurs (1958) with M31 (reaching a surface brightness, μ or SB, fainter than $\mu_B \simeq 25 \mathrm{mag\,arcsec^{-2}}$) and Freeman (1970) initially traced the exponential decline of the radial surface brightness of the disks of spirals and lenticulars (q.v. Pohlen et al., 2002, and references therein). With moderate aperture optical telescopes, Martínez-Delgado et al. (2008, 2009, 2010, 2012, 2015) have shown very faint ($\mu_{CousR} = 27.2\,\mathrm{mag\,arcsec^{-2}}$, $\mu_{SDSSg} = 27.5\,\mathrm{mag\,arcsec^{-2}}$) stellar tidal streams around some individual galaxies interacting with their close or small neighbours. The deep observations of some galaxies included in the ATLAS^{3D} survey by Duc et al. (2015) have also shown stellar structures in detail, reaching surface brightness levels of $\mu_{SDSSg} = 28.5\,\mathrm{mag\,arcsec^{-2}}$. The images obtained with the Dragonfly Telephoto array (Abraham and P. G. van Dokkum, 2014), much cheaper and smaller than large telescopes, have reached remarkably faint surface brightness in different projects, e.g. the detection of four Ultra Diffuse Galaxies (UDG) around the elliptical galaxy NGC 5485 by Merritt et al. (2016) at $\mu_{SDSSg} = 27.7\,\mathrm{mag\,arcsec^{-2}}$, or the 47 extremely diffuse galaxies detected in the Coma cluster down to $\mu_{SDSSg} = 27.7\,\mathrm{mag\,arcsec^{-2}}$ by P. G. van Dokkum et al. (2015), to name a few. Agulli et al. (2016) and Aguerri et al. (2017) have studied the Abell 85 and Hercules clusters of galaxies with deep spectroscopic data (reaching μ_{SDSSr} of 24 and 23 $\mathrm{mag\,arcsec^{-2}}$, respectively), namely the luminosity function, the star formation and the orbital structure of the galaxies. Iodice et al. (2017) have reached a surface brightness of $\mu_{SDSSg} = 30\,\mathrm{mag\,arcsec^{-2}}$ by studying the stellar formation in the halo of NGC 1316 with VLT Survey Telescope (VST, ESO). Trujillo and Fliri (2016) have reached the extremely faint surface brightness of $\mu_{SDSSr} = 31.5$ mag arcsec^{-2} with the Gran Telescopio de Canarias (GTC) and more lately, Trujillo et al. (2017) have detected the nearest UDG to the Milky Way named UGC 2162, with a surface brightness of

$\mu_{SDSSg} = 24.4$ mag arcsec^{-2}, as well as more detailed characteristics with ultra deep imaging from the IAC Stripe82 Legacy Project (Fliri and Trujillo, 2016).

All the previous works, from the first ones to the latest state−of−the−art projects, have reached very faint surface brightness levels, managing to observe extremely faint structures in or around the studied galaxies. In general, they all share one common observational characteristic: performing deep observations of their targets to find the faint structures. Although the large telescopes may reach deep surface brightness levels faster than the smaller ones, most of the deep observations demand large observation times. However, unveiling previously hidden interactions, structures or characteristics of the galaxies, have proved to be results of high impact. In consequence, deep observations have demonstrated to be a key tool to help us improve our understanding of how galaxies interact and evolve in their particular environments, as explained in Sect. 1.2.

1.1.3 HI observations in galaxies.

The atomic hydrogen or atomic gas (hereafter HI) is the most abundant hydrogen phase in the Universe. The HI emission line can be detected in the radio wavelengths, specifically at 1.42 GHz or 21 cm wavelength, in the L−band of the microwaves. It is produced when a photon of this frequency is emitted after the spin of the electron switches the orientation from parallel to antiparallel with respect to the proton. This forbidden transition between two hyperfine levels of the hydrogen is also called $spin-flip$ transition, and it has a very low spontaneous rate of 2.87×10^{-15} s^{-1} and mean lifetime of the excited state of $\sim$ 10−11 Myr. Despite the very low transition rate, the large abundance of HI makes the detection of the faint 21 cm line feasible with the adequate detectors. Aiming to study intercontinental communication interferences, Karl G. Jansky unintentionally detected HI emission coming of the center of our galaxy in the decade of 1930 − as confirmed later by Ewen and Purcell (1951). The potential of this emission was soon understood and the scientists started to perform the first systematic observations in the decades of 1940 and 1950. From the first rudimentary antennas up to the current interferometers and single−dish telescopes as those mentioned in Sect. 1.1.1, the study of HI has become a fundamental part of modern astronomy.

The usually HI rich late−type (spiral) galaxies have centered the main observational efforts. Today, we know the HI is distributed along the same plane as the disc. However, it can be extended several times the Holmberg radius (Banerjee et al., 2013). The HI usually shows higher concentration in the spiral arms, lower densities in the bulges, and it let us trace the dark matter distribution (Bosma, 2017). These galaxies may show warps in the outermost regions (Sancisi, 1976), i.e. inclinations of the gas disc with respect to the optical disc may bend up to 20% as in the case of NGC 5907. The HI is highly sensitive to perturbations so it is considered as one of the main tracers of interactions between galaxies and the surrounding environment.

In comparison to the spirals, the HI in early−type (elliptical) galaxies has only been studied recently. These galaxies are generally devoid of HI gas with the exception of about ∼15% of them (Huchtmeier, 1994). Knapp et al. (1985) found that the in principle unexpected gas of these galaxies has an external origin, product of possible cannibalisation of other gas−rich galaxies or the accretion of intramedium gas. Current studies of the HI in early−type galaxies like ATLAS^{3D} collaboration discuss the gas distribution, kinematics, star formation and implications on the formation and evolutionary scenarios of ETG (Serra et al., 2010, 2012, 2014; Davis et al., 2014, among others.).

The formation of lenticular galaxies is still under discussion but they show the same central low HI densities as in the spirals, forming ringed HI distributions that in occasions manage to form stars (Thilker et al., 2010), yet the gas probably has an external origin as it usually happens with the elliptical galaxies (del Río et al., 2004).

The irregular galaxies have an also irregular distribution of the HI, as it happens with the rest of their structural components. The origin of the gas is a tricky question due to the particular origins of these galaxies − not always known. While in some occasions the irregular galaxies are relatively isolated and their HI does not show direct connection to other sources (Hunter et al., 2018), the large HI envelopes are usually associated to an interaction with the environment (Ashley et al., 2017), such as a nearby companion, advanced mergers or accretion of gas from the intergalactic medium (Ashley et al., 2014).

In this dissertation, the main interest of the HI resides in how it can help tracing regions of star formation located in the outskirts and, specially, in the high sensitivity of HI to environmental effects, that place it as a privileged tracer of interactions that may be barely detectable in other wavelengths. This is of special relevance considering the low density environments associated to highly isolated galaxies (see Sect. 1.2).

1.2 The role of the environment.

The LSS of Universe delineates two types of structures, voids and filaments, and their discovery (Gregory and Thompson, 1978) meant a landmark in cosmological studies. The voids are large regions in space ($10^4 - 10^6\,\mathrm{Mpc}^3$) almost devoid of galaxies when compared to the filaments. The latter are the largest structures known, they contain much larger concentrations of galaxies that surround and set the spatial limits of the voids (q.v. the maps up to $z \sim 0.25$ from 2dF or the Millenium Simulation Project Colless et al., 2001; Springel et al., 2005, respectively).

The Λ-Cold Dark Matter (ΛCDM) model predicts that the galaxies in the Universe follow a hierarchical structure. Most of the galaxies are distributed in associations of different size and number of components and the bulk of LSS is composed of groups of galaxies according to simulations (Jenkins et al., 2001). This is also the case for the nearby Universe, where approximately half of the galaxies are found in groups or clusters (Geller and Huchra, 1983; Eke et al., 2004). The groups are associations that approximately contain no more than 50 members located within distances of $\sim$2 Mpc or less. The clusters of galaxies are composed from dozens up to thousands of galaxies that are gravitationally bound in much larger volumes; this implies that the dark matter accounts for $\sim$ 90% of the total mass while galaxies are only $\sim$1% and intracluster gas $\sim$9%. In turn, the superclusters contain all the former, individual, groups and clusters of galaxies, and are displayed as the filaments that surround the voids. In the context of the current dissertation, the most relevant structures of the hierarchical distribution are the groups of galaxies and, specially, the isolated galaxies.

The environment that surrounds every galaxy is a key factor to consider when evaluating the galaxy ageing and evolution as it may have a critical role. In the case of the nearby galaxies, they are usually gravitationally bound to or directly interacting with the neighbours located within distances that may go from a few kiloparsec (kpc) up to a few hundred kpc. These environmental events may have deep implications in the evolution of structural, dynamical and chemical characteristics of the galaxies involved.

There is a special case among the groups of galaxies, the Hickson Compact Groups (HCG, Hickson 1982 and subsequent publications). They are a special kind of compact groups (CG) defined with three parameters: one, the population (4 or more members within 3 mag of the brightest); two, their compactness (the total brightness must be below 26mag arcsec^{-2}) and, three, a specific isolation (they must have a circular region containing at least 3 times their averaged total brightness of the members and no external galaxy of such magnitude or brighter). The HCG have some remarkable characteristics, for instance, their possible formation in low galaxy density regions (Palumbo et al., 1995) or their HI deficiency (Verdes-Montenegro et al., 2001; Borthakur et al., 2010). Also, the constant interaction between the members may have different effects, e.g. the transition from active to quiescent SF (Alatalo et al., 2015), shocks and turbulence (Bitsakis et al., 2016) and a decrease in molecular gas (Lisenfeld et al., 2017), among others. In other words, the evolution of an individual galaxy belonging to a HCG is constantly affected and heavily dominated by the rest of the members of the group and the intragroup medium of the CG.

On the contrary to the previous scenario, field galaxies have a loose definition that may be outlined as those that do not belong to any other classification, i.e. those not located in CG, groups, clusters (Madau et al., 1998). However, this environmental difference does not exclude one−on−one interactions, for example. Since they have an open definition, barely no selection criteria for field galaxies are applied (e.g. Silva and Bothun, 1998; Pisano et al., 2002; P. G. van Dokkum, 2005; Klypin et al., 2015, to mention a few) so they cannot be intrinsically considered a defined sample of galaxies.

There is a more extreme case in terms of environmental classification: the isolated galaxies. Strictly speaking, there is no such thing as a fully isolated galaxy in the Universe since every one has their first neighbour within a volume of a certain radius.

However, it is possible to refer to a certain level of isolation in terms of distance to the neighbours and to their gravitational influence. Ideally, the isolated galaxies should have no close companions that may interfere with their evolution. Unlike other samples, the isolated galaxies offer the possibility of studying the secular evolutionary stages of galaxies unperturbed for several Gyr. In order to achieve this, it is mandatory to define robust criteria that consistently establish a satisfactory frame in which galaxies can be considered in isolation with the corresponding physical implications. This extreme environment apparently has very low influence on the lone galaxy, who is devoid of major companions. Moreover, the environment may vary depending on how the isolation is defined. However, the former characteristics raise some straightforward questions: are there any external mechanisms taking active part in the evolution of these galaxies? Are there any observational signatures that suggest past interactions between an isolated galaxy and elements of its environment? Do the internal processes prevail over the environmental effects in terms of dominating evolutionary mechanisms or is it the opposite?

There are several state−of−the−art projects focused on studying galaxies in different environments and at different z that aim to answer the previous questions. Most of them rely on precise observational data from either particular galaxies, surveys or selected samples. Some of these works apply different environmental constraints to their samples so the discussions include the effects of different levels of isolation.

Focusing in the galaxies of the nearby Universe, where the scope of this dissertation is, we may find several large collaborations and surveys of various spectral ranges. For instance, the previously mentioned multiwavelength ATLAS^{3D} project is focused on improving the global understanding of 263 ETG within the local volume (42 Mpc). Their results often consider the environmental situation of the sample, for instance, when discussing the evolution of the initial mass function (IMF, Clauwens et al. 2015), the stellar populations properties (N. Scott et al., 2013; McDermid et al., 2015), the morphological changes due to external structures (Duc et al., 2015) or the dependence of the HI properties with the environment (Serra et al., 2010). In this last work, the authors find HI in about half of the ETG outside Virgo cluster and how it changes with different environments, being more regular in the most isolated cases and more disturbed in groups, to find barely no HI in those objects inside the Virgo cluster.

The THINGS survey, previously mentioned too, consists of 34 nearby galaxies that are a subset of the Spitzer Infrared Nearby Galaxy Survey project (SINGS, Kennicutt et al. 2003). The HI data were obtained using the VLA interferometer providing observations of nearby galaxies with a high spatial and velocity resolution (∼7" and below $5.2\,\mathrm{km\,s^{-1}}$, respectively) as well as integrated profiles, rotation curves, HI masses, among others. One of the main implications of the environment in this survey has come as another survey, the Local Irregulars That Trace Luminosity Extremes survey (LITTLE THINGS Hunter et al. 2012). This related project has investigated the star formation in dwarf galaxies and searched for previously unknown optical companions with small telescopes (up to surface brightness levels of $\mu_V = 28.3\,\mathrm{mag\,arcsec^{-2}}$), aiming to inspect possible interactions with the host galaxies, considered fairly isolated (Hunter et al., 2018). The Mapping Nearby Galaxies at Apache Point Observatory (MaNGA, Bundy et al. 2015), the already mentioned CALIFA project or the Spitzer Survey of Stellar Structure in Galaxies in the infrared/μm (S4G, Sheth et al. 2010) are also notable examples of large samples of nearby galaxies. MaNGA is an integral field spectroscopic survey built to investigate the internal kinematic structure and composition of gas and stars of about 10000 galaxies with different environments. A recent study by Lee et al. (2018) of 1830 galaxies from the sample suggests that the large−scale environments hardly affect the galaxy spin (predicted by the tidal−torque theory or TTT, Peebles 1969) in both early and late−type galaxies; however, the small-scale environments such as hydrodynamic interactions with neighbour galaxies can also play a substantial role in determining galaxy spin. CALIFA mainly focuses on studying the kinematical classification of galaxies, the interstellar medium (ISM) over entire galaxies, stellar populations and metallicities, with the largest wide-field integral field unit (IFU) survey of galaxies to date. It consists of ∼600 galaxies of the local Universe ($z = 0.05 - 0.3$) with no specific environmental restrictions. Among the many results of the project, they show that the SFR and SFH can be affected by dynamical and morphological characteristics of the galaxies (e.g. Holmes et al., 2015; Gomes et al., 2016; L. Lin et al., 2017; Levy et al., 2018, among others) which, in some cases, are closely related to their environment. S4G, for its part, mainly focuses on studying the distribution of mass and stellar structures of more than 2300 galaxies of all morphological types from the Local Universe within a distance of 40 Mpc from the

Milky Way, allowing for detailed structural studies as a function of stellar mass as well as of the local environment (e.g. Laine et al., 2014; Bouquin et al., 2018).

The environment is one of the key characteristics necessary for the elaboration and development of evolutionary theories, as the previous and other works have proved. Among them, the AMIGA project is dedicated to understand the profound relevance of the environment by studying highly isolated galaxies, as described further in Sect. 2.1.

Chapter 2

Scientific context, motivation and aims

The main motivation for this work lies in the results of the asymmetry ratio found in the isolated galaxies of the CIG catalog. While this parameter is statistically lower than in any other sample, there is a small fraction of galaxies that raise a particular interest because they show unusually high values of this ratio. In this chapter, I present the AMIGA project as the context of this dissertation, an in−depth description of the definition and results of the asymmetry ratio study, the questions attached to it, the construction of the subsample of galaxies to approach the implications, a brief presentation of the galaxy CIG 96 as the model case for the study and the aims of the present Doctoral Thesis.

2.1 The AMIGA project

The Analysis of the interstellar Medium of Isolated GAlaxies project (AMIGA[1], Verdes-Montenegro et al. 2005) seeks to provide a better understanding on the formation and evolution of galaxies focusing on those that lie on relatively uninhabited environments in comparison with denser ones, even field galaxies. This is done by performing a systematic multi-wavelength study of a selected and statistically significant sample of

[1]Website: http://amiga.iaa.es

extremely isolated galaxies based on a refined version of the Catalog of Isolated Galaxies (CIG[2], Karachentseva 1973), described later in this section. Since the foundation, this project has been addressing the formative and evolutionary questions raised by the different implications of the internal and environmental processes, filling a previously vacant niche in the field of the formation and evolution of galaxies in this extreme environment. The AMIGA project constitutes the framework for the current dissertation.

2.1.1 The CIG and the isolation criteria

All galaxies have a first neighbour within a certain distance. In some cases, such distance is so close (a few kpc or less) that the two may be considered as interacting or merging galaxies; in other cases, it can be large enough as to consider that the two galaxies are gravitationally bound, with or without further apparent connection. By further restricting these conditions, it is possible to reach a situation in which a single galaxy is found inside a large volume of space with no interaction with the first distant neighbour. This hypothetical galaxy might then be classified as isolated. However, is there a distance from which the isolation is defined? Is there an interaction range that prevents or grants isolation? These questions can only be replied by making clear that the isolation is not an absolute property but a comparative magnitude of the galaxies. It only finds its meaning when comparing the different levels of isolation of different targets, measured under certain systematic criteria in a certain physical context. In other words, assuming a systematical quantification of the isolation magnitude, a galaxy is isolated or not; moreover, the level of isolation of a particular galaxy can only be described as higher or lower when compared to the level of isolation of another galaxy or galaxies. If strict and robust criteria are selected, the isolated galaxies constitute an ideal framework to study the secular evolution of galaxies. In this scenario, the evolutionary contribution provided by the mergers or interactions with external large neighbours does not exist. Then, the internal secular processes should remain as the main drivers of evolution, along with any possible contribution made by the surrounding environment like the still not confirmed cold gas accretion or minor mergers with dwarf−sized galaxies and other very small satellites.

[2]This catalog is referred as 'K73' in SIMBAD and 'KIG' in NED databases.

The level of isolation is a relative magnitude, what implies that the criteria used to define and measure it are not unique. A plethora of different selection criteria, more or less restrictive, may be found throughout the literature over the last 40 years (e.g. Turner and Gott, 1975; Balkowski and Chamaraux, 1981; Vettolani et al., 1986; Zaritsky et al., 1993; Marquez and Moles, 1996; Aars et al., 2001; Colbert et al., 2001; Pisano et al., 2002; Márquez et al., 2002, 2003; Prada et al., 2003; Varela et al., 2004; Muldrew et al., 2012; Spector and Brosch, 2016, to name a few).

The AMIGA project and, by extension, this work as part of it, uses the CIG as the reference sample and a revision of their isolation criteria, that remain among the most strict of the literature so far. The CIG catalog was assembled by identifying all galaxies that would not contain a similar sized galaxy (i.e. diameters between 1/4 and 4 times the diameter of the candidate galaxy) within a distance of 20 times its diameter, i.e. in some occasions, this meant projected distances of several Mpc. Those objects that would not fulfil these requirements would be rejected. This characterisation was done by reviewing the First Palomar Observatory Sky Survey (POSS-I) photographic plates and employed a visual projected isolation criterion since the redshift distances were scarce at that time. A total of 1051 objects were added to the CIG, all found in the Catalogue of Galaxies and of Cluster of Galaxies Zwicky et al. (1961), representing approximately the $\sim$3%.

The AMIGA project improved the CIG by reviewing and quantifying the CIG the isolation criteria using digitised images of the POSS-I and POSS-II (Verley et al., 2007b). The revision introduced two parameters, complementary to each other, to quantify the isolation according to the number of neighbours and the tidal forces applied, provided by Verley et al. (2007c) (hereafter V07) and revised later by Argudo-Fernández et al. 2013 (hereafter A13, also used by Argudo-Fernández et al. 2014). These two studies used different subsamples of the CIG according to the available data for the corresponding galaxies in each case[3]. The two parameters are:

- the local number density, η_k, that accounts for the first k neighbours found within a radius of 0.5 or 1 Mpc (depending on the criteria selected, V07 or A13) with

[3]Throughout this dissertation, any mention to the isolation parameters will be accompanied by a reference to the revision used to compute them, either V07 or A13.

respect to the host galaxy,

$$\eta_k \propto log\left(\frac{k-1}{V(r_k)}\right) \tag{2.1}$$

where the volume $V(r_k)$ is the projected distance to the k-th neighbour (radius r_k in arcminutes):

$$V(r_k) = 4\pi r_k^3/3 \tag{2.2}$$

- the tidal force estimation, Q, that quantifies the tidal strength that the neighbours exert on the host,

$$Q_{iP} \equiv \frac{F_{tidal}}{F_{bind}} \propto \frac{M_i}{M_P}\left(\frac{D_P}{R_{iP}}\right)^3 \tag{2.3}$$

where M, D and R stand for the masses, diameters and distance of the neighbour (i) and the primary (P).

The physical interpretation of both is that the farther the considered neighbours lie, the lower η_k and Q, i.e. the more isolated the galaxy is from external influences. In comparison with other samples like the HCG, the catalogs of Karachentsev's Isolated Pairs and Karachentseva's Isolated Triplets (KPG, KTG, Karachentsev 1972; Karachentseva et al. 1979) or the galaxies in the Abell Clusters (ACO, Abell 1958; Abell et al. 1989), the mean values of the isolation parameters η_k and Q calculated for each one are all higher than the mean values of CIG. In other words, the CIG shows the lowest mean isolation values compared to the other samples like the KPG, KTG, HCG and ACO, whose mean isolation values are larger and increase coherently with their growing environments (see Figures 2.1 and 2.2).

2.1.2 Results of the AMIGA project

The AMIGA project has yielded a large number of results after studying the isolated galaxies from the CIG in different spectral ranges, summarised next. The morphological revision of the sample by Sulentic et al. (2006) showed that the late−types are much more frequent than the early−types, yet there are galaxies in every morphological branch: 6% are E−E/S0, 9% are S0−S0a, only 4% are Sa−Sab, while 65% are Sb−Sc and 16% are Scd−Im. When compared to any other sample, the CIG shows the lowest

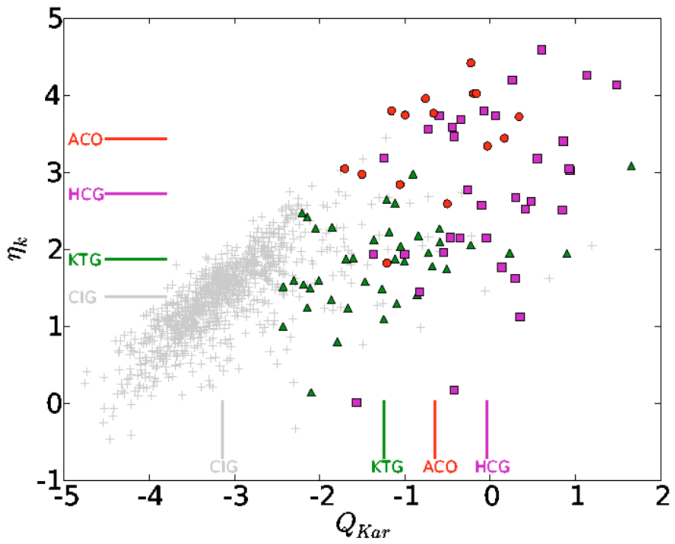

Fig. 2.1 Comparison between the isolation parameters η_k and Q for the CIG (grey pluses) and the comparison samples KTG (green triangles), ACO (red dots) and HCG (purple squares). The marks indicate the mean values of each sample in their corresponding colour. Credit: Figure 6 from Verley et al. (2007c).

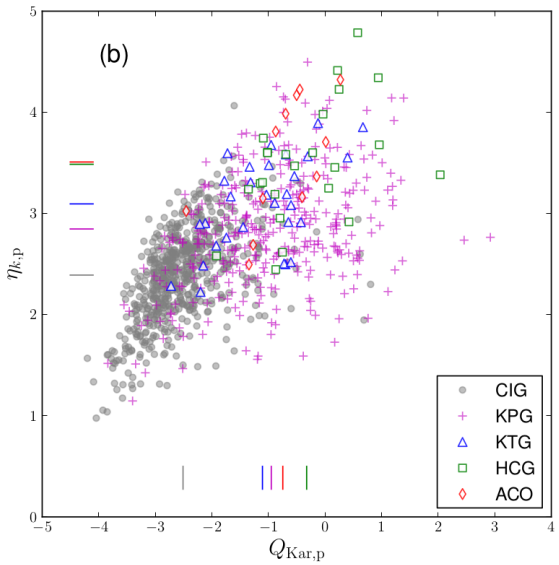

Fig. 2.2 Comparison between the isolation parameters η_k and Q for the CIG (grey pluses) and the comparison samples using photometric data, KPG (purple pluses), KTG (blue triangles), HCG (green squares) and ACO (red diamonds). The marks indicate the mean values of each sample in their corresponding colour. Credit: Figure 3, panel b from Argudo-Fernández et al. (2013).

values for the following physical parameters: the B and far−infrared luminosities (L_B and L_{FIR}, Verdes-Montenegro et al. 2005; Lisenfeld et al. 2007, respectively), the radiocontinuum levels from the mild SF of the disc (Leon et al., 2008), the ratio of radio−excess galaxies either considering early−, late− types or globally (Sabater et al., 2008), the asymmetry level of the integrated HI profiles (Espada et al., 2011b), the molecular gas (Lisenfeld et al., 2011) and the median absolute deviation in colour (Fernández Lorenzo et al., 2012). Besides, the isolated spiral galaxies of the CIG show larger discs (Fernández Lorenzo et al., 2012) and larger bars on average (Durbala et al., 2008) while not being preferentially barred or unbarred (Verley et al., 2007a) and most Sb−Sc spirals host pseudobulges (Durbala et al., 2008; Durbala, 2009). There is no evidence of a difference in the fraction of AGN between the CIG galaxies and HCG, yet such difference exists for the fraction of star forming nuclei between the CIG and HCG, suggesting also that the growth of their black holes could be produced without the need of major mergers (Sabater et al., 2012). The recent scaling relations between the HI mass and the optical properties derived by Jones et al. (2018) are suitable for use as statistical measures of the impact of interactions on the HI content of galaxies.

In the work by Fernández Lorenzo et al. (2014, includes Ramirez-Moreta), we presented a study of the structural parameters and colours of the pseudobulges of a large selection of AMIGA galaxies. The initial sample consisted of 279 galaxies that were refined down to 189 after performing satisfactory structural modelling with GALFIT (Peng et al., 2010) on SDSS i images of the candidates. They were predominantly populated by late−type spiral galaxies (∼66%, according to Sulentic et al., 2006; Durbala et al., 2008), 45% of them with bars. As shown in Fig. 2.3, we found that 94% of them host pseudobulges (Sérsic index values of $n_b < 2.5$) and, according to GALFIT results, we subdivided in high bulge−to−total (B/T > 0.1) or low bulge−to−total (B/T < 0.1) ratios. The remaining 6% were classical bulges ($n_b > 2.5$).

The $g - i$ colours of the pseudobulges and discs were computed and compared with the sample of Nair and Abraham (2010), as shown in the $g - i$ colour-magnitude diagram of Fig. 2.4. We found that 64% of the pseudobulges are as red as early−type galaxies, 66% being low B/T and 58% high B/T located in the red sequence. Also, the pseudobulges showed equal distributions regardless of their B/T, and median $g - i$ values of 1.06±0.11 (low B/T) and 1.04±0.13 (high B/T) yet low B/T pseudobulges

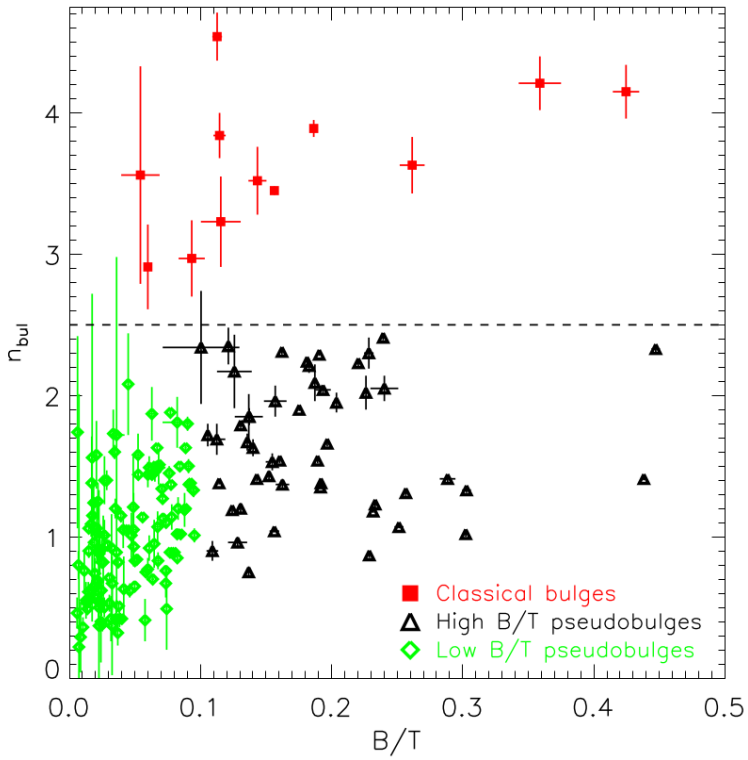

Fig. 2.3 Bulges Sérsic index vs. bulge$t$−to−total ratio (B/T). Classical bulges indicated in red squares above the $n_b = 2.5$ line, pseudobulges below. High and low B/T pseudobulges indicated with black triangles and green diamonds, respectively. Credit: Figure 1 from Fernández Lorenzo et al. (2014).

show larger differences than high B/T pseudobulges, reflecting redder discs in the latter. We concluded that the pseudobulges tend to have low B/T ratios and that their colour differences suggest early formation of the bulges and different SF histories for the disc and bulge. The majority ($\sim 64\%$) present similar colours to those in the early−type galaxies, suggesting old stellar populations, while the bluer ones tend to be in galaxies affected by tidal interaction.

The last and former results demonstrate the deep physical implications that an extremely isolated environment may have over a galaxy and its evolution. Hence, it is of essential need to consider a sample of galaxies selected with strict isolation criteria in order to improve our understanding of how galaxies evolve through time.

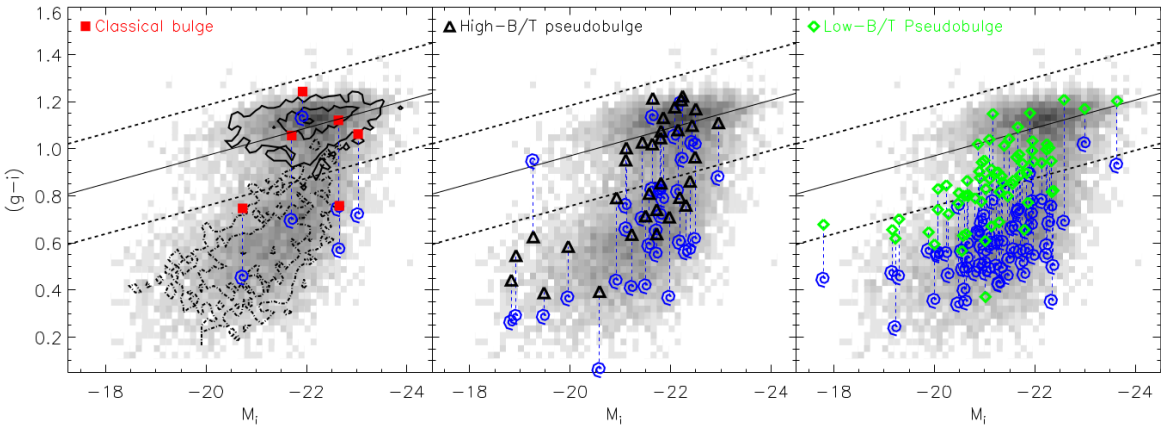

Fig. 2.4 $g-i$ colour corrected from internal reddening vs. SDSS i absolute magnitude, M_i. The bulge−disc pairs of values are joined by broken blue lines while classic, high B/T and low B/T pseudobulges colours are shown in red squares, dark triangles and green diamonds, respectively; discs are shown as blue spirals in all panels. The grey background represents the density diagram obtained from the Nair and Abraham (2010) sample at $0.01 < z < 0.05$. The straight solid and dashed lines are the linear fit and the 2σ for their early−type galaxies (E/S0). The left panel shows the contours of equal density for these galaxies as solid lines, and for Sbc-Sd spirals as dotted lines. Credit: Figure 3 from Fernández Lorenzo et al. (2014).

2.2 Asymmetries in galaxies. The case of the isolated galaxies

Previous studies have shown that about half of the galaxies present global dynamical states of non−equilibrium in the stellar and gaseous regimes (Richter and Sancisi, 1994; Rix and Zaritsky, 1995; Zaritsky and Rix, 1997), evidenced as asymmetries and lopsidedness. The difference between the two terms is subtle: the lopsidedness compares the level of symmetry of a galaxy image, line profile or velocity field with respect to the minor or major axis (Baldwin et al., 1980); the asymmetry is the level of symmetry of an object with respect to a 180° rotation around the center (Abraham et al., 1994).

Bournaud et al. (2005) find the asymmetric distribution of the stellar and gaseous contents of a galaxy insufficient to cause all the lopsidedness observed in the galaxies. For it to happen, other external agents are necessary further than the inner dynamical mechanisms or short−lived tidal encounters, like the interaction with

companions, minor mergers, gas accretion or removal, or underlying asymmetries of the dark matter halo (Richter and Sancisi, 1994; Zaritsky and Rix, 1997; Kereš et al., 2005; Reichard et al., 2008, e.g.) and conclude with the proposal that a cosmological accretion of gas on galactic disks must be in part responsible for such lopsidedness − usually referred to as cold gas accretion.

Considered as a key structural parameter to measure major current and past formative and evolutionary stages, the asymmetry of a galaxy can be measured with different methods depending on the data used (e.g. Abraham et al., 1996; Conselice, 2003, and others). For instance, Reichard et al. (2008, 2009) calculated the lopsidedness of ∼25000 galaxies using the radially averaged amplitude of the $m = 1$ azimuthal Fourier mode between the radii of 2D data (SDSS g and i images from Data Release 4) enclosing 50% and 90% of their light. They showed that the lopsidedness is strongly correlated to the stellar mass density, given that it increases with the disc radius in the spiral galaxies, particularly. Moreover, they conclude that the tidal perturbations mostly affect and last longer in low density galaxies as well as low density regions, i.e. the outskirts of average density galaxies. However, the stellar component is not necessarily correlated to the gas component since the extension of the latter is generally twice that of the former (Broeils and van Woerden, 1994; Kornreich et al., 2000).

The asymmetries in the HI disc are good tracers of colliding events (Holwerda et al., 2011a) due to the high sensitivity of the gas to mergers and interactions (see Sect. 1.1.3). Holwerda et al. (2011b) used a combination of parameters to measure the lopsidedness and the interaction level of HI discs of 141 galaxies, optimising the statistical determination of the merger rate in a sample of galaxies and lowering the bias introduced by the observer. Recently, Giese et al. (2016) used the same parameters to provide an improved asymmetry determination of non−parametric methods dependent of signal−to−noise (hereafter, SNR), resolution and inclination, reinforcing the asymmetry parameter as the most powerful determination of lopsidedness in higher SNR cases. The main mechanisms associated to the lopsidedness have confronted perspectives: the inner−outer agents and the short−long lived interactions. In an environment devoid of large companions, the tidal interactions of a galaxy should be drastically reduced and, as a consequence, the lopsidedness should also be lower.

Also, when comparing the asymmetrical footprints of the isolated cases with those from galaxies in more crowded environments, differences should arise.

The CIG catalog is larger and has more strict isolation criteria than any other previous sample of isolated galaxies, making it ideal for the study of physical properties in such extreme environment, i.e. with minimised effects from tidal interactions and ram pressure stripping, Espada et al. (2011b) used it to perform a statistical study of the galaxy lopsidedness. They computed the HI integrated spectra[4] of a refined subsample of 166 galaxies from the CIG out of the initial 312 AMIGA galaxies with high signal−to−noise−ratio (those with uncertain asymmetry measurements were removed) − a method that will also be applied to the data of distant unresolved galaxies obtained in the future with SKA. They discovered that the isolated galaxies show a statistically lower asymmetry ratio in their HI integrated profiles in comparison with other samples like those from Bournaud et al. (2005), Matthews et al. (1998), Haynes et al. (1998) and field galaxies (see Jones et al. 2018 for a full characterisation of the HI content of AMIGA sample). The definition of the parameter and the results are explained further in Sect. 2.2.1.

2.2.1 The asymmetry parameter $\mathcal{A}_{1/h}$

Throughout the literature, the quantification of the HI lopsidedness is carried out in different ways. Espada et al. (2011b) used the parameter $\mathcal{A}_{flux\ ratio}$ or $\mathcal{A}_{1/h}$ (e.g. Haynes et al., 1998; Kornreich et al., 2001; Espada et al., 2011b), an areal asymmetry parameter computed as the emission ratio between the two areas of the HI line defined with respect to the central velocity and its lowest and highest velocity[5]. It takes values of $\mathcal{A}_{1/h}$ if $\mathcal{A}_{1/h} > 1$ or as $1/\mathcal{A}_{1/h}$ if $\mathcal{A}_{1/h} < 1$. According to their notation:

[4]The spectral data are from archives, the literature and the Arecibo, Effelsberg, Nançay and Green Bank Telescope (GBT) single−dish observatories. Tabulated data are available at the AMIGA data section website.

[5]According to the definitions of asymmetry and lopsidedness (see Sect. 2.2) this concept corresponds to the lopsidedness of galaxies. However, we will refer to it as asymmetry to maintain the notation of Espada et al. (2005) and subsequent works.

$$\mathcal{A}_{flux\ ratio} = \mathcal{A}_{1/h} = \frac{S_l}{S_h} = \frac{\int_{V_l}^{V_m} S_\nu \, d\nu}{\int_{V_m}^{V_h} S_\nu \, d\nu} \tag{2.4}$$

where S_l and S_h is the emission below the spectrum areas in the regions with lower and higher velocity, V_l and V_h in $\mathrm{km\,s^{-1}}$, respectively, and V_m is the central velocity in $\mathrm{km\,s^{-1}}$.

The $\mathcal{A}_{1/h}$ parameter has three main sources of uncertainty that have to be added in quadrature. The first is due to the *rms* noise per channel or velocity width, σ, so the uncertainty for each side is calculated as: $\Delta S_i = \sqrt{N}\sigma R$, where N is the number of channels of the emission range (S_l or S_m) and R is the spectral resolution of the profile. The second corresponds to the uncertainty of the proper mean or central velocity (V_m). As discussed by Fouqué et al. (1990), the central velocity of a galaxy V_{cen} can be computed as the average between the lowest and highest velocities measured at a flux level of 20% the highest flux peak in the integrated spectrum (abbreviated $W20$, it may vary depending on the height percentage used to measure the width). The uncertainty of the central velocity is calculated as: $\Delta V = 4\,\frac{\sqrt{\delta\nu\,(W20-W50)/2}}{SNR_{peak}}$ where $\delta\nu$ is the spectral resolution of the cube, $(W20 - W50)/2$ represents the steepness of the edges of the HI profile at 20% and 50% of the maximum flux, and SNR_{peak} is the signal-to-noise ratio to the maximum flux peak. The third and last source of uncertainty is due to the observational pointing offsets of the antennas. These offsets may introduce a slight lopsidedness in the HI profile if the resolution and the galaxy are of similar size (Tifft and Huchtmeier, 1990; Springob et al., 2005) but the mean contribution ($\Delta A_{point} \sim 10^{-3}$) is negligible in comparison with the previous two, as calculated by Espada et al. (2011b).

They compared the normalised $\mathcal{A}_{1/h}$ and fitted half−Gaussian curves to the CIG and the samples by Haynes et al. (1998), Matthews et al. (1998), and Bournaud et al. (2005), which also contain isolated and field galaxies (see Fig. 2.5, Figure 12 from Espada et al. 2011b).

The CIG distribution (whose width of the half−Gaussian fit is $\sigma = 0.13$) presents the lowest $\mathcal{A}_{1/h}$ values after the comparison with the rest of the distributions, with only 2% of the sample having an asymmetry parameter in excess of 3σ, i.e. $\mathcal{A}_{1/h} > 1.39$, meaning a 39% excess of flux in one half of the spectrum.

However, the residual of the half−Gaussian fit showed 40−50 galaxies with unusually high levels of asymmetry that, in some cases, rose up to 50−60%, i.e. $\sim 1.5 - 1.6$ (see Fig. 2.6, Figure 5 from Espada et al. 2011b). Examples of three HI integrated profiles with different asymmetry levels are shown in Fig. 2.7, 2.8 and 2.9 (they correspond to the Figures 2, 3 and 4 from Espada et al. 2011b).

2.2.2 Limitations of $\mathcal{A}_{1/h}$ and the open question

It is important to remark that the $\mathcal{A}_{1/h}$ parameter only gives a numerical estimation of the asymmetry based on spectral 1D data, i.e. it does not provide information about the spatial distribution of the HI across the extension of the galaxy, but just about the HI emission per channel or velocity slice of the data cube.

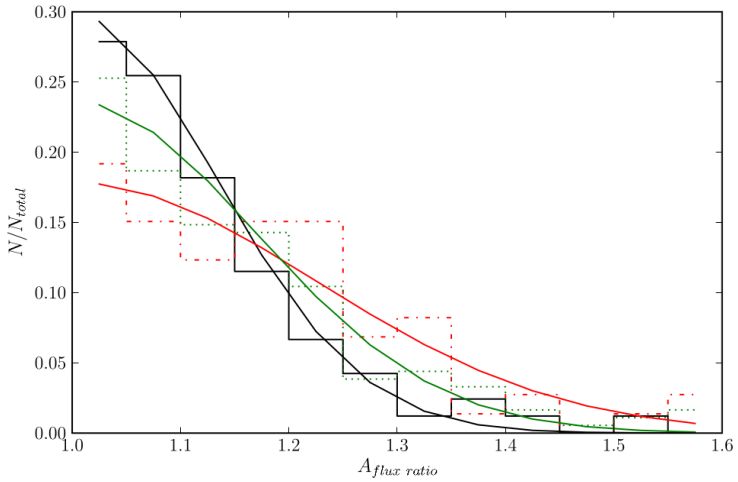

Fig. 2.5 Comparison of the normalised $\mathcal{A}_{1/h}$distribution between the refined sample of Espada et al. (2011b) (black solid histogram) and 1) Bournaud et al. (2005) (red dotted-dashed histogram); 2) a combined sample including HI data in Bournaud et al. (2005), Matthews et al. (1998), and Haynes et al. (1998) excluding CIG galaxies (green dotted line). The solid curves are the half−Gaussian curved fitted to each distribution. Credit of the image: Figure 12 from Espada et al. (2011b).

While a uniform distribution of the HI mass may be expected in an isolated galaxy according to the results, this parameter does not confirm whether or not a galaxy has a regular or anomalous HI spatial distribution. For instance, should the integrated emission of the two halves of an integrated profile were equal, then $\mathcal{A}_{1/h} = 1$, indicating a null asymmetry in the HI mass. However, the HI mass might have an uneven spatial distribution and still be split into two portions of equal mass quantity spread in an equal range of velocities above and below the central velocity. The same reasoning applies for a high $\mathcal{A}_{1/h}$ value: it does not explain where the excess of HI mass is located, neither why it is irregularly distributed.

For instance, T. C. Scott et al. (2014) show a clear example of the limitation of this parameter. They study the case of CIG 340, whose low asymmetry ratio is of $\mathcal{A}_{1/h} = 1.033 \pm 0.020$ (Espada et al., 2011b) suggested an HI disc with very symmetric morphology. However, their low and high resolution datacubes from GMRT interferometric observations showed the HI is warped in the Northern side and shows a deviated HI trail, as can be seen in Fig. 2.10, Figure 2 from T. C. Scott et al. (2014).

Then, why do some isolated galaxies like those from Fig. 2.8 and 2.9 present such high $\mathcal{A}_{1/h}$ values? What are the sources that are causing such asymmetry in the HI integrated profiles of these galaxies, as in the case of CIG 340 visible in Fig. 2.10?

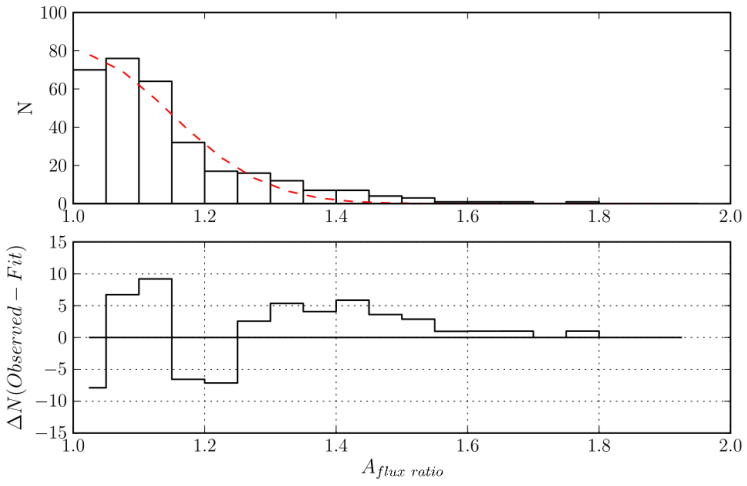

Fig. 2.6 *Upper panel*: the $\mathcal{A}_{1/h}$distribution (solid line histogram) of the HI sample ($N = 312$ galaxies) and its best half−Gaussian fit (dashed line). *Lower panel*: the residual of the half−Gaussian fit to the observed $\mathcal{A}_{1/h}$distribution. Credit of the image: Figure 5 from Espada et al. (2011b).

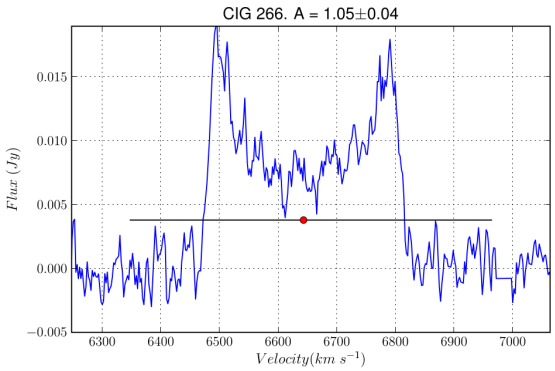

Fig. 2.7 Symmetric HI profile: CIG 266, $\mathcal{A}_{1/h} = 1.05 \pm 0.05$. The points where the horizontal (black) line intersects the profile correspond to the low (V_l) and high (V_h) velocity ends at a 20% level with respect to the peak. The derived mean velocity (V_m) at a 20% level is plotted as a (red) point. Credit of the image: Figure 2 from Espada et al. (2011b).

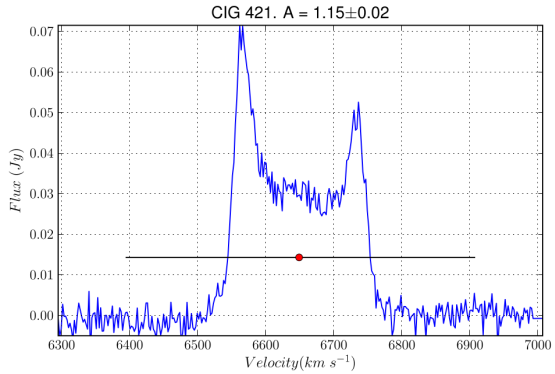

Fig. 2.8 Slightly asymmetric HI profile: CIG 421, $\mathcal{A}_{1/h} = 1.15 \pm 0.03$. See description in Fig. 2.5. Credit of the image: Figure 3 from Espada et al. (2011b).

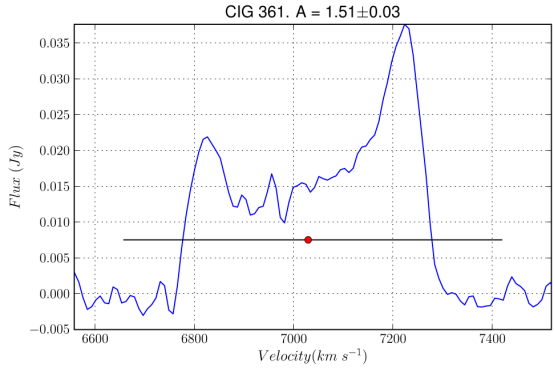

Fig. 2.9 Strongly asymmetric HI profile: CIG 361, $\mathcal{A}_{1/h} = 1.51 \pm 0.03$. See description in Fig. 2.5. Credit of the image: Figure 4 from Espada et al. (2011b).

Are there any detectable external agents interacting and disrupting the HI envelope of these galaxies? Do these asymmetries have an internal origin instead? May the causes of the asymmetries be taking active part in the evolution of the isolated galaxies? Finding the reasons behind the large values of $\mathcal{A}_{1/h}$ and answering these questions constitute a large portion of the motivation of the current dissertation.

2.3 Sample selection

The first steps to look for the physical causes behind the different levels of asymmetry found in the HI spectra started with the acquisition of VLA interferometric data. The first selection of these targets was made taking into account the CIG after being revised by Verley (2005) with a tidal parameter γ_{tide}, that accounts for a distance relation between the host and the closest galaxies. This parameter is defined as follows:

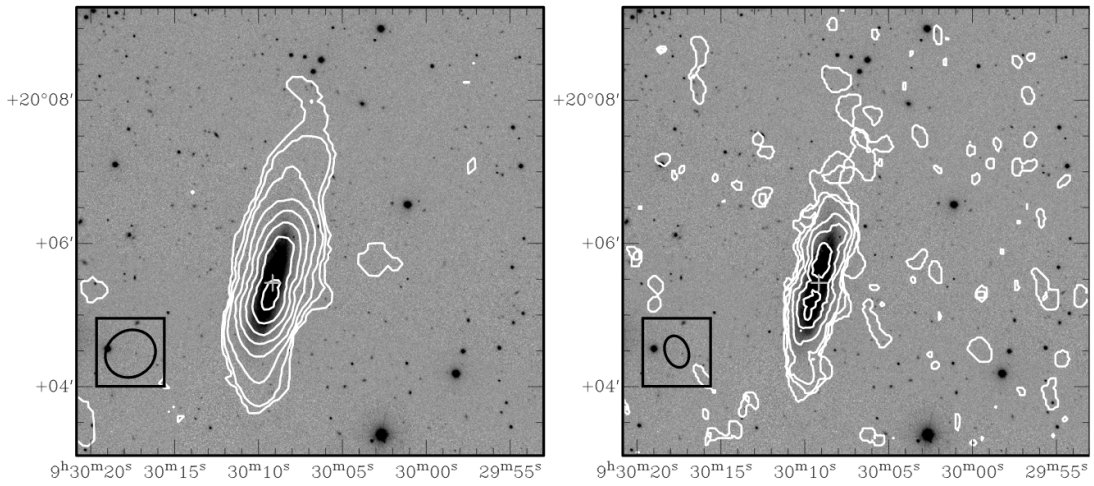

Fig. 2.10 Integrated HI emission contours (white) overplotted on a SDSS r band images of CIG 340. *Left*: integrated emission contours from the low resolution HI map, (beam size = 45.57" × 41.35") where the HI column density levels are 10^{20} cm^{-2} $\times(0.5, 1.2, 2.3, 4.7, 7.0, 9.3, 11.6, 14.0)$. *Right*: integrated emission contours from the high resolution HI map, (beam size = 26.08" × 19.97") where the HI column density levels are 10^{20} cm^{-2} $\times(1.6, 3.2, 6.3, 10.6, 19.0, 25.3)$. The first contours are at the 3σ level. Beam size shown as a framed black ellipse. The optical centre of the galaxy is marked with a grey cross. Credit of the image: Figure 2 from T. C. Scott et al. (2014).

$$\gamma_{tide} = \sum_i \frac{\left(\frac{r_i}{r_{CIG}}\right)^3}{{d_i}^3} \tag{2.5}$$

where r_i is the radius if the $i-$th galaxy in arcsec, r_{cig} is the radius of the target galaxy and $d_i^3 = d/D_{25}$ is the distance of the $i-$th galaxy normalised to the target diameter (D_{25}). Similar to the tidal force estimation Q of the subsequent isolation criteria, γ_{tide} takes into account the sizes an distances of the galaxies but leaves out their masses, unlike Q. The galaxies selected had signal$-$to$-$noise > 10 in their HI integrated profiles, a beam$-$to$-$galaxy ratio larger than 2 to avoid pointing problems or missing emission, values of $\mathcal{A}_{1/h} > 1.05$ and minimised external effects as given by low γ_{tide} values. This selection resulted in 9 galaxies from CIG. Another 3 galaxies that fulfilled the previous criteria were added from similar samples. Finally, another 5 targets with symmetric HI spectra $\mathcal{A}_{1/h} \sim 1$ were added as a control sample. Altogether, they added up to 12 well isolated and asymmetric galaxies and 5 symmetric ones.

As explained further in Sect. 2.6.2, the HI is highly sensitive to interactions yet faint optical and external structures may outlive the HI tidal features. For this reason, we built a sample out of the original CIG catalog (1051 galaxies) to perform deep optical observations. For simplicity, we will refer to it as 'the sample', unless stated otherwise. In order to build it, the following criteria were applied in order:

- the galaxies with an available HI spectrum are selected,
- from these, the spectra with a positive HI detection are selected,
- from these, the galaxies with $\eta_{k,A13} \leqslant 2.7$ are selected,
- if the A13 method does not have isolation values for a target, then the values from V07 are applied and the galaxies with $\eta_{k,V07} \leqslant 2.4$ are selected,
- from these, only the galaxies with central velocities $V > 1500$ km s^{-1} are selected to avoid close galaxies that may have too large angular sizes and, in consequence, force too long optical observations in order to cover their close environments,
- from these, the galaxies with Galactic extinction values $A_g < 0.5$ are selected,

- and last, from these, the galaxies with diameters measured on the 25 mag that are $D_{25} > 1$' are selected.

The source of the asymmetries is unknown yet and its nature may not be unique. Hence, it is necessary to include galaxies with different $\mathcal{A}_{1/h}$ values to identify the apparent causes and confirm those directly responsible of the asymmetry. For this reason, the $\mathcal{A}_{1/h}$ parameter is deliberately not considered in these selection criteria to avoid obtaining a biased sample. The number of members of this subsample ascends to a total of 184 galaxies. Among these, we find galaxies that can be considered fully symmetrical according to the $\mathcal{A}_{1/h}$ values, for instance, CIG 340 ($\mathcal{A}_{1/h} = 1.03$, as mentioned in Sect. 2.2.2) or CIG 568 ($\mathcal{A}_{1/h} = 1.08$) and galaxies with more asymmetrical HI distribution like CIG 96 ($\mathcal{A}_{1/h} = 1.16$) or CIG 1019 ($\mathcal{A}_{1/h} = 1.22$).

2.4 Optical observations of the sample

Along the last 6 years, some of the galaxies of the previously defined sample (see Sect. 2.3) were observed with different optical telescopes: Calar Alto observatory (CAHA[6], Almería, Spain), the VLT Survey Telescope (VST, ESO[7]) in Chile, the Nordic Optical Telescope (NOT, La Palma, Spain) and the Isaac Newton Telescope (INT, ING, La Palma, Spain). All the galaxies of the CIG are located in the Northern hemisphere. However, some targets have low declination values, allowing us to observe them with telescopes located in the Southern hemisphere, like VST.

In order to reach faint surface brightness levels of $\sim$27 mag arcsec^{-2} with the previous telescopes, we calculated that the minimum time on source would be approximately of 4−5 hours. A total of 32 galaxies were fully observed (time on source $\geqslant$ 4 hours) namely, CIG 11, CIG 33, CIG 96, CIG 59, CIG 152, CIG 154, CIG 279, CIG 568, CIG 1002, CIG 1027 and CIG 1047 with VST; CIG 85, CIG 94, CIG 96, CIG 250, CIG 281, CIG 335, CIG 340, CIG 467, CIG 604, CIG 613, CIG 616, CIG 736,

[6]Based on observations collected at the Centro Astronómico Hispano Alemán (CAHA) at Calar Alto, operated jointly by the Max-Planck Institut für Astronomie and the Instituto de Astrofísica de Andalucía (CSIC).

[7]Based on observations made with ESO Telescopes at the La Silla Paranal Observatory under programme ID 093.B-0894 and 098.B-0775.

CIG 756, CIG 772, CIG 800, CIG 812, CIG 838, CIG 841, CIG 862, CIG 911, CIG 947 and CIG 1039 with CAHA, INT and NOT telescopes. Some of these targets were observed with more than one telescope, e.g. CIG 96. Also, another 10 galaxies were partially observed (time on source $\geqslant$ 4 hours) namely, CIG 41, CIG 53, CIG 121, CIG 204, CIG 292, CIG 615, CIG 862, CIG 879, CIG 1004 and CIG 1019. Further information of some of these observations can be found in Ch. 7.

Out of these targets, a few had been observed previously in different scientific contexts to the deep observations aimed by the current work. However, some showed interesting results, like the case of CIG 340 (Fig. 2.10). The deep observations program started with the pilot observations of CIG 96 and CIG 1019 in September 11^{th} and 19^{th}, 2012. As described in the following sections, CIG 96 had already been observed in the 21 cm wavelength (both single−dish and interferometric data) and a new analysis with ultraviolet images had just been published (q.v. Espada et al., 2005, 2011b). This previous scientific background made CIG 96 an ideal first case for an extended study with deep HI and optical observations, with the aim of studying the connection between the gaseous and stellar components and the possible features and asymmetries of the galaxy by reaching much fainter levels than in previous works.

2.5 The interest of the spiral galaxy CIG 96

NGC 864 is a spiral galaxy included in the CIG catalog as CIG 96. Previous works carried out on this galaxy (see Sect. 2.6.1) have shed light upon many of its properties. However, they still can not fully explain the causes for the asymmetry signature of its HI integrated profile. The isolation of CIG 96 rules out any major mergers and the current data of the galaxy do not suggest any specific source for its 16% asymmetry level ($\mathcal{A}_{1/h\,CIG96} = 1.16$, Espada et al. 2011b) in the HI integrated profile. Are there any external agents involved in the HI asymmetry of CIG 96 or do its own inner evolutionary mechanisms prevail instead?

These new questions are directly related to those drafted by the results of the HI distribution asymmetries, i.e. the unresolved HI asymmetry problem finds a direct exponent in this galaxy. For this reason, they motivate a new in−depth study dedicated

to look for the footprints of the HI asymmetries with a well known galaxy such as CIG 96 as model case.

2.6 The isolated spiral galaxy CIG 96

The spiral galaxy CIG 96 is a member of the selected sample of isolated galaxies and it has been studied over the last years in several spectral bands by different authors. In this section, I present an overview of the characteristics of CIG 96 with a summary of the most relevant results up to date, pointing out the attributes that are thoroughly analysed and discussed in the following sections of the dissertation.

2.6.1 Main characteristics and previous works

Briefly introduced in Sect. 2.5 and 2.4, CIG 96 is a slightly flocculent and barred spiral galaxy classified as a SAB(rs)c type by de Vaucouleurs et al. (1991) and as a barred Sc type by Sulentic et al. (2006) and Fernández Lorenzo et al. (2012) and located at a distance of 20.3 Mpc[8]. At the isophotal level of 25 mag arcsec^{-2} in the B band, it has a diameter of 2'.35 in its major axis that corresponds to a size of 13.9 kpc, the minor−major axis relation is 0.6988 so the inclination of the galaxy is of 46°.3 and the position angle (hereafter PA) is of 20°. These and other parameters of CIG 96 are listed in Table 2.1.

With respect to the environment (see Sect. 1.2), the mean and standard deviation values for the two isolation parameters according to V07 and A13 are indicated in Table 2.2.

The isolation parameters of CIG 96 according to the method by V07 are $\eta_{k,V07}$ =0.877, and Q_{V07} =-1.980, within 1×$\sigma(\eta_k)$ and 1.7×$\sigma(Q)$ with respect to the mean values of $<\eta_k>$ and $<Q>$, respectively. According to the A13 method, $\eta_{k,A13}$ =0.68 and Q_{A13} =-3.41, 4×$\sigma(\eta_k)$ and 1.3×$\sigma(Q)$, respectively. CIG 96 is a

[8]Throughout this work, a cosmology with $H_0 = 75\,\mathrm{km\,s^{-1}\,Mpc^{-1}}$, $\Omega_{\Lambda 0} = 0.73$ and $\Omega_{m0} = 0.27$ is assumed.

standard member of the CIG population and a very isolated galaxy of the nearby Universe. The implication of the isolation parameters is discussed further in Sect. 5.1.

Table 2.1 Parameters of CIG 96 (NGC 864)

Parameter	Value
$\alpha_{(2000)}$ [a]	$02^h15^m27.6^s$
$\delta_{(2000)}$ [a]	+6°00'09"
Type [b]	SAB(rs)c / Sc
Distance [c]	20.3 Mpc
r_{25} [d]	2'.35 / 13.9 kpc
Inclination [e]	46°.3
Position angle [e]	20°.0
$A_{int}(r)$ [c]	0.185
$A_k(r)$ [c]	0.006
$A_{int}(g)$ [c]	0.255
$A_k(g)$ [c]	0.008

Notes.
[a] Leon and Verdes-Montenegro (2003).
[b] SAB(rs)c according to de Vaucouleurs et al. (1991) and Sc according to Sulentic et al. (2006).
[c] Fernández Lorenzo et al. (2012). Distance computed using $H_0 = 75\,\mathrm{km\,s^{-1}\,Mpc^{-1}}$. A_{int} and A_k represent the internal and k-correction extinction terms in SDSS r and g bands.
[d] Semi-major axis of the galaxy at the isophotal level $25\,\mathrm{mag\,arcsec^{-2}}$ in the B band (Fernández Lorenzo et al., 2012).
[e] This work.

According to Buta et al. (2005), CIG 96 has a fairly strong bar[9] that is statistically less frequent than other bars of weaker strength. The bar hosts a circumnuclear ring with SF (Martini et al., 2003; Comerón et al., 2010) and has three corotation radii located in the following positions: within the bar ($0.25\times r_{bar}$), just beyond the bar ($1.29\times r_{bar}$) and within the spiral arms ($>1.29\times r_{bar}$), respectively (Buta and X. Zhang, 2009).

Using the Hα emission, Erroz-Ferrer et al. (2012) studied the kinematics of the inner regions of CIG 96, bar included, with data from GHαFas instrument at

[9]Buta et al. (2005) refer to the bar strength parameter as Q_b; in the case of CIG 96 it is $Q_b = 0.321$, indicating a strong bar compared to other galaxies of their sample with weaker bars, i.e. $Q_b < 0.1$.

Table 2.2 Mean (<>) and standard deviation (σ) values of the isolation parameters for the CIG according to V07 and A13.

Parameter	V07 [a]	A13 [b]
$<\eta_k>$	1.378	2.39
$\sigma(\eta_k)$	0.556	0.45
$<Q>$	-3.142	-2.51
$\sigma(Q)$	0.689	0.68

Notes.
[a] Verley et al. (2007c).
[b] Argudo-Fernández et al. (2013).

William Herschel Telescope (ING, La Palma). In agreement with Buta et al. (2005), their bulge−disc−bar decomposition yields a flat−profile for the bar or, in other words, a strong bar (models discussed further by Athanassoula and Misiriotis 2002) that is linked to a higher exchange of angular momentum with the halo than weaker (exponential−profile) bars.

Exploring the radio continuum, Ulvestad and Ho (2002) used VLA archival data (B-configuration) from CIG 96 to confirm the presence of a central radio source at 6 cm (C band, 4−8 GHz) radio source whose emission of $\sim 10^{20}$ W Hz^{-1} at a resolution of $\leqslant$1" is consistent with being powered by nuclear starbursts rather than by a massive black hole, as in active galaxies. This result is consistent with Sabater et al. (2012), that consider CIG 96 is not an AGN galaxy after studying the mid− and far−infrared emission (MIR and FIR, respectively) from IRAS survey at 25 and 60 μm (see also Lisenfeld et al. 2007).

The works by Espada et al. (2005, 2011a,b) (hereafter abbreviated for simplicity as E05, E11a and E11b, respectively) provided a new and more complete insight on CIG 96.

E05 showed that CIG 96 has a large HI disc extended beyond $2\times r_{25}$ (approximately up to 12' or 71 kpc[10] in the major axis) with single−dish data from Green

[10]Throughout this work, all references to distance between different points of CIG 96 and the surroundings must be considered as projected distance unless stated otherwise.

Bank Telescope and interferometric data from VLA observatory in D-configuration. They discussed the asymmetry observed in the HI distribution of the disc (later, E11b would calculate the 16% asymmetry level) and presented a kinematical model of the galaxy. They unveiled the HI emission of a close and small neighbour (NGC 864 COM1) situated at at 15'.2 (∼90 kpc) to the East of CIG 96. To account for the HI asymmetry, they rule out any encounter with a massive companion as well as any close or oblique passage of another smaller galaxy. They leave the door open for a parallel passage through the equatorial plane of CIG 96 at an intermediate distance, i.e., outside the optical disc but within the extended HI disc.

At the ultraviolet (UV) wavelengths, E11a also detected a partially complete, extended UV (XUV) ring located at $1.5-2\times r_{25}$ with near-UV (NUV) and far-UV (FUV) data from GALEX, that also show some regions with SF. Hereafter I will refer to this ringed feature as the pseudoring of CIG 96. E11a also studied the Kennicutt−Schmidt SF law and efficiency in the large HI disc, using the VLA observations as well as the NUV and FUV data. By comparing the VLA maps and UV images, they found a good spatial correlation between the HI and both NUV/FUV emission, especially outside the inner 1'. Also, the main regions with SF lie on the enhanced HI emission of two spiral arm−like features connected to the HI pseudoring. They found that the (atomic) Kennicutt−Schmidt power−law index systematically decreases with the radius. Regarding to the star formation efficiency (hereafter SFE), they saw that it decreases with radius where the HI component dominates and that there is a break of the correlation at $r = 1.5\times r_{25}$. However, mostly within the HI pseudoring structure, i.e., between $1.5\times r_{25}$ and $3.5\times r_{25}$, SFE remains nearly constant. They concluded that this might be a common characteristic in XUV disc galaxies as well as that a non-axisymmetric disc can drive the outer spiral arms, as the morphology of the galaxy allows.

2.6.2 Causes of the features in CIG 96

In addition to the question raised by the results of Espada et al. (2011b) with regard to the existing but so far unexplained lopsidedness of the isolated galaxies, the analysis of the optical and HI images by E05 and E11a showed two remarkable features of the

galaxy and its environment: a small companion and the external pseudoring with SF regions.

To date, no work has brought forward convincing arguments to explain whether the HI and optical features of CIG 96 are caused by the close companion or by any other external agent. As a consequence, it raises the question as to whether asymmetries might develop in galaxies free from interactions or not, complementing the motivation for a new and in-depth study of CIG 96.

However, to support any internal agent as the main evolutionary process, it is necessary to first rule out any external influence. Neither tidal features nor gas−rich companions are found in HI maps even for the most asymmetric cases (e.g. Portas et al., 2011; Sengupta et al., 2012) and current shallow optical images are relatively symmetric when dust patches are ignored. In absence of interactions for the last ∼2.7 Gyr (discussed in Sect. 5.1), any lopsided mode would have dropped already (Jog and Combes, 2009). Does this imply that secular evolution processes can lead to asymmetries?

Since the early works of Bosma (1978) and Bosma and Freeman (1993) it is known that our understanding of a galaxy may change after performing and comparing deep observations that let us reach very low surface brightness levels of a galaxy and its surroundings. Hence, performing this kind of observations was a natural follow−up for the case of CIG 96. Additionally, as suggested by the N−body simulations of Peñarrubia et al. (2005), the orbital properties of halo substructures are determined by the environment and can survive several Gyr, outliving HI tidal features. Within the last two decades, a number of works have unveiled many faint structures or companions that remained hidden in shallower observations (e.g. Martínez-Delgado et al., 2008, 2009, 2015; Duc et al., 2015; P. G. van Dokkum et al., 2015; Trujillo and Fliri, 2016; Trujillo et al., 2017; Iodice et al., 2017; Bosma, 2017, among others).

In the following Chapter 3, I present the new and deep HI and optical data of CIG 96. They have been used to study in detail its faint gaseous and stellar components as well as the surroundings with the aim of revealing any possible causes of the HI asymmetrical distribution of the galaxy and other effects on its evolution.

2.7 Scientific aims

The main scientific aims pursued with the work presented in this Doctoral Thesis are:

- Try to understand the formation of asymmetries in isolated galaxies with deep optical and HI observations.
- Evaluate the possible causes of the different asymmetries found in CIG 96, whether internal or external.
- Look for observational signatures of interactions between CIG 96 and its environment.
- Characterise and probe the origin of any new external features of CIG 96.
- Evaluate the interference of the possible and detectable external agents over the evolution of CIG 96.
- Characterise the origin, structure, colours and age of the pseudoring of CIG 96.
- Establish the optical and HI study of CIG 96 as the reference for other isolated galaxies with high asymmetry ratio in their HI integrated profiles.

Chapter 3

Methods

In this chapter I present a description of all the data of CIG 96 used in this dissertation, i.e. the characteristics and observing strategies of the HI and optical observations performed for this study, the reduction and calibration methods used to produce their final images, as well as the complementary infrared images of Planck, retrieved from the archive, and WISE band 3, kindly provided by Dr. Tom Jarrett. The most relevant data are summarised in Tables 3.1 and 3.2.

3.1 HI observations of CIG 96

21 cm line observations of CIG 96 were made using the NRAO Karl G. Jansky Very Large Array observatory in two different epochs: one, as the Very Large Array (hereafter VLA) and two, as the Extended Very Large Array (hereafter EVLA), that is an upgrade of the original VLA with new receivers and a more powerful and versatile correlator.

3.1.1 Description of the VLA and EVLA observations

Two VLA projects submitted by the AMIGA group, AV0276 and AV0282 (submitted by AMIGA in both cases), were performed in July 2004 and July 2005, obtaining 3 hours in D-configuration (26 antennas used) and 7 hours in C-configuration (27 antennas

used), respectively. Both observing projects were prepared and executed with the same set up: 2 IF correlator mode, a bandwidth of 3.125 MHz per IF and a frequency resolution of 48.8 kHz that corresponds to a velocity resolution of 10.4 km s^{-1}.

The EVLA project 13A-341, fully dedicated to observing CIG 96, was executed during 2013 as follows: 3 hours in March, in D-configuration; 3 hours in May, in the hybrid DnC-configuration and 10 hours in July, in C-configuration. In all cases, 27 antennas were used. The set-up of these observations consisted of single IF correlator mode, a bandwidth of 2 MHz and a frequency resolution of 16 kHz, equivalent to a velocity resolution of 3.3 km s^{-1} that was smoothed to 10 km s^{-1} for the calculations. These data are summarised in Table 3.1.

3.1.2 Calibration methods and HI datacubes

All the VLA and EVLA data were fully calibrated and imaged using CASA software package (McMullin et al., 2007) tasks[1]. Each data set or Measurement Set (abbreviated MS) was scanned to remove bad data and RFI (radio-frequency interferences). They were separately calibrated in phase, amplitude and bandpass and imaged individually to check their suitability for our aims. We used the CLEAN algorithm (Högbom, 1974) to produce a set of two individual datacubes by separately combining all VLA data and all EVLA data, respectively. We also produced a combined datacube out of the previous two, as explained later. The hybrid DnC-configuration data were discarded due to the presence of a remarkable amount of RFI, making them too defective for our goals. The VLA data consisted of two individual MS, one for D-configuration data and one for C-configuration data. EVLA data consisted of thirteen individual MS: three MS were obtained in D-configuration and ten MS in C-configuration.

3.1.2.1 VLA datacube characteristics

All VLA data were used to produce a preliminary datacube via imaging using natural weighting. It led to a synthesised beam of 27.11" × 23.60" and a *rms* noise level of 0.31 mJy beam^{-1} (1σ), reaching a HI column density limit of $N_{HI} = 2.68 \times 10^{19}$ cm^{-2} (5σ).

[1] A sample script containing all the calibration and imaging steps is provided in Appendix A.

Assuming an HI linewidth of $10\,\mathrm{km\,s^{-1}}$, the achieved HI mass detection limit is $\sim 1.5\times10^{6}\,M_{\odot}\,(5\sigma)$ and an HI column density of $2.7\times10^{19}\,\mathrm{cm^{-2}}\,(5\sigma)$.

All HI masses in this work have been computed as given by Roberts (1962, 1975):

$$M_{HI}\ (M_{\odot}) = 2.356 \times 10^{5}\ D^{2}\ S\ \Delta V$$

where D is distance (Mpc) and $S\Delta V$ is the velocity integrated HI flux ($\mathrm{Jy\,km\,s^{-1}}$). This equation derives from the quantum mechanics of the hyperfine transition, assuming that the HI gas is optically thin.

The column density $N_{HI}\,(\mathrm{cm^{-2}})$ depends on the brightness temperature $T_B(K)$ integrated over the line width dv ($\mathrm{km\,s^{-1}}$). In turn, T_B depends on the flux density S ($\mathrm{Jy\,beam^{-1}}$) and the product of the major and minor axes $Maj \times min$ ($\mathrm{arcsec^{-2}}$). Respectively, the brightness temperature and column densities have been computed for this work as follows:

$$T_B\ (K) = 6.07 \times 10^{5}\ S\,(Maj\ \times\ min)^{-1}$$

$$N_{HI}\ (cm^{-2}) = 1.823 \times 10^{18} \int T_B\ dv$$

3.1.2.2 EVLA datacube characteristics

All EVLA data in C and D configurations were combined and imaged with natural weighting in a preliminary datacube. It had a median rms of $0.84\,\mathrm{mJy\,beam^{-1}}$ (1σ) and a synthesised beam of $37.57" \times 19.97"$. Such beam elongation is due to the short Right Ascension range in which the observations were taken. With a velocity resolution of $10\,\mathrm{km\,s^{-1}}$, the HI mass detection limit achieved was of $M_{HI} = 4.1\times10^{6}\ \mathrm{M_{\odot}}\,(5\sigma)$.

3.1.2.3 Combined EVLA and VLA datacubes

The resulting datacube of combining the EVLA and VLA datacubes shapes the reference datacube for the subsequent analysis of the HI observations. For simplicity purposes, hereafter we will refer to this combined data product simply as the 'HI cube'. After the rms-weighted concatenation of the VLA MS and EVLA MS we produced the final

datacube of this work (hereafter referred as the HI cube). The weighting was computed as $w(i) = rms(i)^{-2}$, where $rms(i)$ stands for the flux density rms of each cube in the same units. The corresponding weighting factors applied to the VLA and EVLA data were 10.40 and 1.42, respectively.

The HI cube comprises of a total of 19 hours on target and has a synthesised beam of 28.16" × 22.72" (2.77 kpc × 2.24 kpc at a distance of 20.3 Mpc). It covers a velocity range from 1330 km s^{-1} to 1800 km s^{-1} in 48 channels assuming spectral resolution of 10 km s^{-1}. We used the Kinematical Local Standard of Rest (LSRK) as the frame of reference for the radio velocities. Also, we worked with a smoothed beam of 28" × 28" to simplify the physical interpretation of the results and avoid beam effects. The corresponding HI cube yielded a median rms of 0.25 mJy beam^{-1} (1σ) that allowed us to reach an HI mass limit of $M_{HI}^{lim} \simeq 1.4{\times}10^{6}\, M_{\odot}$ (5σ) and an HI column density limit of $N_{HI} \simeq 1.78{\times}10^{19}$ cm^{-2} (5σ). After performing a wavelet filtering (see Sect. 3.1.3) over the HI cube, we have improved these results by a factor of ∼2, reaching a final median rms of 0.126 mJy beam^{-1} (1σ) per channel. The minimum HI mass detected is $M_{HI}^{lim} = 0.7{\times}10^{6}\, M_{\odot}$ (5σ), the HI column density limit is $N_{HI} = 8.9{\times}10^{18}$ cm^{-2} (5σ) and the total HI mass is $M_{HI}^{total} = 5.5{\times}10^{12} M_{\odot}$ (5σ). The integrated intensity map, the velocity field and the channel maps are all presented in Sect. 4.1.

3.1.3 Wavelet filtering of the HI cube

A robust detection of faint HI features relies on reaching a column density (N_{HI}) as low as possible with the best SNR. In order to improve further our N_{HI} limit, we have applied a wavelet filtering to our HI cube which allows to achieve a higher SNR. An in-depth discussion of the wavelet transform is beyond the scope of this paper but we provide here an explanation of the method used in this work. As explained by Leon et al. (2016), the wavelet transform is a powerful signal-processing technique that provides a decomposition of the signal into elementary local contributions defined by a scale parameter (Grossmann and Morlet, 1985). The wavelets are the scalar products of shifted and dilated functions of constant shape. The data are unfolded in a space-scale representation that is invariant with respect to dilation of the signal. Such an analysis is particularly suited to studying signals that exhibit space-scale discontinuities and/or

Table 3.1 Data and results of the HI observations with VLA/EVLA

Telescope	ΔV [d]	Time [e]	Beam size [f]	rms [g]	N_{HI} [h]	M_{HI} [i]
VLA [a]	1249.5−1895.2	10	27.1×23.6	0.31	2.68	1.5
EVLA [b]	1330−1700	13	37.6×20.0	0.84	6.19	4.1
VLA+EVLA	1330−1700	19	28.0×28.0	0.25	1.78	1.4
VLA+EVLA+WF [c]	1330−1700	19	28.0×28.0	0.13	0.89	0.7

Notes.
[a] 3 h in D configuration, 7 h in C configuration. The original channel width is 10.4 km s^{-1} (48.8 kHz).
[b] 3 h in D configuration, 10 h in C configuration. The original channel width of 3.3 km s^{-1} was smoothed o 10 km s^{-1} (48 kHz) for the current calibration.
[c] Wavelet filtering (WF) applied to the VLA+EVLA combined data.
[d] Velocity range in km s^{-1}.
[e] Integration time in h.
[f] Beam size in arcsec × arcsec.
[g] rms in mJy beam^{-1} (1σ).
[h] HI column density limit in 10^{19} cm^{-2} (5σ).
[i] HI mass limit in $10^6\,M_\odot$ (5σ).

hierarchical features, as may be the case for the possible structures located in the outskirts of the HI envelope of CIG 96.

Following the same procedure as Leon et al. (2016), we have used a B_3-spline scaling function. Similar to the Ricker function (mexican hat), the expression of this function has a positive kernel surrounded by a negative annulus and the total integrated area is zero. It is defined by the following convolution matrix $\mathcal{M}$:

$$\mathcal{M} = \begin{bmatrix} 1/256 & 1/64 & 3/128 & 1/64 & 1/256 \\ 1/64 & 1/16 & 3/32 & 1/16 & 1/64 \\ 3/128 & 3/32 & 9/64 & 3/32 & 3/128 \\ 1/64 & 1/16 & 3/32 & 1/16 & 1/64 \\ 1/256 & 1/64 & 3/128 & 1/64 & 1/256 \end{bmatrix}$$

We have applied this wavelet over the HI calibrated data via the *A trous* algorithm (see Bijaoui 1991) as described by Leon et al. (2000). This algorithm creates different filtered wavelet planes according to the scale parameters and a certain threshold level. The scale parameters have received values of 2^i with $i \in [1,6]$, each defining the $i-$th plane. Each $i-$th raw wavelet plane is defined as the subtraction of two components that, in turn, depend on the $i-$th scale parameter: 0^{th} component corresponds to the image plane itself; the rest of the $i-$th components are defined as the result of convolving the $(i-1)-$th component with the previously defined kernel function. The last plane, namely, the last smoothed plane or LSP (in our case, scale parameter of 2^6) does not undergo any convolution. Hence, it is not a wavelet plane itself but the residuals of the last convolution. With the consequent exception of the LSP, each raw plane is filtered above a threshold to construct the $i-$th filtered wavelet plane. For this work, such threshold was set at $5\sigma_i$, where σ_i is the rms noise for the $i-$th plane.

The combination of the filtered wavelet planes and the LSP is possible and may cause the rms to change. Since the original image is spread in different spatial scales, a limited combination of the planes implies the recovered flux will be a lower limit to the total emission contribution. Should all planes be combined, the recovery is complete and the total flux, conserved.

After filtering our HI cube, we combined all planes. The resulting rms and, accordingly, the HI column density limit, were improved by a factor of 2, as specified in the last paragraph of Sect. 3.1 and summarised in Table 3.1.

3.1.4 Blanking of the HI cube

Separating genuine emission from noise is key to discern faint structures of an image. In order to do so, we blanked non-signal pixels using the following method.

First, we applied a spatial smoothing over the wavelet−filtered HI cube by convolving it with a Gaussian kernel four times the size of the adopted synthesised beam, i.e., (2×28")×(2×28") or 56"×56". The resulting smoothed datacube was only used to create the masks for each channel, as described next. The noise of this particular datacube was $rms = 0.34\,\mathrm{mJy\,beam^{-1}}$ (1σ). Second, we created masks for each channel

of this smoothed datacube. The shapes of these masks were defined by masking out the pixels with values below a $3.5\times rms$ threshold ($\sim$1.2 mJy beam^{-1}). Finally, the masks from the smoothed datacube were applied to the original datacube (non spatially smoothed) to create the moment maps[2].

This method mainly has two advantageous consequences: one, the depth and spatial resolution of the original datacube remains unaffected by the masking and two, the threshold limit does not take into account for the integration the areas in each channel whose only contribution is noise. In other words, the blanking of the HI cube improves the resulting cube by removing any remaining effect from the sidelobes (either positive or negative) that might mimic nonexistent structures at low emission levels.

3.2 Optical observations of CIG 96

In order to obtain deep optical images of the outskirts and close environment of CIG 96, we performed observations in two different observatories. Deep observations need an observing strategy with strict constraints in terms of numerous exposures of large exposure times and a very good flat fielding.

3.2.1 Description of the optical observations

Two datasets were respectively observed with the 2.2m and 1.23m telescopes at CAHA observatory. The first dataset is from CAHA2.2m, a deep image with good seeing in the Cousins R band (see Sect. 3.2.1.1). The second dataset consists of three images taken with photographic B, G, R bands used to study colour index properties (see Sect. 3.2.1.2 and all 2.2m and 1.23m images combined in Fig. 3.1). The third dataset was obtained with the VST telescope and provides a very deep and wide field image to study the surroundings of the galaxy (see image in Fig. 3.5 and Sect. 3.2.1.1). The most relevant data are summarised in Table 3.2.

[2]All tasks used to generate the described moment maps are part of the CASA Image Analysis toolkit.

Table 3.2 Data of the optical observations

Tel (Inst.) [a]	Filter	B [b]	Sp. scale [c]	T [d]	FoV [e]	SB_{limit} [f]	Seeing [g]
CAHA2.2m (CAFOS)	Cousins R	2×2	1.04	3h 56m (71×200)	12×12 (71×71)	27.5	1.59
CAHA1.23m (DLR-MKIII)	B, G, R phot.[h]	1×1	1.04	3h 38m (109×120) [i]	15×16 (88×94)	–	1.56
VST (OmegaCAM)	SDSS r	2×2	0.21	5h 10m (122×154)	60×60 (350×350)	28.7	1.10

Notes.
[a] Telescope, instrument in brackets.
[b] Binning mode.
[c] Spatial scale in arcsec pix^{-1} according to the binning used.
[d] Total exposure time. Number of exposures × exposure time of each one in seconds in brackets.
[e] Field of view in square arcmin. Projected physical distance of the field of view according to the distance to the galaxy in brackets (see Table 2.1).
[f] Surface brightness limit in mag arcsec^{-2}.
[g] Seeing in arcsec.
[h] CAHA1.23m images in photographic filters.
[i] Total number of exposures. Out of them, 30, 37 and 42 were taken with B, G and R filters, respectively. Each one has an exposure time of 120 s.

3.2.1.1 CAHA2.2m dataset, data reduction and calibration

CIG 96 was first observed in the second half of the night of September 11^{th}, 2012 with the CAFOS instrument at CAHA2.2m telescope. The CAFOS SITe1d detector has 2048×2048 pixels with a pixel size of 24 μm (spatial scale of 0.53 " pix^{-1}), providing an effective circular field of view of ∼12' in diameter.

A total of 71 exposures of 200 s each build up a total time on source of 3h 56min. All images were taken in the Cousins R filter, dithered by ∼20" and in 2×2 binning mode, providing a pixel scale of 1.04 " pix^{-1}. Since the aim was to achieve a low surface brightness, no seeing restrictions were requested. The night conditions were photometric during most part of the night, with a median seeing of 1.59" (seeing ranging from 1.31" to 1.81"). We used standard reduction and calibration techniques from *repipy* and *LEMON* packages [3] and IRAF. No standard stars were measured in this campaign so the extinction coefficient was computed by means of non-saturated

[3] *repipy* (GitHub source) reduction package by J. Blasco-Herrera, *LEMON* (GitHub source) calibration package by Terrón and M. Fernández (2011).

stars present within the field of view of our observations. As a consequence, a larger uncertainty is introduced in the photometric calibration. In order to obtain the Zero Point of the night, we computed the Bouguer fit of 8 non-saturated stars (visible in all images) and calibrated them with the correspondent data from SDSS (Ahn et al., 2012). Since this dataset was taken using Cousins R filter, all fluxes were converted from SDSS magnitudes system to Cousins R using the transformation by Lupton (2005), derived by matching photometry data from SDSS Data Release 4 (DR4 Adelman-McCarthy et al. 2006) to Peter Stetson's published photometry for stars:

$$R_{ri} = r - 0.2936 * (r - i) - 0.1439 \tag{3.1}$$

in magnitudes, where r and i are the magnitudes in the SDSS r and SDSS i filters, respectively. The median Zero Point of the night is 24.28 ± 0.12 mag (Cousins R) and we reach surface brightness levels in each band of $\mu_{R\ Cous} = 27.5\,\mathrm{mag\,arcsec^{-2}}$ and $\mu_{r\ SDSS} = 28.0\,\mathrm{mag\,arcsec^{-2}}$, respectively.

3.2.1.2 CAHA1.23m dataset, data reduction and calibration

CIG 96 was observed for a second time on the night of December 8th, 2012 with the DLR-MKIII instrument at the CAHA1.23m telescope. The camera is equipped with an e2v CCD231-84-NIMO-BI-DD sensor (4k×4k pixels, $15\,\mu m\,\mathrm{pix}^{-1}$). The original field of view is 21.5'×21.5' but the observations were cropped down to the central 15'×16'.

In this case, we used three different filters: photographic B, G and R (different from Johnson-Cousins) for which a total of 30, 37 and 42 exposures of 120 s each were taken, respectively, in 1×1 binning mode. The night conditions were stable for the most part of the night and all filters present a median seeing of 1.56" (seeing range from 1.48" to 1.61"). The total integration time was 3h 38min.

As with the previous dataset, standard reduction was applied to all the images in each filter separately. However, they were divided by a blank field. It was obtained from an adjacent galaxy-free field and corrected for bias and regular flat field too, so the remaining image would not show any residual gradient. Dividing the images by this blank field allows large scale structures to be removed. We used the SDSS tabulated

fluxes from several stars to calibrate the images via the following relation between SDSS and photographic filters: B(3900-5100 angstrom) would correspond to SDSS g and R(5800-7000 angstrom) to SDSS r. However, G(4900-5800 angstrom) would lie right between SDSS g and r bands. For the conversion of G band to SDSS, we considered different scenarios in which the emission was split between SDSS g and r bands but it has not been used further in this work. Hereafter we focus on the empirical relations that we calculated for the photographic R and B bands with respect to SDSS r and g, respectively. The initial relations between the corresponding magnitudes before correcting from extinction are:

$$m_{r\ SDSS}^{+ext} = 1.01 * m_{R_{phot}} - 9.83 \pm 0.15 \tag{3.2}$$

and

$$m_{g\ SDSS}^{+ext} = 0.99 * m_{B_{phot}} - 9.70 \pm 0.33 \tag{3.3}$$

Internal extinction and $k-$correction were applied to the fluxes in both SDSS g and r bands. We used the extinction laws by Savage and Mathis (1979) (in agreement with Fitzpatrick 1999) where $A(B) = 4.10 \times E_{B-V}$; the internal extinction and k-correction in the B band for CIG 96 are $A_{int}(B) = 0.276$ and $A_k(B) = 0.009$, respectively (Fernández Lorenzo et al., 2012); the extinction-reddening relations for the SDSS bands are $A_x(g) = 3.793 \times E_{B-V}$ and $A_x(r) = 2.751 \times E_{B-V}$ (Stoughton et al., 2002).

These relations yield the following internal and k-correction values for each band: $A_{int}\,(g) = 0.255$, $A_{int}(r) = 0.185$, $A_k(g) = 0.008$ and $A_k(r) = 0.006$.

Hence, the final empirical extinction$-$corrected equations that convert R, B photographic bands to SDSS r and SDSS g bands, respectively, are:

$$m_{r_{SDSS}} = 1.01 * m_{R_{phot}} - 10.02 \pm 0.15 \tag{3.4}$$

and:

$$m_{g_{SDSS}} = 0.99 * m_{B_{phot}} - 9.96 \pm 0.33 \tag{3.5}$$

Finally, the images were average stacked applying an outliers rejection algorithm.

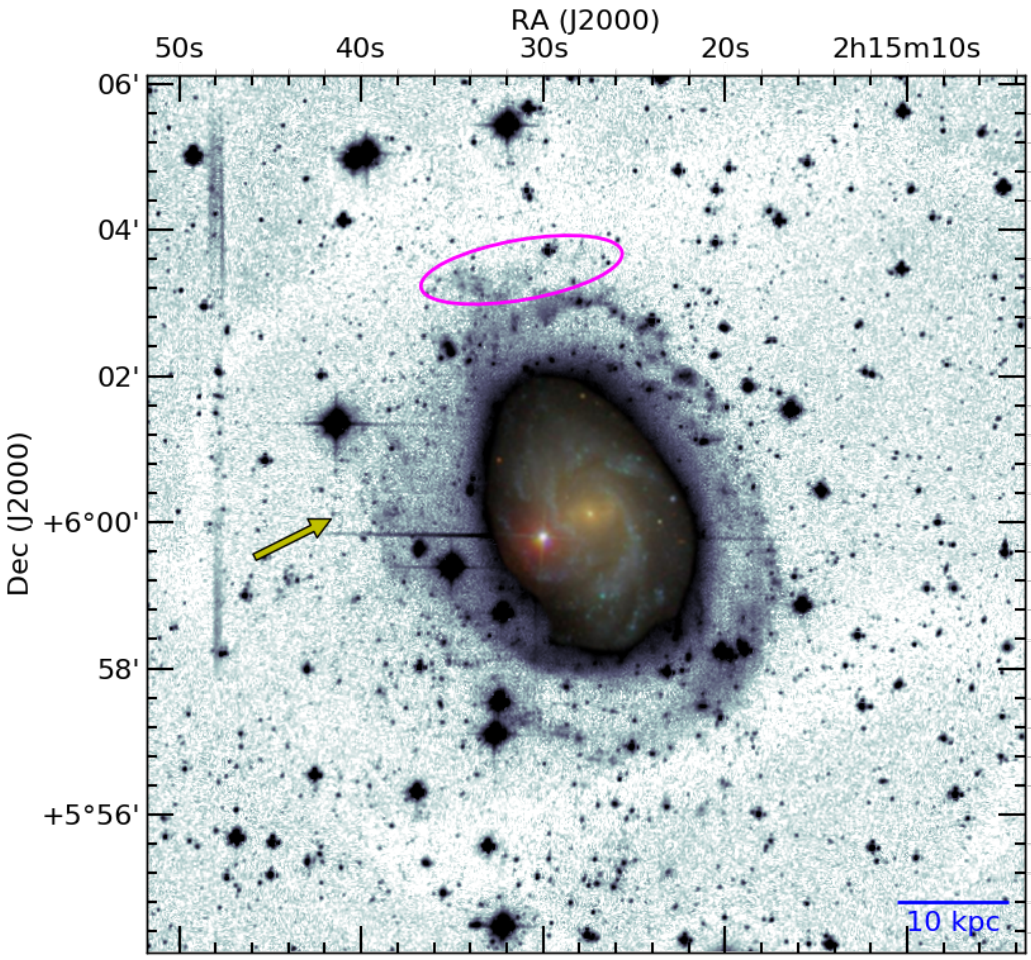

Fig. 3.1 A 12'×12' combined image of the Cousins R image from CAHA2.2m telescope and the three photographic B, G, R images from CAHA1.23m telescope. This particular image is only used to show the outer faint structures of the galaxy (e.g. the pseudoring, the Northern region in a magenta ellipse or the Eastern diffuse emission pointed by the yellow arrow), not for any physical measurement. The inner coloured area corresponds to an SDSS image of CIG 96 down to $\sim$24 mag arcsec^{-2} (SDSS r band) and it is used as reference.

With the aim of studying the colour distribution in the most interesting regions of the galaxy, we built a $g - r$ image with the two images from R and B photographic bands already calibrated to SDSS r and SDSS g bands respectively:

$$g - r = -2.5 * log(F_{SDSS\ g}) + 2.5 * log(F_{SDSS\ r}) \\ = -2.5 * log \frac{F_{SDSS\ g}}{F_{SDSS\ r}} \tag{3.6}$$

where $F_{SDSS\ r}$ and $F_{SDSS\ g}$ are the fluxes of the SDSS r and g images, respectively. The image and analysis of this result are shown in Sect. 4.2.3.

In Fig. 3.1 we show the result of combining the reduced CAHA2.2m image (Cousins R band) and the three reduced CAHA1.23m images (photographic B, G, R filters) altogether. When compared to the better resolution of VST (see Sect. 3.2.1.3), the lower resolution of these images provides a more clear visualisation of the external structures of CIG 96, especially the faint structure to the North and the very diffuse Eastern side of the pseudoring, indicated in the image. However, we cannot calibrate them all to a common band, so this image must be taken only as an illustrative view of the galaxy.

3.2.1.3 VST dataset, data reduction and calibration

In order to study the larger scale structure surrounding CIG 96, we observed the galaxy also with OmegaCAM at the VST (runID: 098.B-0775 A, P.I.: E. Unda−Sanzana) in the nights of October 6^{th}, 9^{th} and 20^{th}, November 1^{st} and 2^{nd} and December 2^{nd}, 3^{rd} and 20^{th}, all in 2016. The instrument has a field of view of 1°×1°sampled with a 32-CCD, 16k×16k detector mosaic at 0.21" pix^{-1} (q.v. Kleijn et al., 2013), allowing for a large coverage of the galaxy surroundings. For comparison, a footprint of the 32 CCDs and the 4 auxiliary CCDs (two in each side, used for guiding and image quality measurement) of OmegaCAM at VST are shown in Fig. 3.2.

The pilot observations of CIG 568 and CIG 879 of our previous program (runID: 093.B-0894 A, P.I.: E. Unda−Sanzana) allowed us to refine the observing strategy by improving the target selection (avoiding those with potentially too close bright stars) and adjusting the exposure times (optimising the on−target and overhead times). The following observations, in which CIG 96 is included, were benefited from these

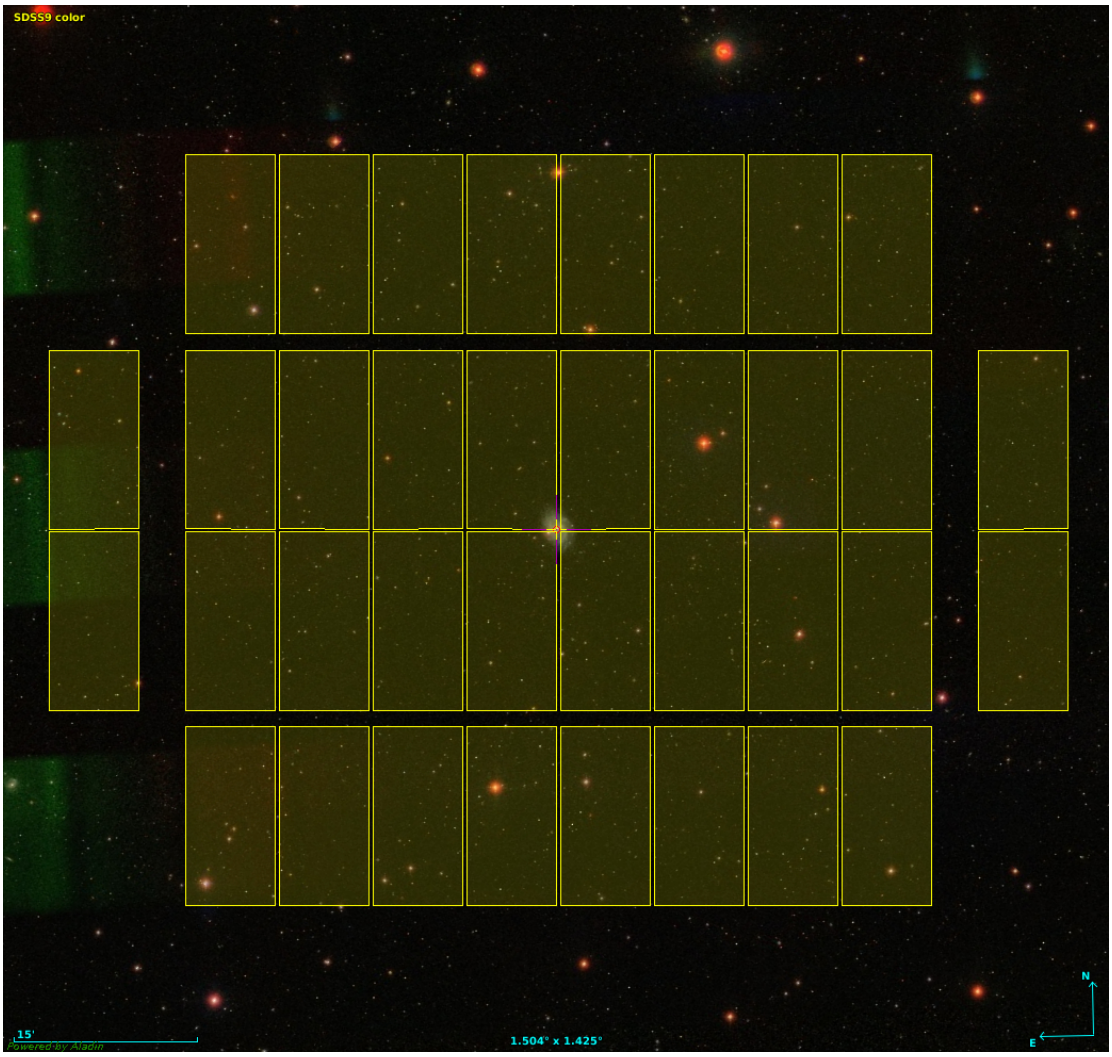

Fig. 3.2 *Background*: SDSS colour image centered on CIG 96. *Foreground*: footprint of the 32 CCDs of OmegaCAM (central regions) along with the 4 auxiliary CCDs (2 in each side).

improvements. A total of 8 observing blocks (OBs) of 1 hour each were dedicated to observe CIG 96 in the dates previously indicated. From these, 7 OBs had 16 exposures and 1 OB had 10 exposures, making a total of 122 exposures of 154 s each, taken in the dates mentioned before. The total time spent on source was of 5h 10 min.

The 32 CCDs used for the imaging have intermediate spaces between the different chips in the vertical direction (5.64 mm top and bottom gaps; 0.82 mm central gap) and in the horizontal direction (1.5 mm gap). Also, at the time these observations were designed, the user manual accounted cross talk between CCDs 93 to 96 at $< 0.4\%$ level

(slightly above our aim of 0.35%). Further discussion with the telescope staff let us know of irregular gain variations in CCDs 82, 87 and 88.

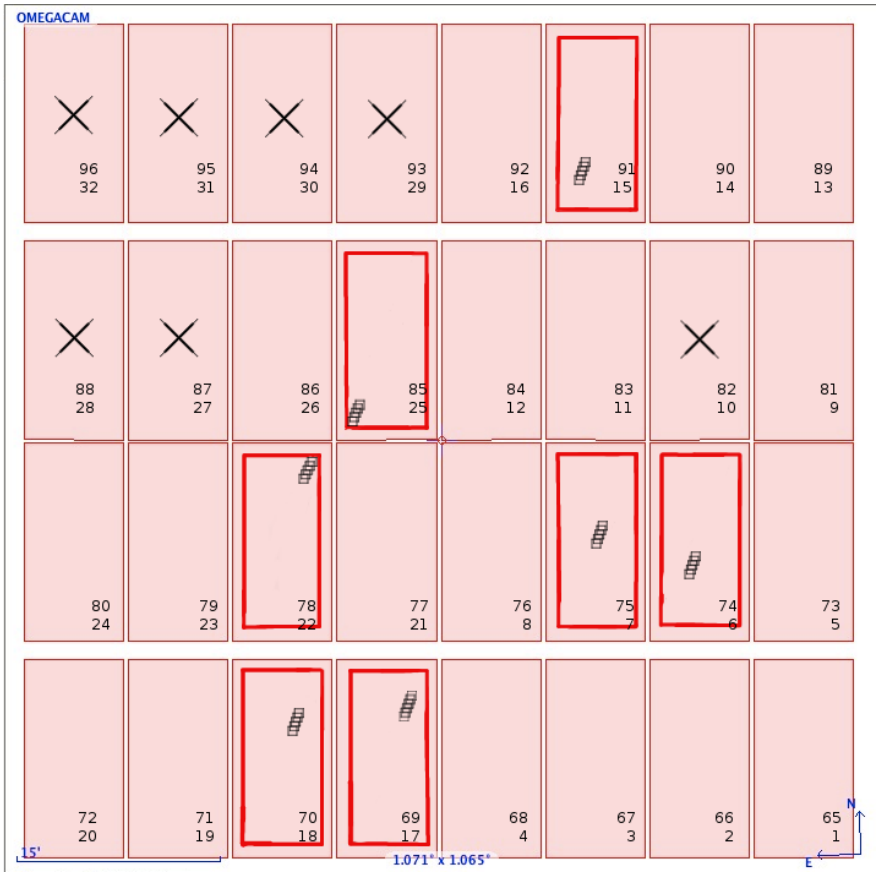

Fig. 3.3 Footprint of the 32 central imaging CCDs of OmegaCAM at VST with a sample set of pointings of CIG 568. We avoided positions in which the galaxy and its close surroundings would fall too close to the CCDs with gain problems (82, 87, 88) or cross talk problems (93 to 96). These are all marked with black crosses. The 49 pointings are distributed in 7 CCDs, each one showing 7 offset pointings (black squares) and spread along a virtual South-East to North-West diagonal. The red regions delimit the region in which the pointings were taken, leaving 1' in RA and Dec with respect to the edge of the CCDs.

In order to avoid as much as possible these seven CCDs and guarantee a homogeneous coverage of the gaps, we initially designed a manual diagonal dithering pattern (see Fig. 3.3) for the pilot observations exposures to sample the galaxy and its surroundings. With it, the 49 different offset positions of the galaxy (7 pointings with 7 offset positions each) were placed along a diagonal oriented from the South-East to

the North-West, always leaving at least 1' (both in RA and Dec) with the edge of the CCDs (see Fig. 3.3).

After the pilot observations, we concluded that the previous diagonal dithering would not significantly differ from the already existing modes (JITTER and DITHER, since STARE was not useful for our aims) so we designed a new manual dithering pattern that would make six pointings to the corresponding apexes of a slightly irregular hexagon-shaped pattern plus one more central pointing. An example of the dithering pattern used for CIG 96, as submitted to the telescope, is shown in the sample OB included in Appendix B. Moreover, in Fig. 3.4 we show the weights image of the observations of CIG 96, i.e. the image that reflects the areas with best coverage of the field.

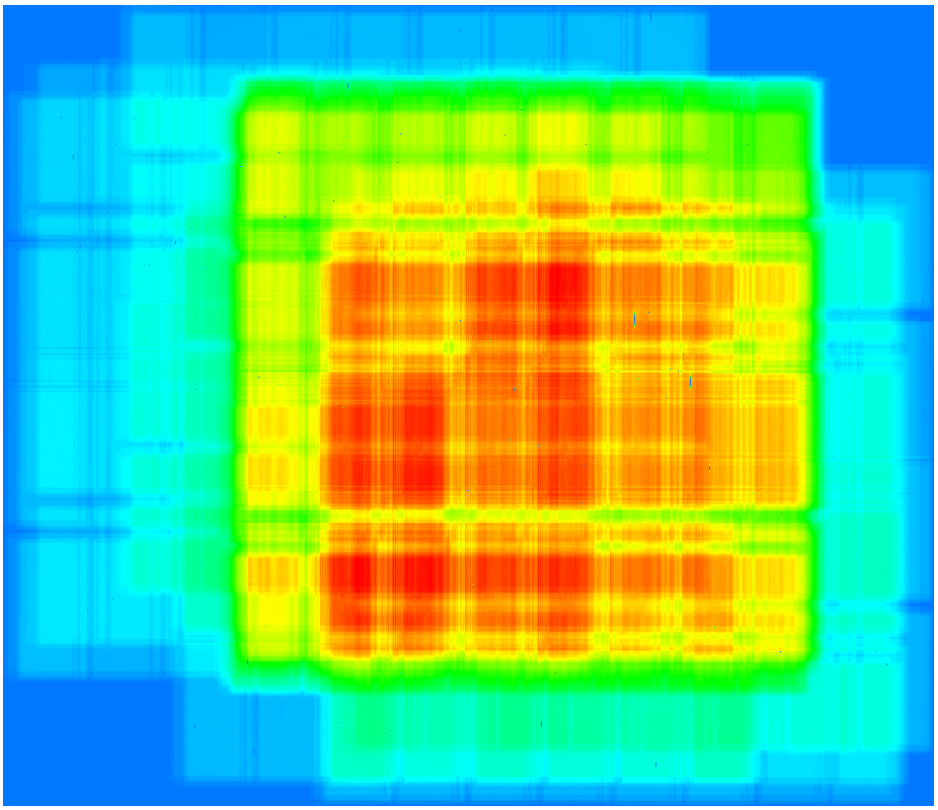

Fig. 3.4 Weights image obtained from the observations of CIG 96 with OmegaCAM at VST. The color−scale reflects high and homogeneous coverage in red (the highest), yellow and green tones, and low and inhomogeneous coverage in cyan and blue (the lowest) tones. For reference, the region delimited in green tones is approximately 62'×62'.

The automatic scheduling of the telescope performs the observations only if all the observing requirements are fulfilled. In our case, all observations were done under the following conditions: photometric sky transparency, maximum seeing of 2.0", airmasses below 2.0 ($>63.4°$), with an angular distance to the Moon of at least 60° and its maximum illumination at 30%.

We used a modified version (Venhola et al., 2017) of Astro-WISE pipeline (Valentijn et al., 2007) to reduce and calibrate these data. A sample script of this process can be found in Appendix C. Fig. 3.5 shows an SDSS colour image of CIG 96

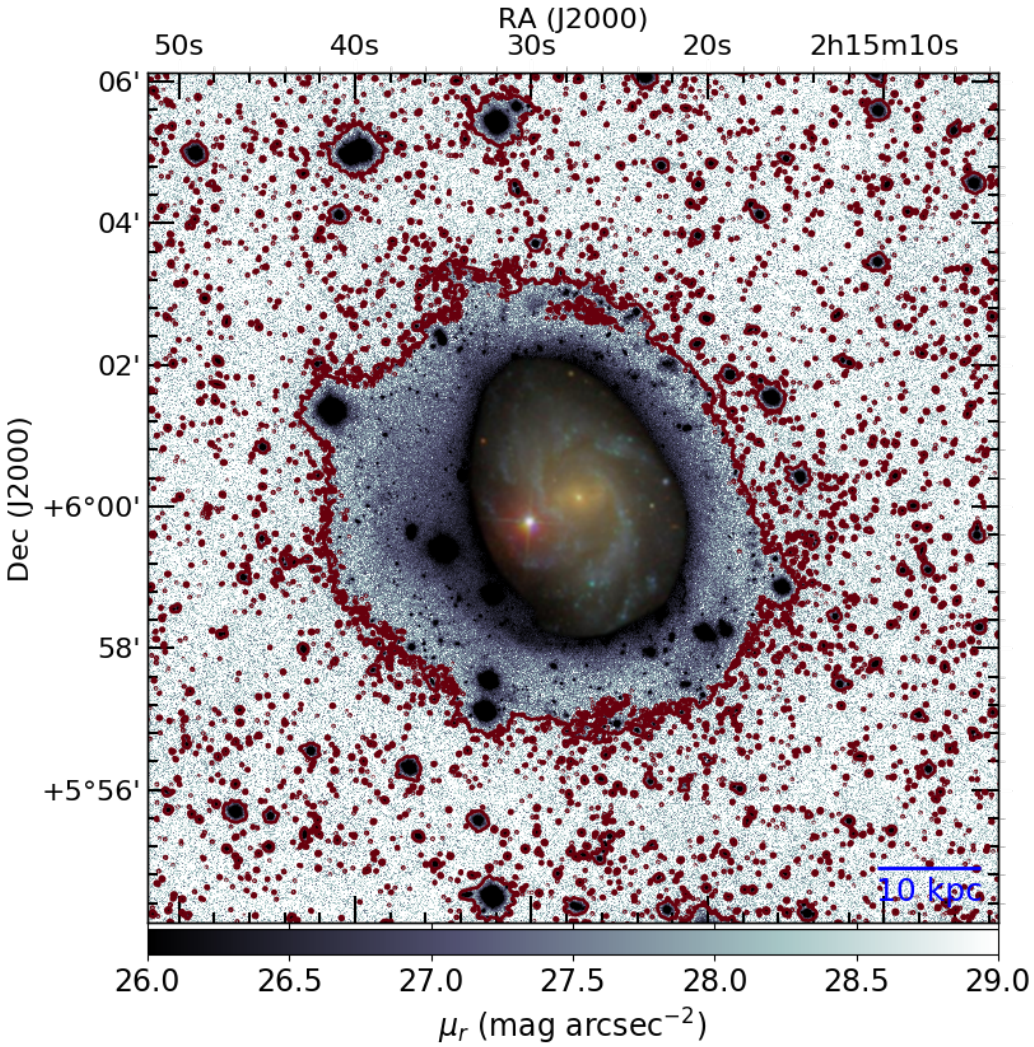

Fig. 3.5 A 12'×12' detail of the VST optical image of CIG 96 with the SDSS colour image down to ∼24 mag arcsec^{-2} (SDSS r). The red contour is set on 26.5 mag arcsec^{-2} (SDSS r), to point out the faintest surface brightness level of the pseudoring.

on top of a 12'×12' region of the VST image. The SB was calculated using equation 3.7, in which the second term corresponds to the conversion from pix^{-2} to arcsec^{-2}:

$$\begin{aligned} \mu_{SDSS\ r} &= -2.5 * log(F_{SDSS\ r}) - 2.5 * log(0.21^2) \\ &= -2.5 * log(F_{SDSS\ r}) + 3.3889 \end{aligned} \tag{3.7}$$

Additionally, the faint SB reached with this image allowed us to detect Galactic cirrus around the galaxy (see Sect. 4.2.6).

3.3 Planck and WISE images of CIG 96

In order to inspect the cirrus around CIG 96 (see Sect. 4.2.6), we have used images from the HFI camera of the Planck satellite at 857 GHz / 350 μm band (Planck Collaboration et al., 2014). Also, we have used a WISE band 3 image (12 μm) since this band that traces hot dust and shows good correlation with the cirrus emission (Miville-Deschênes et al., 2016). This image, kindly provided by T. Jarrett, consists of mosaics constructed from single native frames using a drizzle technique (Jarrett et al., 2012), re-sampled with pixels of 1"×1" each (relative to a 6" FWHM beam).

Throughout this work and for simplicity, we will refer to these images as Planck857 and WISE3, respectively. Planck857 images were obtained from SkyView online tool (McGlynn and Scollick, 1994) while the WISE3 image was obtained from the IRSA, NASA/IPAC archive and reprocessed to improve the flat fielding and remove the stars.

Chapter 4

The faint features of CIG 96: results and analysis

Our new HI and optical data of CIG 96 show the body and some new features in the outskirts of the galaxy with unprecedented detail. This chapter contains the analysis of the HI cube described in Sect. 3.1.2.3 and 3.1.3. Moreover, the CAHA and VST optical data (see Sect. 3.2.1.1, 3.2.1.2 and 3.2.1.3) have revealed the morphology and colour of the pseudoring as well as the outskirts of the galaxy at very faint surface brightness levels.

4.1 HI results

In this section I present the results of the distribution and kinematics of the atomic hydrogen in the main body and surroundings of CIG 96. The central velocity and asymmetry of the galaxy are calculated and compared to previous results. The identification of structures is done via the channel maps, the integrated flux density map, the velocity field map and the position−velocity cuts over the major and minor axes of the wavelet filtered HI cube.

4.1.1 Integrated emission, central velocity and asymmetry level

To calculate the total spectrum of the HI cube, we integrated the emission of each of the 48 channels. As discussed by Fouqué et al. (1990), we then computed the central velocity of the galaxy V_{cen} as the average between the lowest and highest velocities measured at a width (or flux level) of the 20% of the highest flux peak in the integrated spectrum (abbreviated $W20$, name varies depending on the percentage used). The error can be estimated as: $\Delta V = 4\,\frac{\sqrt{\delta\nu\,(W20-W50)/2}}{SNR_{peak}}$ where $\delta\nu$ is the spectral resolution of the cube, $(W20 - W50)/2$ represents the steepness of the edges of the HI profile at 20% and 50% of the maximum flux, and SNR_{peak} is the signal-to-noise ratio to the maximum flux peak. Taking these into account, the $W20$ central radio velocity of our HI cube is $V_{LSRK}\,(CIG\,96) = 1544.15 \pm 0.23$ km s^{-1}. The integrated spectrum of CIG 96 is shown in Fig. 4.1, top panel.

We find a difference of approximately 10 km s^{-1} between our result for the central velocity of CIG 96 and those calculated from single-dish data by E05 (same method as in this work) and Haynes et al. (1998), 1561.6 and 1562 ± 1 km s^{-1}, respectively, both in heliocentric frame of reference, i.e., approximately 1553 and 1554 km s^{-1} when converted to LSRK, as is ours. Kerr and Lynden-Bell (1986) also provide a LSRK velocity of 1553 ± 1 km s^{-1}, showing the same shift with respect to our result. To locate the reason for this apparent inconsistency, we recalculated the central velocity of our HI cube and the one published by E05 in different standards of rest and in the two optical and radio velocity conventions. In all cases, the differences remained within a few km s^{-1}, i.e., no change in the standard of rest or velocity convention would account for such a shift. The calibration process was also revised and the correct rest frequency for the HI line was confirmed, leaving us with the only hypothesis of an undetected error in the raw data or the calibration process. Taking this into account, we conclude this difference may be assumed, since it is a small shift compared to the width of the profile, not to affect the interpretation of the data in any case.

CIG 96 has a close companion: NGC 864 COM01 (hereafter also referred as the companion), detected in HI by E05. We determine a $W20$ central radio velocity of V_{LSRK} (companion) $= 1577.90 \pm 2.62$ km s^{-1}. The HI and optical properties of this

neighbouring galaxy, as well as its implication in the isolation of CIG 96, are discussed further in Sect. 4.1.4, 4.2.5 and 5.1.

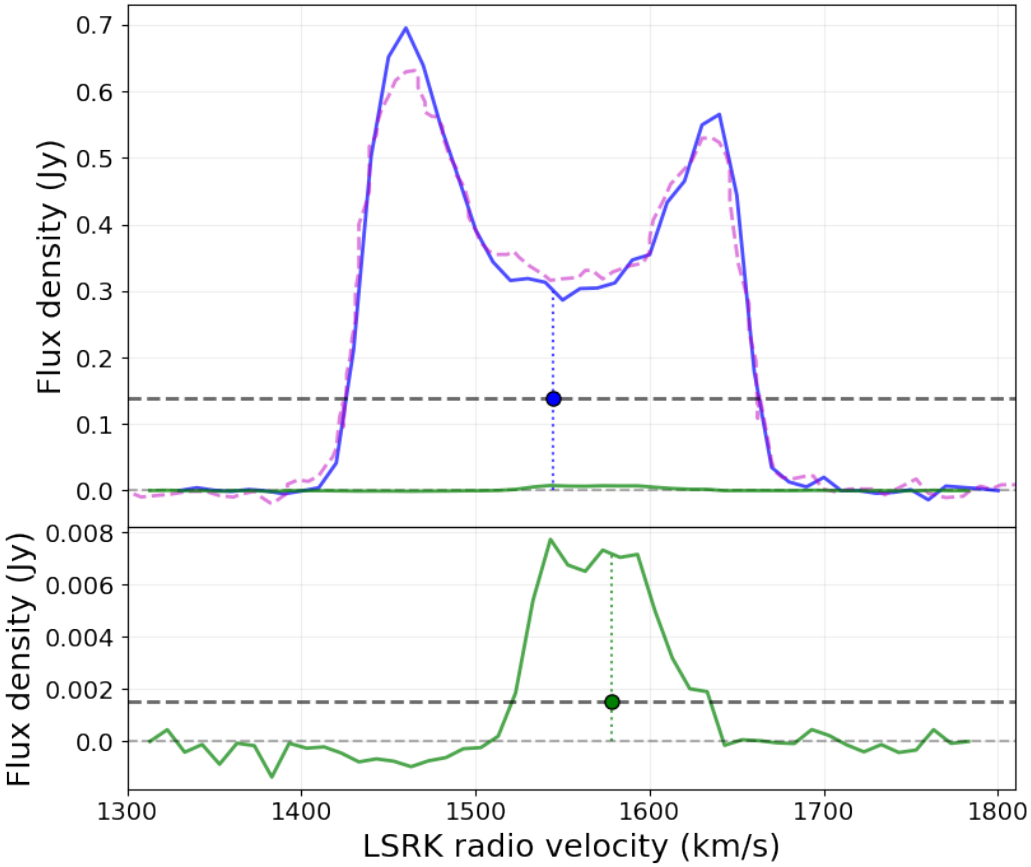

Fig. 4.1 *Top panel*: in blue solid line, integrated profile of CIG 96, calculated from the EVLA and VLA combined HI cube. In pink dashed line, the integrated spectrum of CIG 96 (LSRK) obtained by Haynes et al. (1998) at Green Bank 43 m (heliocentric). Our integrated spectrum shows a central velocity that is lower than the Green Bank spectrum so, in order to match and facilitate the comparison between the two, we have shifted the latter by -17 km s^{-1}. The green solid line is the integrated profile of the closest companion of CIG 96: NGC 864 COM01. The horizontal green dashed line sets the width at 20% of the highest flux peak ($W20$) for the central radio velocity computation, shown as a blue dot (V_{LSRK} $(CIG\ 96)$ = 1544.15 km s^{-1}). The vertical blue dotted line defines the two halves of the spectrum for the asymmetry parameter calculation. *Bottom panel*: integrated HI profile of the companion NGC 864 COM01 with a rescaled flux density for an easier visualisation. The green dot sets the central velocity of this galaxy (V_{LSRK} $(companion) = 1577.90$ km s^{-1}).

In Fig. 4.1 we compare the integrated emission spectra derived from our HI cube for CIG 96 and its companion (bottom panel) with the one obtained by Haynes

et al. (1998) using data from Green Bank 43m single dish telescope, and still in the heliocentric system of reference. For a better comparison between the two spectra, we have shifted the latter by -17 km s^{-1}. The perfect match between them strongly suggests that our HI cube has a velocity shift of -10 km s^{-1}, after converting all velocities to LSRK.

As described in Sect. 2.2.1, the HI integrated spectrum is necessary to estimate the HI asymmetry level of a galaxy, quantified as $\mathcal{A}_{1/h}$ (e.g. Haynes et al., 1998; Kornreich et al., 2001; Espada et al., 2011b). This areal asymmetry parameter provides a simple quantification of the gas distribution in the two halves of the galaxy, but it does not give spatial information of any possible asymmetry.

We calculated the sources of the uncertainties of this parameter as described by E11b:

- the *rms of the HI profile* σ: the uncertainty of each of the two halves, S_1 and S_2, is described as: $\Delta S_i = \sqrt{N_i}\sigma R$, where N_i is the number of channels of the side measured and R is the spectral resolution of the profile. The absolute error accounted for both sides as: $\Delta A_{rms} = \left[\left(\frac{\Delta S_1}{S_1}\right)^2 + \left(\frac{S_1}{S_2^2}\right)^2 \Delta S_2^2\right]^{1/2}$;
- the *measurement of the central velocity*: the error for each side with respect to half the strongest peak F_{max} is: $\Delta S_i = \Delta V \times 0.5 \times F_{max}$;
- and the *pointing offset*: negligible in this case, it is only relevant when the primary beam is about the size of the galaxy, not the case for our data of CIG 96.

From our data, $\Delta S_i = 0.04$, $\Delta A_{rms} = 0.006$ and $\Delta A_{Vel} = 0.001$. The total error $\Delta A_{flux\ ratio}$ is the quadratic sum of ΔA_{rms} and ΔA_{Vel} so our asymmetry level estimation, we compute a value of $A_{flux\ ratio} = 1.16 \pm 0.01$, i.e. $16 \pm 1\%$, in full concordance with E05.

4.1.2 Channel maps

The channel maps allow to inspect every channel of the HI datacube. Each one corresponds to a different velocity and let us trace any structures that might be

connected to the gaseous envelope of the galaxy. In Fig. 4.2 we show a subset of the channel maps of the wavelet filtered HI cube on top of the CAHA1.23m optical image (band R) of CIG 96. This image corresponds to the central 25'×25' of the primary beam and to the channels with emission, i.e., from 1380 to 1690 km s^{-1} (channels 6 to 37, respectively) where the channel width is 10 km s^{-1}. The systemic velocity of the galaxy (V_{LSRK} $(CIG\ 96)$ = 1544.15 km s^{-1} see Sect. 4.1.1) corresponds to channel 23 and the approaching and receding sides of the galaxy extend approximately 135 and 145 km s^{-1}, respectively. The synthesised beam is 28"×28", the rms is 0.126 mJy beam^{-1} and the column density reached is $N_{HI} = 8.9 \times 10^{18}\, cm^{-2}\, (5\sigma)$.

The HI distribution is more symmetrical in the central channels (approximately between ∼1500 and 1600 km s^{-1}) than in those with velocity differences of $\Delta V \geqslant 60$ km s^{-1} with respect to the central velocity. In the latter, the approaching side shows that the HI has an uniform distribution over a larger area in the South-West than in the receding, where the distribution is more narrow and oriented towards the North-East. The HI extension also differs, reaching ∼7.9' (∼47 kpc) towards the South-West and ∼9.3' (∼55 kpc) towards the North-East. Also, the receding Northeastern side is less massive, as reflected in the asymmetrical shape of the integrated spectrum (Sec 4.1.1). In both the approaching and receding sides, the HI is extended beyond $4\times r_{25}$ of the optical extension. From 1630 to 1670 km s^{-1} (channels 31 to 35), there is a change in the orientation of the HI, especially visible in column densities below 1.0×10^{19} cm^{-2} (outer contours of Fig. 4.2 and moment maps shown in Sect. 4.1.3).

Focusing on the outskirts, we have found two previously undetected features that are discussed further in Sect. 5.2:

- First, the NW HI feature. We notice a clumpy structure from 1480 to 1550 km s^{-1} (channels 16 to 23), to the North-West of the galaxy ($\alpha = 02^h15^m05.9^s$, $\delta = 6°03'03"$), with an approximate size of ∼21 kpc (∼3.5', measured from channel 17 to 22), a column density of $N_{HI}^{NW} \simeq 6.5\times10^{19}$ cm^{-2} and a total HI mass of $M_{HI}^{NW\ feat.} \simeq 3.1 \times 10^6 M_\odot$. The NW HI feature is indicated with green marks in Fig. 4.2.

- Second, the SE HI feature. A structure shows up from 1600 to 1640 km s^{-1} (channels 28 to 32), to the South-East of the galaxy ($\alpha = 02^h15^m41.0^s$, $\delta = 5°55'31"$),

within a region of approximately 8.8×8.8 kpc (∼90”×90”), with a column density

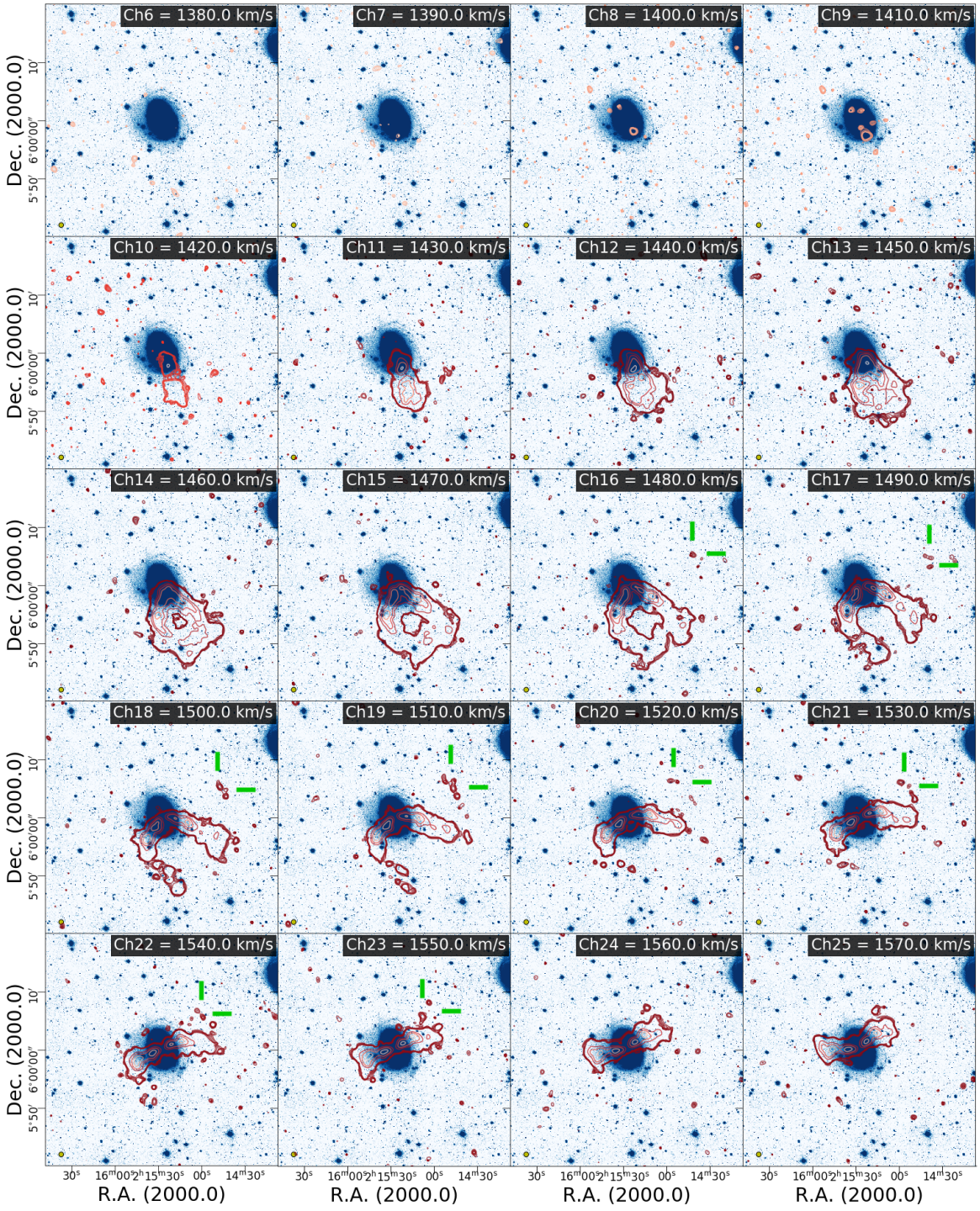

Fig. 4.2 *Continues.*

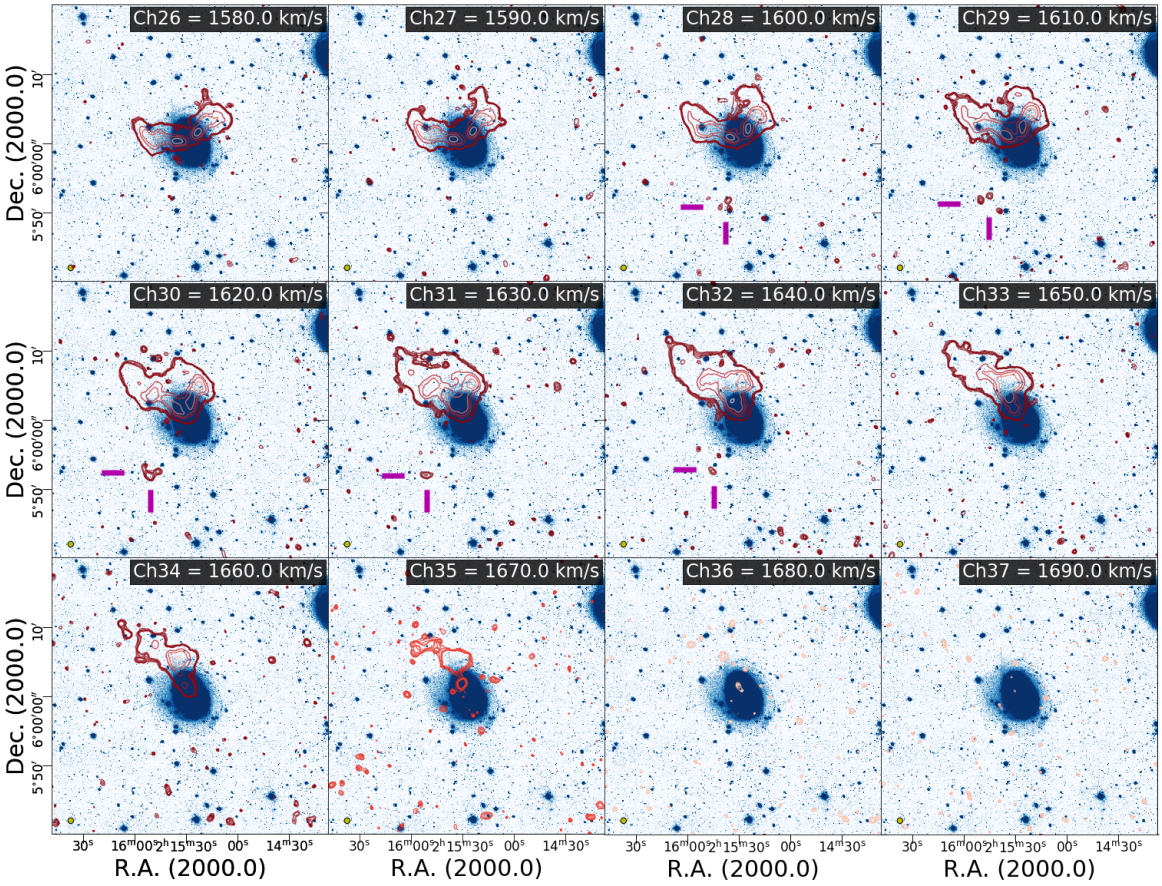

Fig. 4.2 Channel maps of the wavelet filtered HI cube superimposed on the VST optical image of CIG 96. The field of view is approximately 25'×25' (147×147 kpc). *Foreground*: the red contours correspond to 3.4, 3.9, 4.5, 5.1, 5.6, 28.1, 56.2, 112.5 and 224.9 σ levels ($rms = 0.126$ mJy beam^{-1}, 1σ) or the equivalent HI column densities of 0.6, 0.7, 0.8, 0.9, 1.0, 5.0, 10.0, 20.0, 40.0 $\times 10^{19}$ cm^{-2}, respectively. Green and magenta marks indicate the NW and SE HI features, respectively. The synthesised beam of 28"×28" is shown in the bottom left corner as a yellow circle. *Background*: VST image of CIG 96. We display a surface brightness range of $\mu_{r\ SDSS} = 26.0 - 28.4$ mag arcsec^{-2} to enhance the outskirts of the galaxy while brighter inner structures are not shown.

of $N_{HI}^{SE} \simeq 4.9\times10^{19}$ cm^{-2} and a total HI mass of $M_{HI}^{SE\ feat.} \simeq 1.6 \times 10^6 M_\odot$. The SE HI feature is indicated with magenta marks in Fig. 4.2.

A complementary visualisation of the channel maps is shown in Fig. 4.3. Taking the central velocity of the galaxy as reference (1544.15 km s^{-1}), the emission of the immediately approaching (1550 km s^{-1}, channel 23, in red) and receding (1540 km s^{-1}, channel 22, in blue) channels is displayed on the top left frame. For each following

frame, the emission shown corresponds to the next pair of equidistant channels, i.e. increasing and decreasing one channel (or 10 km s^{-1}) at a time.

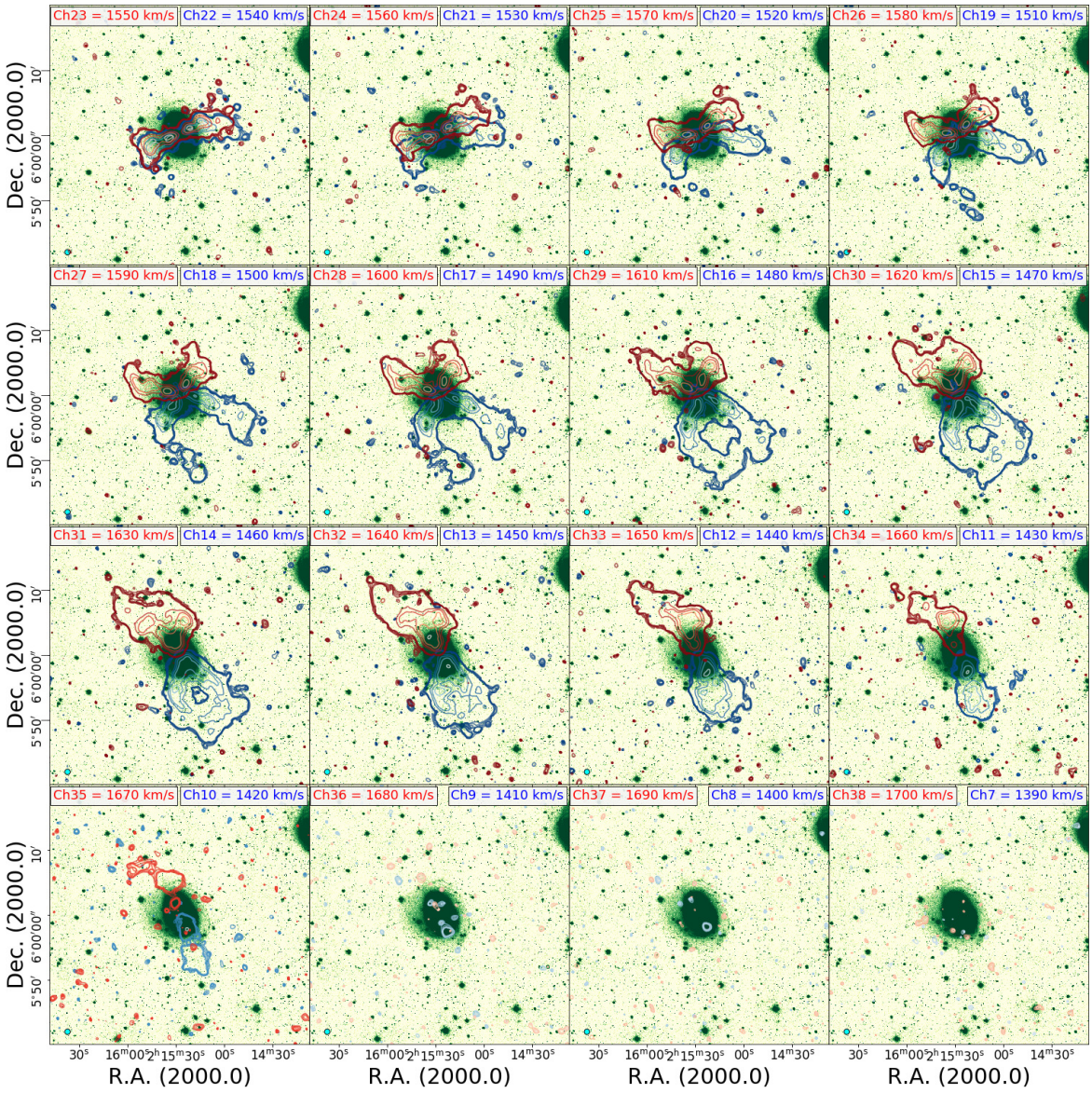

Fig. 4.3 Paired channel maps of the wavelet filtered HI cube superimposed on the VST optical image of CIG 96. Each frame shows the equidistant emission from both the approaching (red) and receding (blue) channels with respect to the central velocity of CIG 96 (V_{LSRK} $(CIG\ 96)$ = 1544.15 $km\,s^{-1}$), increasing 10km s^{-1} (one channel) at a time. The cyan circle at the bottom left represents the beam size of 28"×28".

We confirm the previously observed symmetrical and asymmetrical distribution. The emission is fairly homogeneous and symmetrical in the approximate channels range of 20 to 25, i.e. the inner ∼50 km s^{-1}, from 1520 to 1570 km s^{-1}. In the following pairs,

the emission of the approaching channels is visibly more extended and regular than the receding, tilted to the East with respect the approaching emission. This is specially noticeable in the pairs 32−13 (1640−1450 km s^{-1}) and 33−12 (1650−1420 km s^{-1}).

4.1.3 Moment maps and position-velocity profiles

The integration of the flux density S (or 0^{th} moment) is carried out from channel 6 (1380 km s^{-1}) to channel 38 (1700 km s^{-1}), i.e. one additional channel beyond the HI emission. The velocity field (or 1^{st} moment) is the intensity-weighted velocity of the spectral line, i.e., a measure for the mean velocity of the gas. They are computed with the following relations:

$$M_0 = \int S \, dv \tag{4.1}$$

$$M_1 = \frac{\int v \, S \, dv}{\int S \, dv} \tag{4.2}$$

4.1.3.1 Integrated flux density map (0th moment)

The 0^{th} moment is shown in Fig. 4.4 and later in 4.9. The HI extends beyond $4\times r_{25}$, i.e., approximately up to 50 kpc (8.5'), reaching an integrated column density of $N_{HI} = 1.2 \times 10^{20}$ cm^{-2} (5σ) with a beam size of 28"×28". As a comparison, in Fig. 4.4 we indicate with a black line the approximate $N_{HI} = 8.7 \times 10^{20}$ cm^{-2} (5σ) column density reached by E11a with a beam size of 16.9"×15.6". Quantitatively, our observations are roughly ∼7 times deeper than the previous ones.

4.1.3.2 Velocity field map (1st moment)

The $1st$ moment is shown in Fig. 4.5. It allows the estimation of the position angle (from now on, PA) of the major and minor kinematical axes of the galaxy, indicated by the two black lines at PA = 20° and PA = 110° respectively.

The synoptic vision of pairs of equidistant iso-velocity lines of the velocity field is shown in Fig. 4.6 and confirms the patterns of the previous channel maps of Fig. 4.2

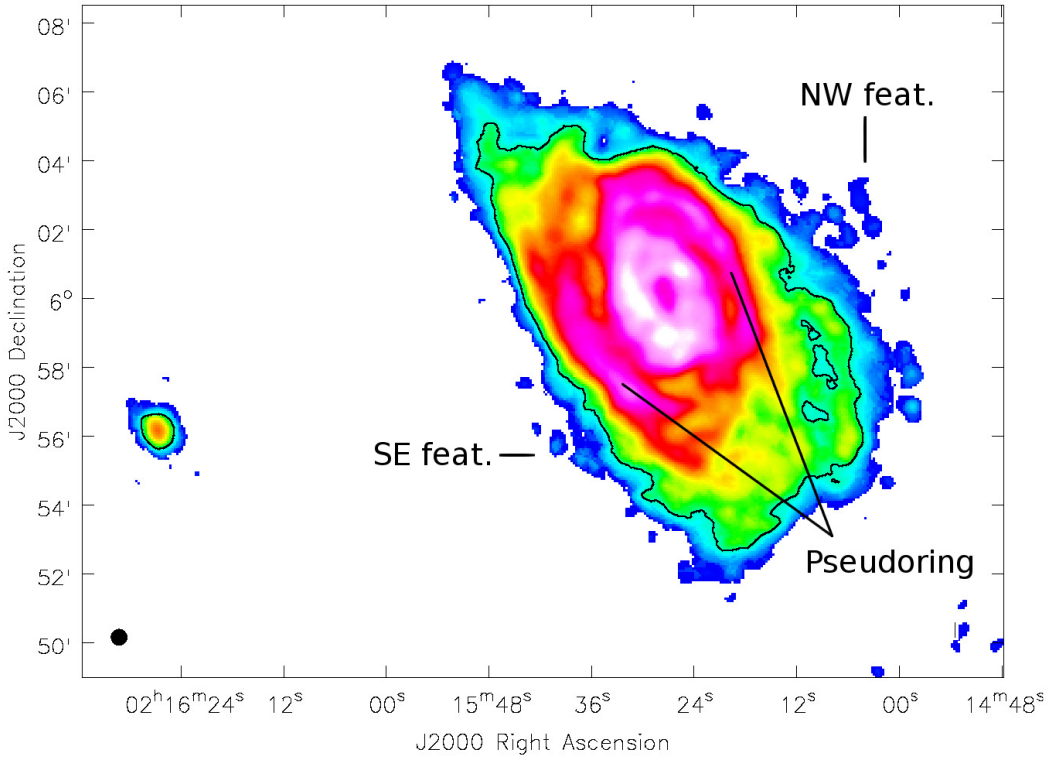

Fig. 4.4 HI integrated intensity map of CIG 96 and the companion after a 3.5σ blanking (see Sect. 3.1.4). We identify the NW and SE HI features mentioned in Sect. 4.1.2 as well as the HI emission of the pseudoring. The black contour represents the column density of $N_{HI} = 8.7 \times 10^{20}$ cm^{-2} (5σ) reached by E11a. The black circle at the bottom left represents the beam size of 28"×28".

and 4.3. The pairs are approximately homogeneous within the first ∼50 km s^{-1} with respect to the central velocity of the galaxy (1544.15 km s^{-1}, see Sect. 4.1.1), i.e. from the central velocity up to approximately the 1594 / 1494 km s^{-1} pair. However, from the 1604 / 1484 km s^{-1} pair up to the farthest 1644 / 1444 km s^{-1} pairs, the kinematic signature shows growing and larger differences, namely, the receding side (red contours) shows an increasing tilted orientation towards the East reaching a PA $\simeq 40°$ with respect the more homogeneous approaching side (blue contours) that approximately maintains the major axis orientation at PA = 20°. It is also noticeable that the receding side keeps an increasing rotation velocity up to the most distant emission while the approaching side does not, as shown in the closed contours from ∼1464 km s^{-1} down to 1440 km s^{-1}. This is easily visible in the position-velocity cuts of Sect. 4.1.3.3.

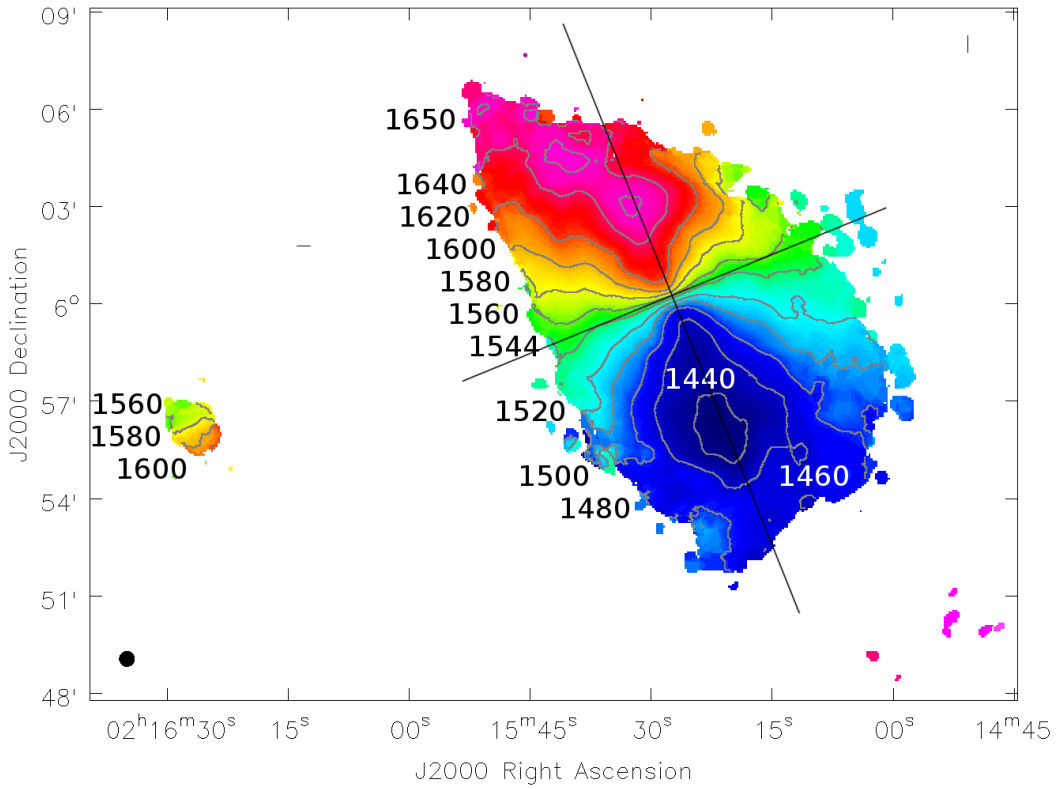

Fig. 4.5 HI velocity field map of CIG 96 and the companion after a 3.5σ blanking (see Sect. 3.1.4). The black lines indicate the orientation of the major and minor axis ($PA_{maj} = 20°$ and $PA_{min} = 110°$, respectively) along which the position-velocity cuts have been performed (see Fig. 4.7). Grey contours represent the indicated velocities in $km\,s^{-1}$. The black circle at the bottom left represents the beam size of 28"×28".

4.1.3.3 Position-velocity cuts

We have performed the position-velocity profiles (or P/V cuts) over the HI cube along the major and minor axes, as shown in Fig. 4.7.

The emission located at the largest radius in the Southwestern region is indicated with a cyan arrow in the top panel of Fig. 4.7, the P/V cut over the major axis. It is visible in the channel maps at $1450 - 1470\ km\,s^{-1}$ (channels 13 to 15) and it shows a drop in velocity of about $30 - 40\ km\,s^{-1}$ with respect to inner parts of the galaxy. This feature was already detected by E05 and both its extension and velocity drop we measured are in agreement with the results of such work. The interruption in the emission to the North-East is due to a $\sim 3 \times 3\,kpc^2$ region (~30"×30") with low HI

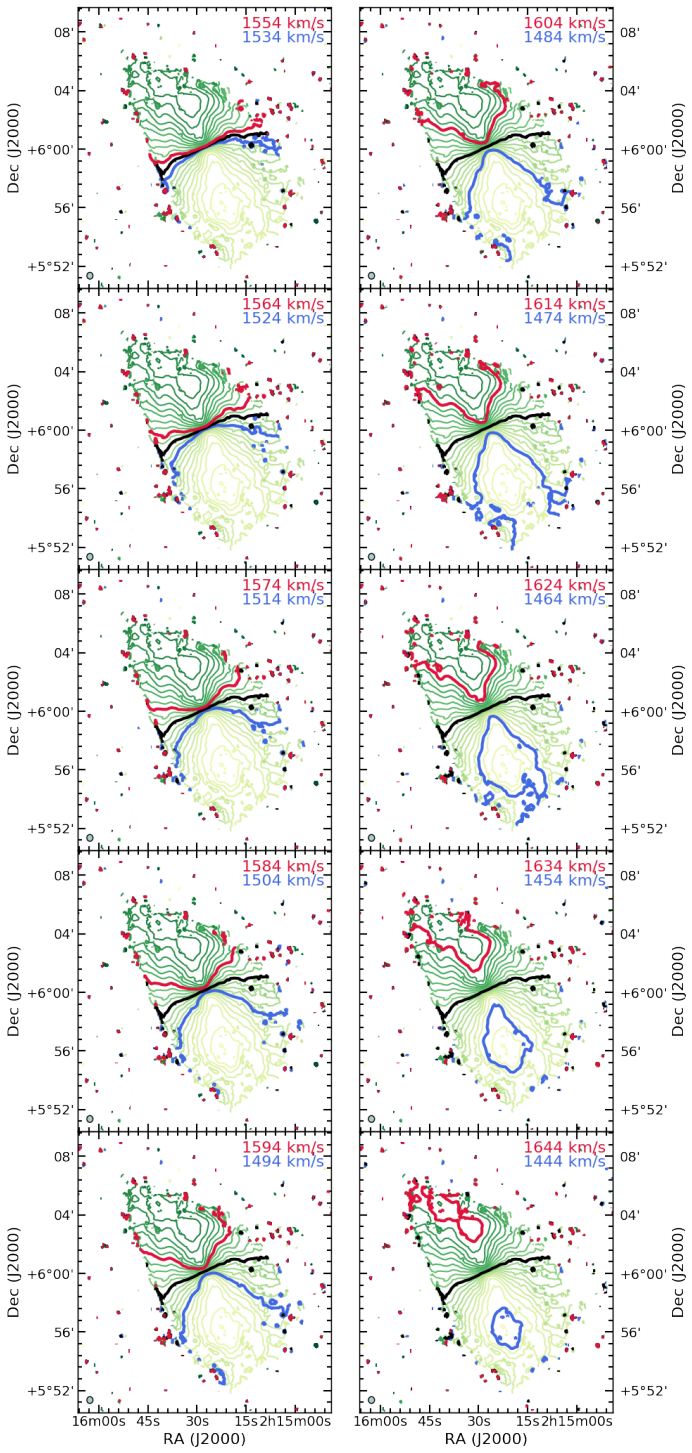

Fig. 4.6 Evolution of symmetrical iso-velocity lines of the 1^{st} moment map (green gradient). Every pair of approaching/receding velocity lines (indicated in red and blue, respectively) are drawn at the same and multiple of 10 velocity increments from the central velocity of CIG 96, that is indicated as a black solid line at V_{LSRK} $(CIG\ 96)$ = 1544.15 $km\,s^{-1}$. The grey circle at the bottom left represents the beam size of 28"×28".

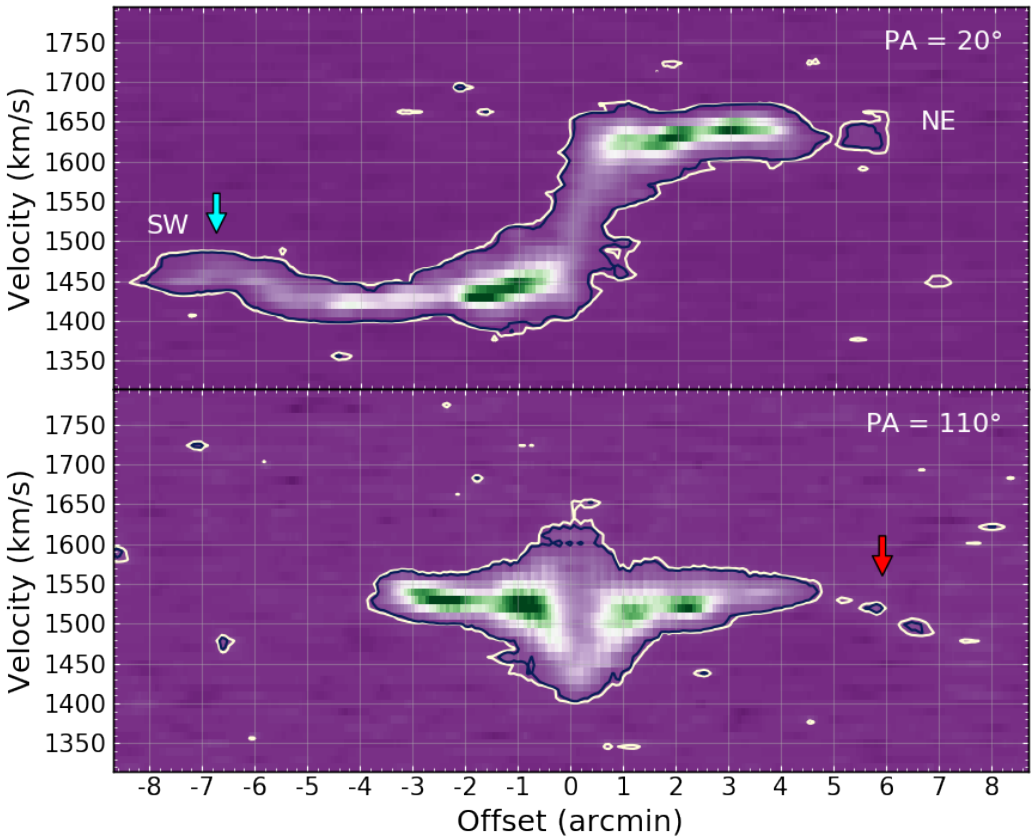

Fig. 4.7 Position-velocity cuts along the major axis (*top panel*, PA = 20°) and minor axis (*bottom panel*, PA = 110°) of CIG 96 HI cube. The column density is $N_{HI} = 0.24 \times 10^{20}\,\mathrm{cm}^{-2}$ (1σ) and the white and black contours correspond to 3.5σ and 5σ, respectively. The cyan arrow points to the Southwestern region where the velocity increases by approximately $30 - 40\ \mathrm{km\,s}^{-1}$ (see Sect. 4.1.3). The red arrow points to the NW HI feature, the clumpy structure detected visible in channels 16 to 23 of the HI cube (see Sect. 4.1.2). As a reminder, the beam resolution is of 28"×28".

emission. It is visible in the 0^{th} moment map ($RA = 2^h15^m34.935^s$, DEC = 6°04'33.17") as well as in the channel maps at $1630 - 1640\ \mathrm{km\,s}^{-1}$ (channels 31 and 32).

The P/V profile over the minor axis cuts through part of the NW HI feature (indicated with a red arrow, Fig. 4.7, bottom panel), the clumpy HI structure mentioned in Sect. 4.1.2. This feature shows a velocity gradient of ∼70 $\mathrm{km\,s}^{-1}$ (approximately from 1480 to 1550 $\mathrm{km\,s}^{-1}$) and it seems to connect with the galaxy in the channels around its central velocity (channels 23 to 25). Also, the central part of the galaxy shows emission in a wide range of velocities with respect to the central velocity. We discuss this effect further in Sect. 5.2.

4.1.4 NGC 864 COM01, HI rich companion of CIG 96

As described by E05 and introduced in Sect. 4.1.1, CIG 96 has a small companion located at 15.2' (∼90 kpc) to the East. It has a B magnitude of $m_B = 16.38$ mag, a central LSRK velocity of $V_{hel} = 1577.90$ km s^{-1} and a total HI mass of $M_{HI} = 4.2 \times 10^6\, M_\odot$. Both CIG 96 and the companion share a similar orientation of their minor axis. However, they show different kinematical orientation, i.e., as shown in the 1^{st} moment map of Fig. 4.8, right panel (along with the 0^{th} moment, left panel), the companion is counter-rotating with respect to CIG 96, and we do not find any signs of tidal interactions between them.

4.2 Optical data results

This section contains the analysis of the optical images of CIG 96, namely, the description of the optical features of CIG 96, the $g - r$ colour image built from CAHA1.23m images (see Sect. 3.2.1.2 for description and calibration of data) to study the colour of the pseudoring and the radial profiles in different position angles.

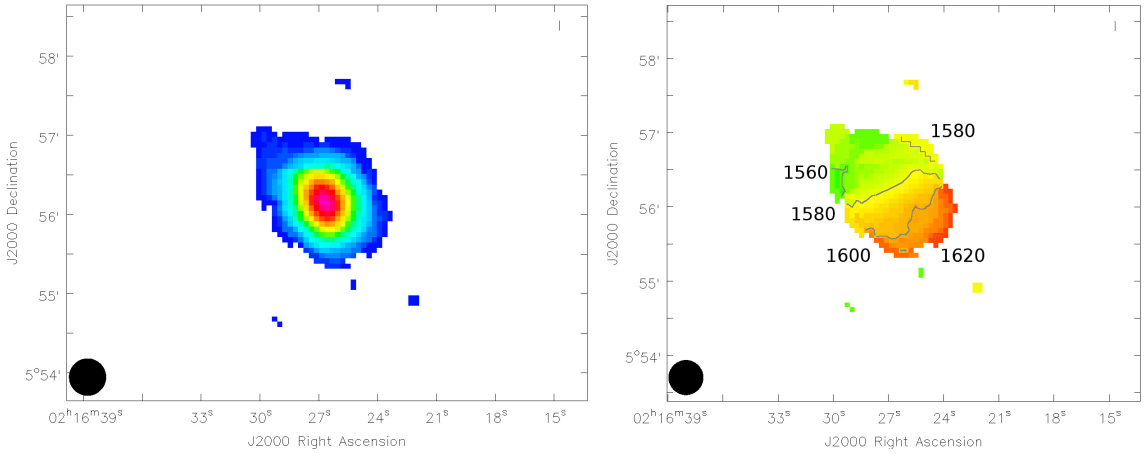

Fig. 4.8 Moment maps of the companion of CIG 96. *Left panel*: HI integrated intensity map after a 3.5σ blanking (see Sect. 3.1.4). *Right panel*: HI velocity field map after a 3.5σ blanking. Grey contours represent the indicated velocities in km s^{-1}. The black circles at the bottom left of each panel represents the beam size of 28"×28".

4.2.1 Surface brightness limit and optical features

The images from CAHA2.2m and CAHA1.23m telescopes have a field of view of 12′×12’, i.e. approximately 71×71 kpc (see Fig. 3.1), while the VST covers 1°×1°, i.e. approximately a 350×350 kpc field centered on the galaxy that also allows overlapping the whole HI image (see a partial image of VST and the HI data in Fig. 4.9). The limiting surface brightness reached is deeper than any other previously published, in particular with the VST image ($\mu_{r\ SDSS}(VST) = 28.7\,\mathrm{mag\,arcsec^{-2}}$, see Fig. 3.5) that reveals unprecedented detail of the extension, boundaries and structures of the external and faint pseudoring of CIG 96 as well as its connection to the inner parts of the galaxy. VST image also shows signs of Galactic cirrus (See Sect. 4.2.6) so we set our reliable detection limit in $\mu_{r\ SDSS}(VST) = 28.4\,\mathrm{mag\,arcsec^{-2}}$, just above the level they start to show up.

The brightest stellar structures within the pseudoring ($\mu_{R\ Cous}\,(CAHA) = 25.5 - 26.5\,\mathrm{mag\,arcsec^{-2}}$) are located within a distance of $r = 1.5 - 2.0 \times r_{25}$ from the galaxy center (i.e. approximately 3.5’ − 4.7’ or 15.0 − 20.5 kpc). They are well defined and large to the North, thinner to the West and more diffuse to the South (see Fig. 3.5). The Eastern region shows very diffuse emission and no clear sign of the pseudoring structure, making the latter a partially closed pseudoring. Despite the surface brightness limit reached, the numerous stars in the field and their PSFs may play a relevant role by overlapping with any fainter emission at such low surface brightness, mimicking non existing extragalactic stellar traces (Trujillo and Fliri, 2016). In particular, this occurs in the Eastern region where a few bright stars are located. However, the even deeper surface brightness limit reached with VST image has two immediate implications: one, the definition of certain regions of the pseudoring are greatly improved and two, the Galactic cirrus start becoming clearly visible at 28.5 $\mathrm{mag\,arcsec^{-2}}$, hindering the detection of features beyond the pseudoring at surface brightness fainter than this level (see Sect. 4.2.6).

4.2.2 Disc and pseudoring relative orientation

A visual inspection of the CAHA2.2m optical image suggested an apparent misalignment between the pseudoring and the galactic disc. In order to quantify it, we performed

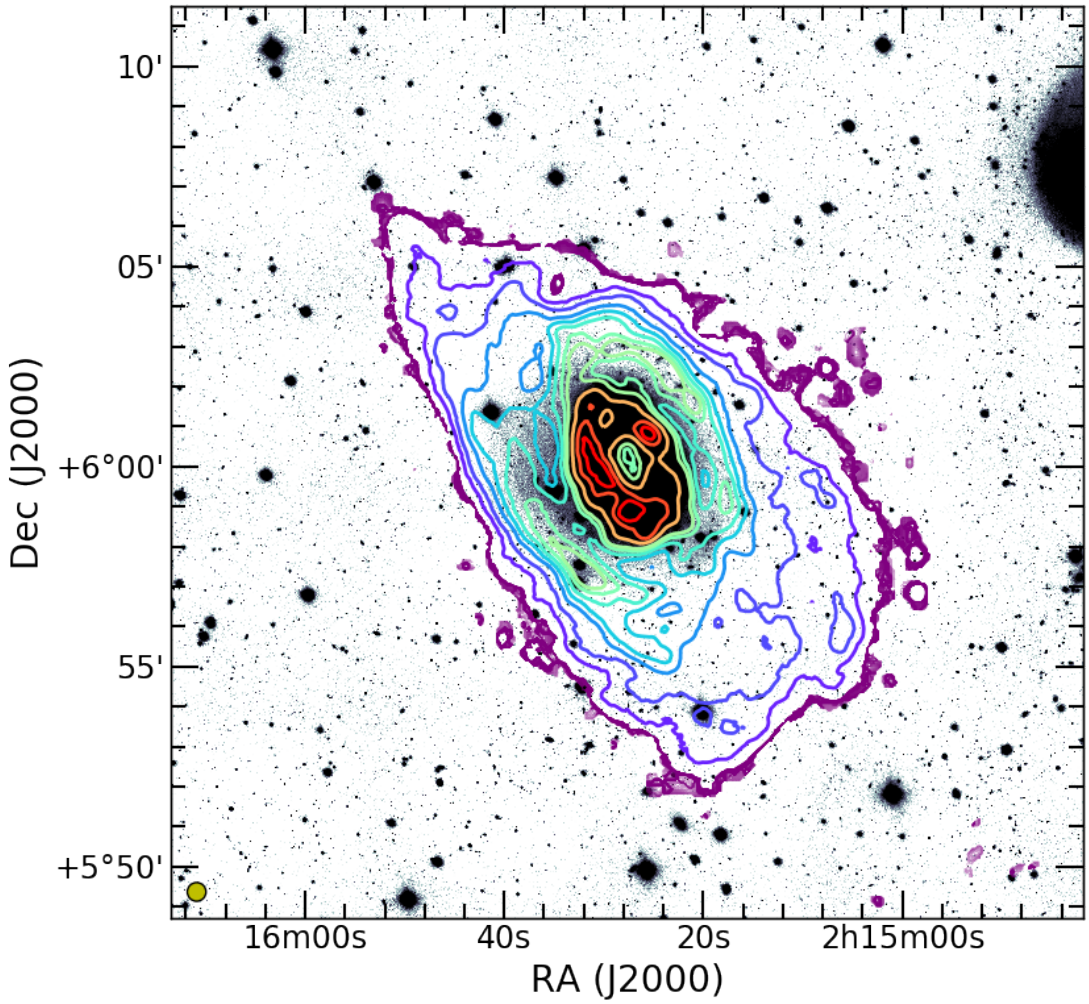

Fig. 4.9 *Background*: VST optical image of CIG 96 ranging from 26 to 28 mag arcsec^{-2}. *Foreground*: HI cube integrated profile contours showing column densities of 0.6, 7.1, 14.1, 28.2, 42.3, 56.5, 70.6, 80.4, 105.8, 127.0 and 141.1 $\times 10^{20}$ cm^{-2}. The yellow circle at the bottom left represents the beam size of 28"×28".

elliptical fittings to the pseudoring structure as well as to the isophotes of the galaxy from 20.2 to 26.4 mag arcsec^{-2} after removing the signatures of the close bright stars to avoid biased fittings.

The fittings of the innermost regions of the galaxy ($\mu_{R\ Cous} = 24.0$ mag arcsec^{-2} or brighter) were not reliable because of the strong influence of the spiral arms. Moreover, bright close stars contaminate the outermost regions (fainter than the same level of $\mu_{R\ Cous} = 24.0$ mag arcsec^{-2}) and even after removing the regions influenced

by these stars, too few points are left as to get reliable fittings out of the isophotes, shown in Fig. 4.10.

However, the optical images showed very clearly the disc center of the galaxy with an error below 1". After fitting the pseudoring we found out that the orientation of the pseudoring was $PA_{pseudoring\ fit} = 21.5°$, similar to the PA of the major axis of the galaxy ($PA_{maj} = 20°$). Moreover, we found a shift of 12" (∼1.2 kpc) between the centers of the pseudoring fitting and the disc, i.e. approximately the radius of the bar. This difference between the disc and pseudoring fitting centers is shown in Fig. 4.11, where the pseudoring fitting has been scaled down to the 23.5 mag arcsec^{-2} (Cousins R) isophote for comparison.

As proposed by Holmberg (1958), disc galaxies can be adequately represented as oblate spheroids so that:

$$cos^2(i) = \frac{(b/a)^2 - q^2}{1 - q^2} \tag{4.3}$$

where b/a is the axes relation and q is the axial ratio for an edge-on system or a parameter dependent on the morphology of the disc (q.v. Fouqué et al., 1990, among others). In the case of CIG 96, the axes relation measured at the 23.5 mag arcsec^{-2} (Cousins R) isophote is $b/a = 0.698821608$, the morphological parameter is $q = 5$ for being an Sc galaxy (see 2.1, Sulentic et al., 2006), so the disc inclination is $i = 46.59°$. We de-projected the optical images assuming this inclination (e.g. Fig. 4.12) to confirm whether the pseudoring might have an oval shape or be in a different plane from the disc. From this image, we calculated the flattening or ellipticity of the pseudoring is of $0.04 - 0.05\%$, i.e. practically circular, suggesting it to be slightly oval if seen at almost the same inclination as the inner disc of the galaxy.

4.2.3 CIG 96 colour index image and optical features

We analyse here the colour index image of CIG 96 and the distribution along the pseudoring (further discussed in Sect. 5.2) via CAHA1.23m photographic B and R images converted to SDSS g and r magnitudes, respectively (see Sect. 3.2.1.2).

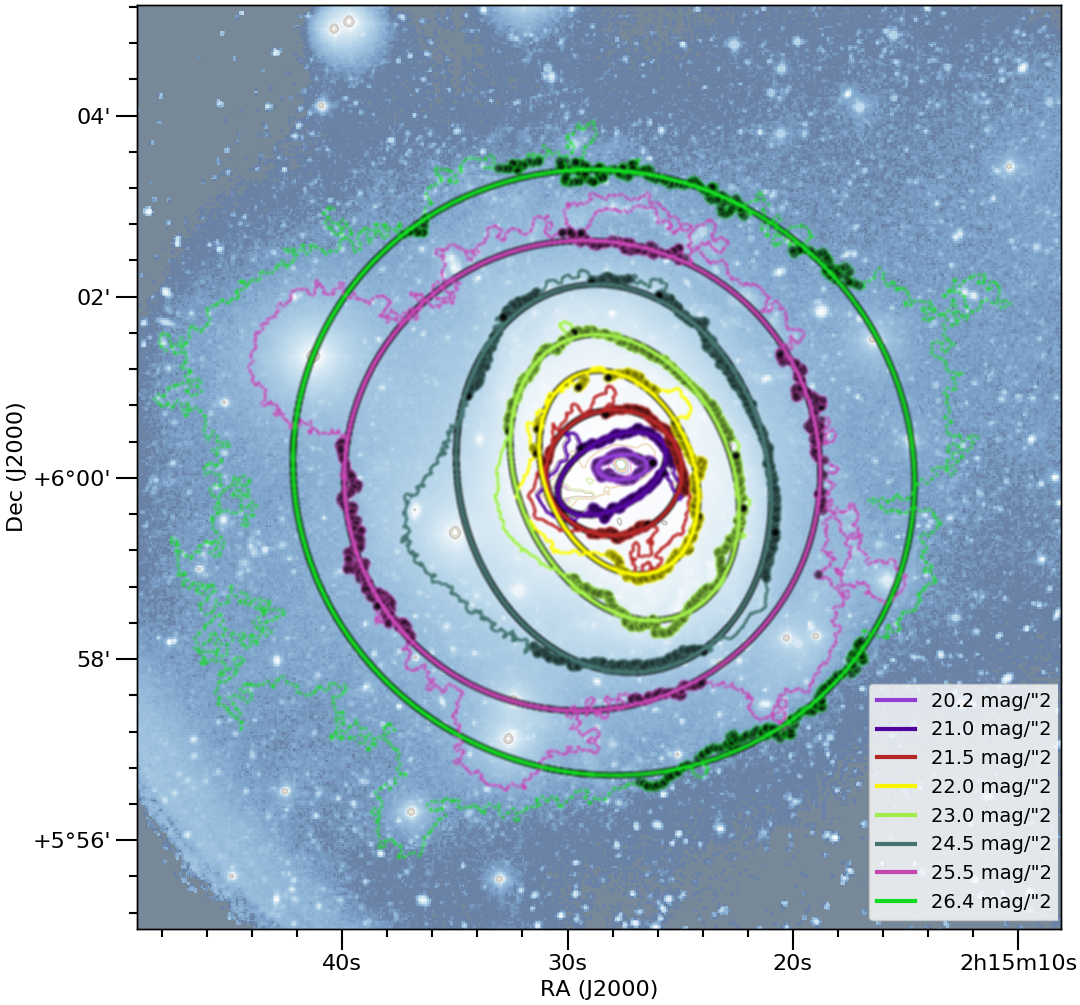

Fig. 4.10 *Background*: CAHA2.2m image of CIG 96 with 19.4, 19.6, 19.8, 20.0, 20.2, 20.6 and 21.0 mag arcsec^{-2} (Cousins R) inner isophotes in pale colours. *Foreground*: elliptical fittings of the 20.2 to 26.4 mag arcsec^{-2} (Cousins R) isophotes of the CAHA2.2m image of CIG 96 from indicated with solid lines. The full isophotes are outlined with faint dotted contours. The elliptical fittings were computed with the darkened points in each isophote, corresponding to those less affected by the close stars.

As a reference for the colour index values plotted in Fig. 4.13 left and central panels, we indicate the boundaries of the Blue and Red clouds from SDSS $g-r$ optical colour−magnitude diagram. In particular we show the Green Valley interval of $(g-r)_{G.V.} = 0.60 - 0.75$ mag as defined by Walker et al. (2013) following the colour analysis by Strateva et al. (2001).

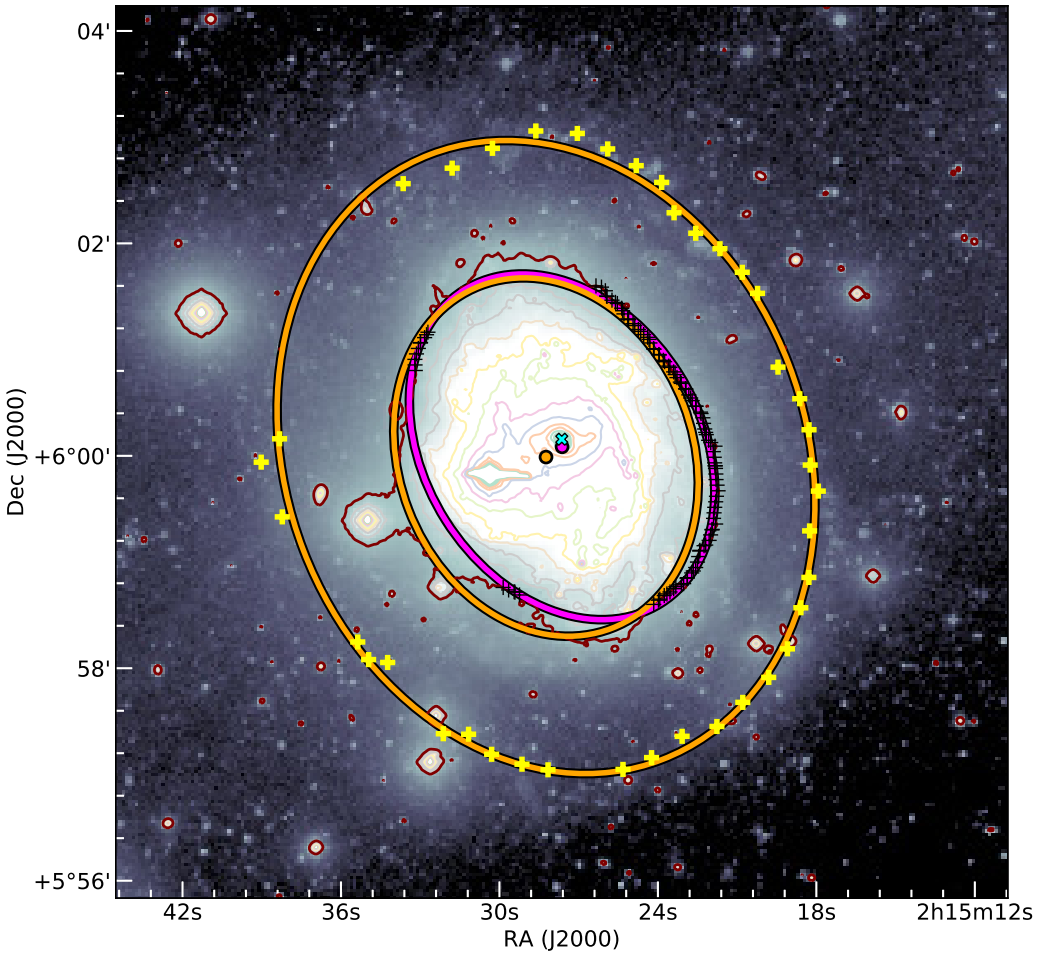

Fig. 4.11 *Background*: CAHA2.2m image of CIG 96 with 19.4, 19.6, 19.8, 20.0, 20.2, 20.6, 21.0, 21.4, 21.8, 22.2, 22.6 and 23.0 mag arcsec^{-2} (Cousins R) isophotes in pale colours. The center of the galaxy is determined with the brightest optical isophotes and marked with a cyan cross. *Foreground*: the most external isophote is 23.5 mag arcsec^{-2} (Cousins R), indicated with a dark red line; the elliptical fitting of this isophote is shown with a magenta solid line (center of the fitting shown as a magenta circle, <1" from the galaxy center) and it has been computed with the regions of the isophote that are marked with black crosses. The elliptical fitting of the pseudoring has been computed with the external yellow crosses. It is shown as the external orange ellipse whose center is shown as an orange circle. For comparison, the pseudoring elliptical fitting has been scaled down (internal orange ellipse) to the same size of the 23.5 mag arcsec^{-2} isophote fitting, keeping the center position. The distance between the centers of the 23.5 mag arcsec^{-2} isophote and pseudoring elliptical fittings is of 12" ($\sim$1.2 kpc).

Qualitatively, we may also remark three striking features from the $g-r$ and optical images (see Fig. 4.13, left and central panels). The first feature is a diffuse arc in the Eastern side of the pseudoring that almost closes it from North to South (Fig. 4.13,

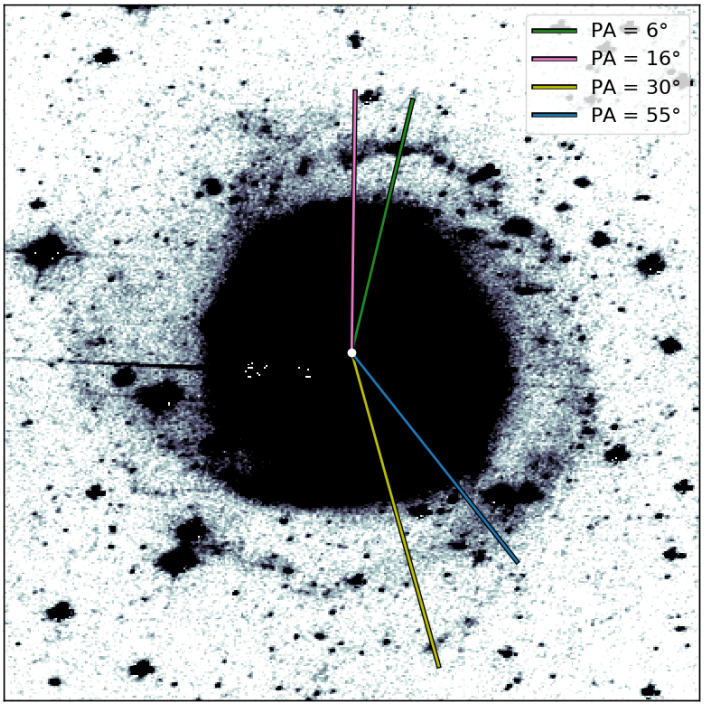

Fig. 4.12 De-projected SDSS g CAHA1.23m image of CIG 96. The pink, blue and green lines indicate the directions (or PA) used to compute the four radial profiles discussed in Sect. 4.2.3.2. They are also shown in the panels of Fig.4.13 where they have been reoriented to preserve the correct PA.

left panel, orange arrow). It is barely detectable (below $\sim 1.2\sigma$) in any individual image further than a diffuse emission due to the heavy contamination of nearby stars. The second structure is also barely detectable (below 1.2σ) in any individual image despite there being no significant contamination by close stars in this region. It is located beyond the Southern region of pseudoring, approximately 30 kpc (∼5') from the galaxy center (Fig. 4.13, left and center panels, cyan arrow). The third structure is indicated with yellow crosses in the central panel of Fig. 4.13. This double structure has a surface brightness of ∼26.0 mag arcsec^{-2}seems to connect the Northern and Southern inner parts of the galaxy with the Western and Eastern sides of the pseudoring, respectively.

4.2.3.1 Pseudoring colour index distribution

We have studied the azimuthal variation of the colour index along the pseudoring by determining its median value in 33 circular non-overlapped apertures distributed in

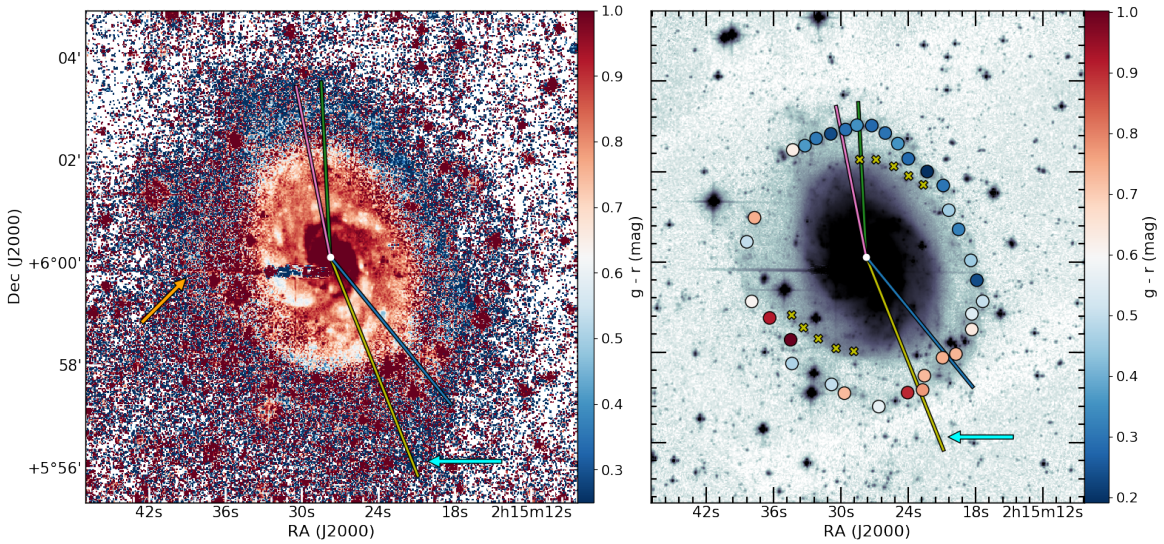

Fig. 4.13 *Left panel*: SDSS $g-r$ colour index image smoothed with a Gaussian kernel of 1 pixels radius. Orange arrow points to the Eastern and more diffuse arc of the pseudoring. Cyan arrow points to an optical feature to the South. Blue and red tones indicate colour index in magnitudes. The pink, blue and green lines indicate the directions (or PA) used to compute the four radial profiles discussed in Sect. 4.2.3.2 and indicated in Fig. 4.12. *Right panel*: 33 circular apertures of 1.25 kpc radius (12.7") located over stars-free areas of the pseudoring, represented over the CAHA2.2m and CAHA1.23m combined optical image. A bluer/redder region indicates a bluer/redder $g-r$ colour index. The cyan arrow points again to the Southern feature. Yellow crosses indicate the connecting regions between the pseudoring and the inner parts of the galaxy.

foreground star-free regions along its extent as shown in central panel of Fig. 4.13, except for the Northeastern region (PA between $38°-70°$) due to the lack of reliable optical emission in this arc. We defined the apertures over a de-projected image of CIG 96. For a better visualisation, we have kept their spatial location and circular shape in the image presented in the previous figure, which is not de-projected. In order to discard any colour index changes in the pseudoring due to a gradient in the sky level, we determined the sky colour index of 62 regions set farther than the pseudoring, covering 360°around CIG 96 and free of bright stars. These apertures show $g-r$ values between ∼0.2 and ∼1.2. In Fig. 4.14 we show the $g-r$ colour index distribution of all regions according to their PA and we find no colour index correlation between the apertures from the pseudoring and those from sky.

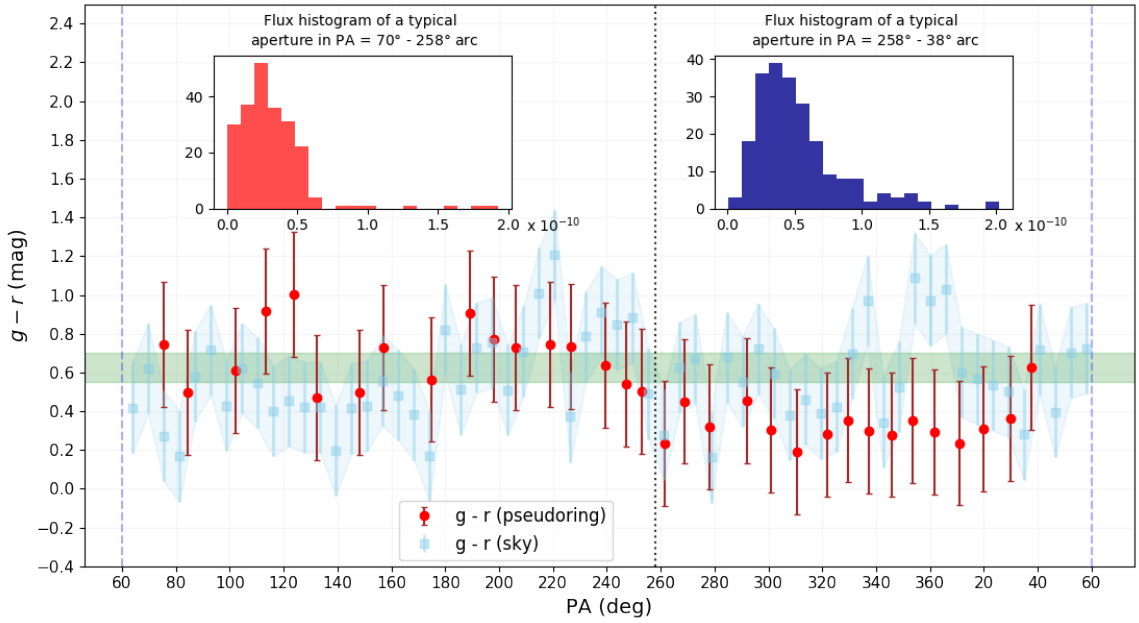

Fig. 4.14 SDSS $g-r$ colour index vs. PA along the pseudoring. The red dots represent the $g-r$ values obtained from the SDSS g and r de-projected images. They are obtained from dividing g median flux to the corresponding r median flux of each aperture and converting these results to magnitudes. The pale blue dots correspond to the $g-r$ colour index measured at a distance of $r=29.5$ kpc ($\sim$5') on the sky. The green stripe sets the Green Valley interval that separates the red cloud ($g-r>0.75$ mag) from the blue cloud ($g-r<0.60$ mag) as defined in 4.2.3. The embedded figures correspond to typical flux $\times 10^{-10}$ histograms for two apertures from the Southeastern region (PA $=70°-258°$ and the Northwestern region (PA $=258°-38°$) separated by the vertical doted grey line.

However, as anticipated in the central panel of Fig. 4.13, we find a colour index change in between two PA ranges of the pseudoring. The 17 apertures of the Southeastern arc (within PA $=70°-258°$) show a median colour of $g-r=0.73$ mag ($st.dev.=0.15$ mag), i.e., a redder colour. Contrarily, the remaining 16 apertures of the Northwestern arc (within PA $=258°-38°$) show a median value of $g-r=0.31$ mag ($st.dev.=0.11$ mag), i.e., a bluer colour, making the difference between the two regions of $g-r\simeq 0.4$ mag.

4.2.3.2 Radial cuts

In order to compare the colour of the disc with the immediate pseudoring regions we computed radial profiles from individual g and r images. Fig. 4.12 shows the de-projected SDSS g image of CIG 96 together with the lines along which those were calculated.

These profiles are shown in Fig. 4.15, where the bulge (the first 2.5 kpc, E11a), disc and pseudoring radii are marked as well. We selected the orientations due to the different structures crossed: disc, dust regions, arms, star forming regions and thicker/thinner regions of the pseudoring. The profiles were then computed at PA of 6°, 16°, 30°and 55°and we will refer to them as PA6, PA16, PA30 and PA55, respectively.

To present the main results that these profiles yield, we have used a surface brightness of 26.8 mag arcsec^{-2} in the SDSS r band. At this depth, the disc size varies in a range of $R_{disc} = 9.5 - 11$ kpc, depending on the PA.

The gap between the disc and pseudoring is not constant either: in the regions where the pseudoring and the disc are well resolved, the gap has an approximate width of $\simeq 1$ kpc. However, in regions where both the disc and pseudoring have a more diffuse emission, they prevent any reliable estimation of this separation.

The gap width, as well as its uncertainty, has a connection to the pseudoring dimensions: the more defined regions of the pseudoring have a width of $w_{pseudoring} \simeq 2$ kpc but it may rise up to $\sim$4 kpc in some diffuse regions being hardly distinguishable from the disc.

Profile PA6 (green) shows red colours along the disc relative to the limit defined by the Green Valley strip. The peak at $\sim$7 kpc corresponds to a foreground star ($m_{r\ SDSS} = 19.65 mag$). The pseudoring shows blue colours in most of its extent along this PA, accordingly to the star forming region (radius $\sim$0.7 kpc) that dominates this section of the cut, centered at a radius of approximately 12.5 kpc. The colour difference of the disc and the pseudoring at this PA is $\sim$0.4 mag.

Profile PA16 (pink) also shows the difference in colours between the disc and the pseudoring. The disc shows a stable red colour throughout its whole extension ($g - r \simeq 0.7$ mag). However, the pseudoring shows a colour gradient from $g - r \sim 0.7$

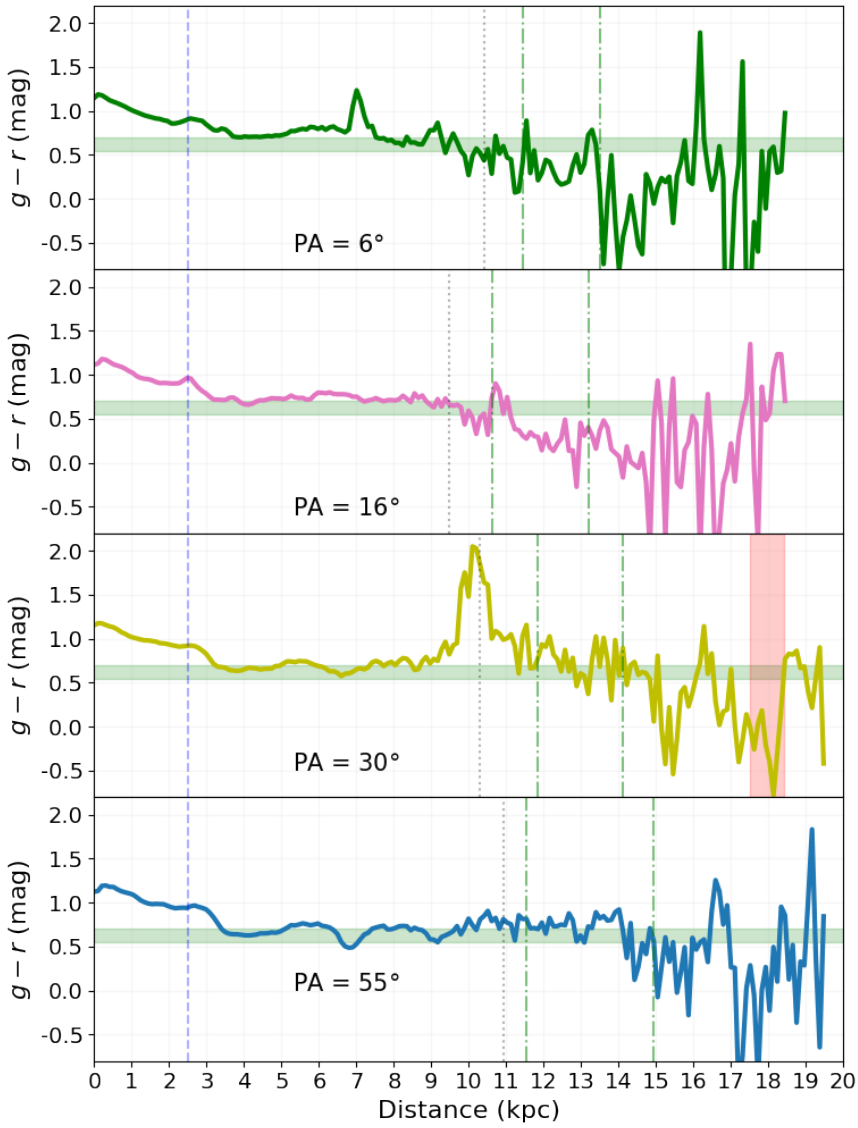

Fig. 4.15 Radial profiles obtained along four different orientations with PA of 6°, 16°, 30° and 55° (shown in Fig. 4.13, right panel) at the top, top-center, bottom-center and bottom panels, respectively. The horizontal green stripe represents the Green Valley in SDSS $g-r$ (see Sect. 4.2.3. The bulge, disc and pseudoring limits are measured at 26.8 mag arcsec^{-2}. The bulge limit (2.5 kpc) and the disc limit are shown as the light blue dashed and black dotted lines, respectively. The pseudoring variable inner and outer limits are defined in each panel by the green dot-dashed lines. The light red band in the PA = 30°panel sets the location of the optical feature to the South marked as a cyan arrow in the left panel of Fig. 4.13 and a magenta ellipse in Fig. 4.17.

to 0.1 approximately, hence most of the pseudoring has blue colours. This profile was also aimed towards a large star forming region of ∼1.5 kpc radius in the pseudoring

and located at an approximate distance of 12 kpc, so such a blue colour is expected. However, there is no apparent cause for the colour change.

Profile PA30 (yellow) shows an uniform disc colour within or right on the red edge of the Green Valley ($g - r \simeq 0.75$ mag) consistent with the rest of the profiles. There is an exceptionally red peak at 10.5 kpc that, unlike in the case of PA6 (produced by a star), it is the result of a region with large quantities of dust. The orientation of the previous profiles missed these dusty inner regions of the galaxy, easily visible in the colour index image from Fig. 4.13, left. PA30 crosses the pseudoring through an area of diffuse emission and the redder colour is consistent throughout its extension. The orientation of this profile was chosen to obtain also the colour of the Southern feature of ∼1 kpc width located at ∼18 kpc indicated with a red vertical stripe (also marked with a cyan arrow in Fig. 4.13, left). Despite the fact that the feature is surrounded by the sky, its location and the surrounding 0.5 kpc show a clearly blue colour.

Profile PA55 (blue) shows a different behaviour along the disc. The mean colours are bluer than along the previous profiles; two regions that correspond to where the arms are crossed show very blue colours. This profile was selected to observe a much more diffuse and broad region of the pseudoring (width of 3.5 kpc). As in the disc, the pseudoring colour along this orientation is not homogeneous but it shows red colours ($g - r \sim 0.8$ mag) throughout most of its width. The farthest part of the pseudoring shows a steep change towards bluer colours, making it hard to confirm whether it is an artifact of the sky or an existing structure with similar colour.

4.2.4 Colour index and HI column density in the pseudoring

The black crosses of Fig. 4.16 show the location of the apertures of the pseudoring on top of the HI 0^{th} moment map. We find a remarkable spatial correlation between the optical pseudoring and the HI distribution, in agreement with E11a. In Fig. 4.16 we indicate with a magenta ellipse the spatial location of the optical Southern feature (shown in Fig. 4.13 left panel with a cyan arrow). It is too distant to the pseudoring (∼4.1 kpc) as to confirm that both have a physical link and, unlike other SF regions of the pseudoring, we find no increase of the N_{HI} in this region.

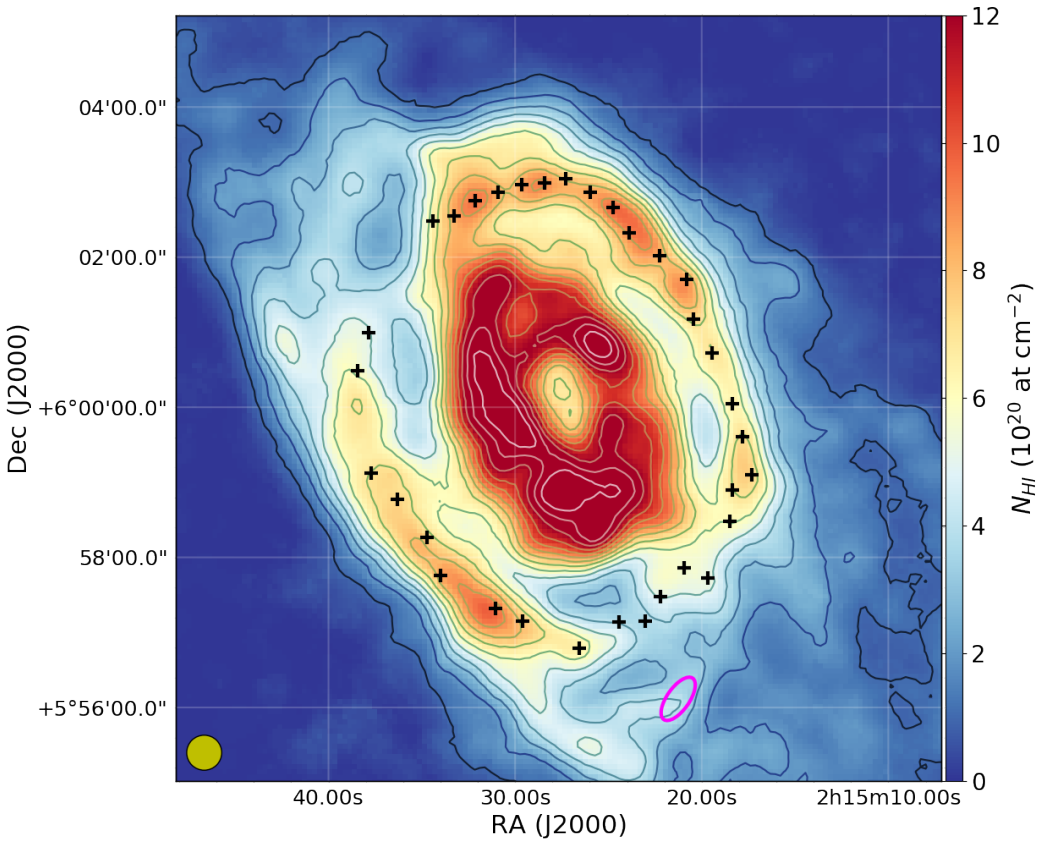

Fig. 4.16 Central 53×53 kpc (9×9') of the integrated HI emission map of CIG 96. Column density is indicated in colour gradient. Contours indicate 1, 2, 3, 4, 5, 6, 7, 8, 9, 10, 11, 12, 13 and 14×10^{20} cm^{-2}. The black crosses indicate the central position of the 33 apertures used to measure the colours of the pseudoring (see Sect. 4.2.3.1). The magenta ellipse indicates the position of the Southern feature indicated with a cyan arrow in Fig. 4.13, left panel, the $g-r$ colour index image. The yellow circle at the bottom left indicates the HI image synthesised beam of $28'' \times 28''$.

We have performed a detailed comparison between the pseudoring colour index $g-r$ and N_{HI} for each selected aperture. With this aim, we have scaled each one of them by subtracting the mean value of the 33 apertures and dividing them by their sigma value (Fig. 4.17, top panel).

We observe an anticorrelation between $g-r$ and N_{HI} scaled values within PA = 180° − 40°, i.e. bluer colours correspond to larger column densities. It is only broken between PA = 90° − 180°, approximately, probably due to less reliable $g-r$ measurements in this side of the pseudoring, the most diffuse region. The anticorrelation is also confirmed in the bottom panel of Fig. 4.17 where we show $g-r$ as a function of

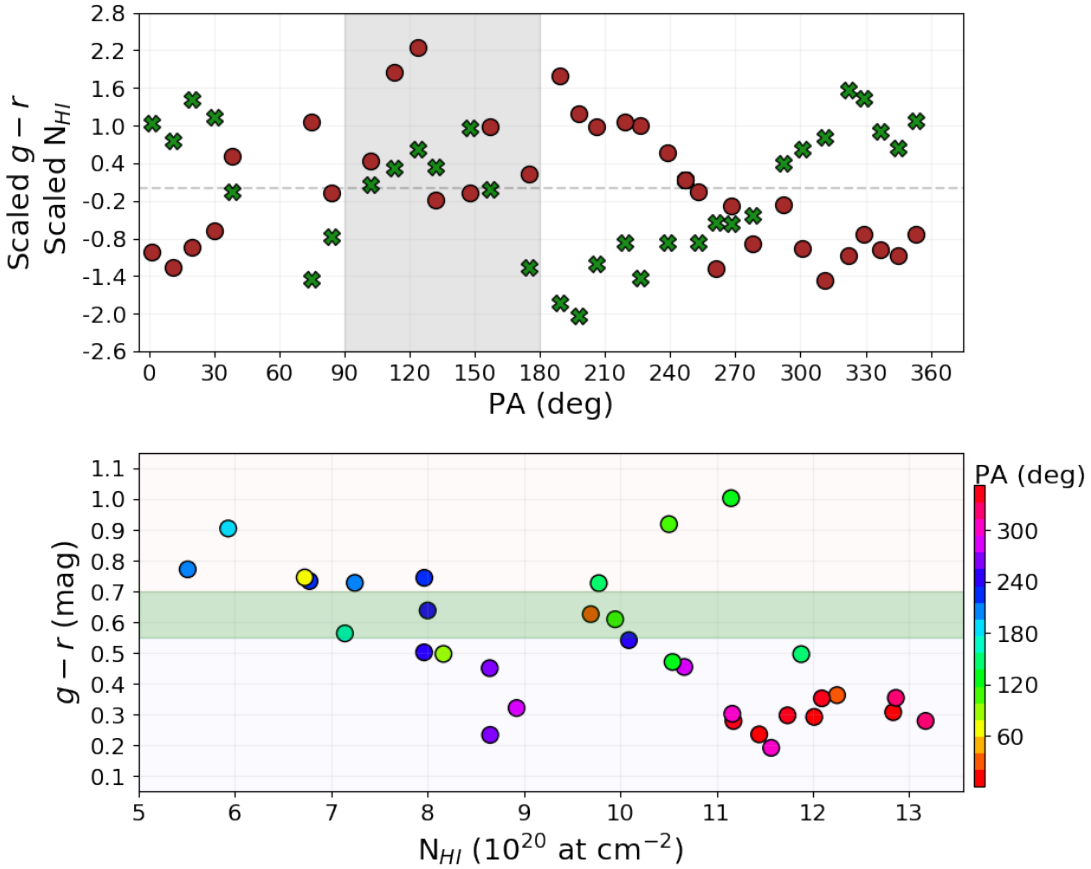

Fig. 4.17 *Top panel*: $g-r$ (brown circles) and N_{HI} (green crosses) scaled (mean subtracted, sigma divided) values in each of the 33 apertures. A grey dashed line has been drawn at $g-r=0$ for reference. Redder colours and higher N_{HI} are positive in this figure. *Bottom panel*: $g-r$ median colour index vs. N_{HI} measured in the 33 apertures traced over the pseudoring. The green horizontal stripe represents the Green Valley in SDSS $g-r$.

N_{HI}: most of the bluer areas, mainly located in the Northwestern side of the pseudoring (PA $= 260° - 40°$) show column densities of $8.5 - 13.5 \times 10^{20}$ cm^{-2}, higher than most of the redder ones which show much lower levels instead. These results are discussed further in Sect. 5.2.

4.2.5 Optical connection with the companion

We aimed to observe any possible optical structures connecting CIG 96 and its companion (see Sect. 4.1.4). It is only possible to studying any potential connection with the

VST 1°×1°image as this provides continuous coverage across the ∼90 kpc separation CIG 96 from its companion, having the CAHA images have a much smaller field of view of 12'×12'. Fig. 4.18 shows a 10'×10' image centered between the two galaxies. At the current optical surface brightness limit, coinciding with the HI map, we find no signs of any stellar feature tracing any current or past link interaction between CIG 96 and the companion.

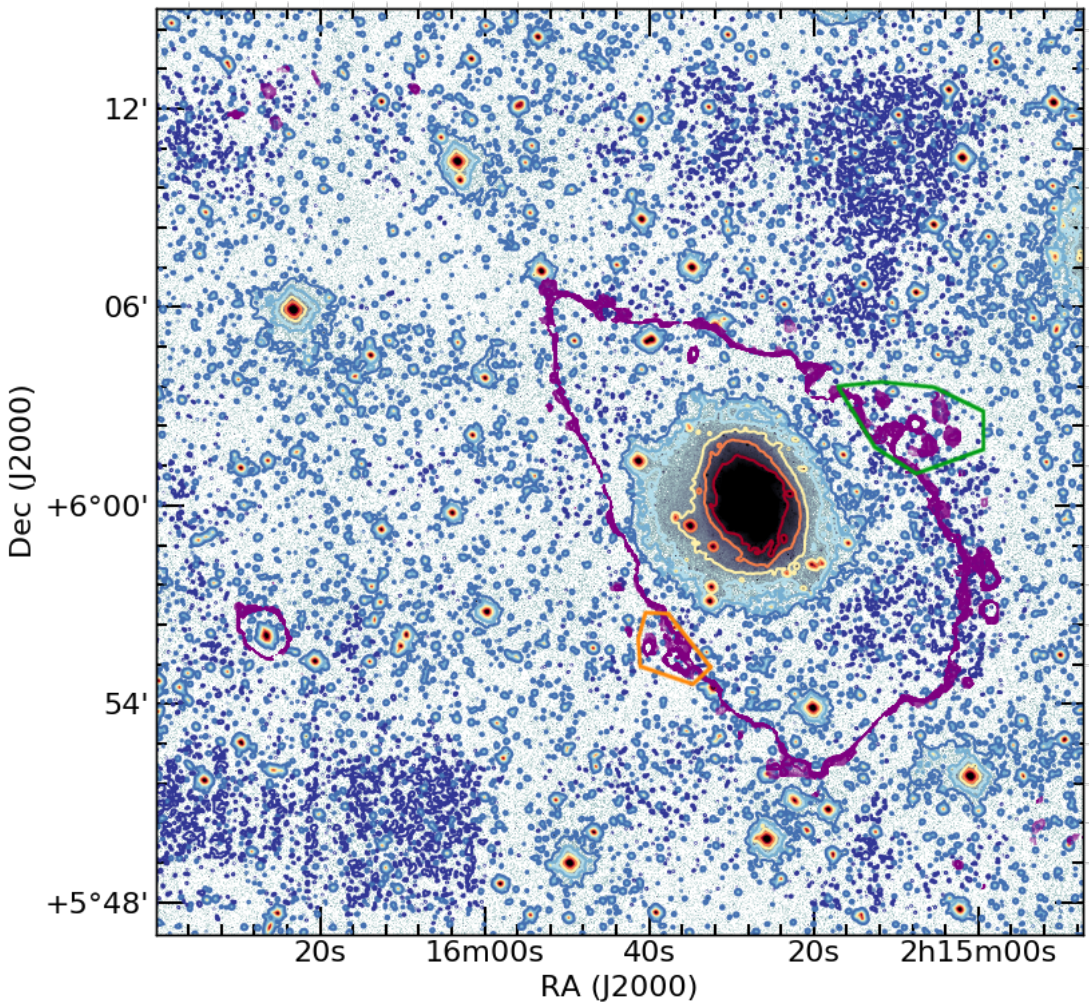

Fig. 4.18 VST image in SDSS r band of a 28′ × 28′ region covering both CIG 96 and the companion NGC 864 COM1 (indicated by the magenta contour to the East of the image). Optical contours are set in 24.0, 25.0, 26.0, 27.0, 27.5, 28.0 and 28.4 mag arcsec^{-2} (SDSS r), smoothed with a Gaussian kernel of 11 pix radius. The purple contour marks the HI column density limit of the 0^{th} moment at $0.6\times10^{20}\,cm^{-2}$, the same as in Fig. 4.9. The green and orange regions mark the position of the NW and SE HI features, respectively.

4.2.6 Cirrus

A precise sky subtraction is key to reach faint surface brightness levels despite the possible large PSFs from close stars (whose radii reach several arcmin, Trujillo and Fliri 2016) may hide faint stellar structures. However, there is another limiting factor at the current optical surface brightness: the emission due to the presence of Galactic cold dust (Sandage 1976, confirmed with IRAS data by Neugebauer et al. 1984) known as cirrus of the Milky Way. These cirrus may cover large areas in the sky and, depending on the region, they may start to be especially relevant from $\mu_{r\ SDSS} \simeq 25.5 - 26.0\,\mathrm{mag\,arcsec^{-2}}$ in the optical wavelengths (Duc et al., 2015).

As described in Sect. 3.3, we have used Planck857 and WISE3 images to identify the presence of cirrus in the field of CIG 96. Their optical resolutions are 4.2' and 6.5", respectively, i.e. approximately 242 and 6 times lower than the $1.04"\,\mathrm{pix^{-1}}$ resolution of our CAHA images or 1260 and 30 times lower than our VST image, respectively.

The Planck857 image is a good indicator of cirrus; however, we cannot extract reliable conclusions in the field of CIG 96 due to its low spatial resolution. We used the central $40' \times 40'$ of the VST image to inspect the cirrus (see Fig. 4.19, top left panel). It shows that this area is populated with scattered emission visible from $\sim$28.5 mag arcsec^{-2}. While this image is not enough to conclude whether that emission belongs to cirrus or not, we may confirm it does not show up in any other observation considered in this work.

In the Planck857 image (Fig. 4.19, bottom left panel), a $\sim 2\sigma$ peak of emission (where σ is the rms measured on the clean Southeastern region) is visible in the central pixels where the galaxy is located. In the surrounding area and close to the noise level, there are extended areas to the East, North-West and South-West of CIG 96 which seem to match some of the emission observed with the VST image at $28.5\,\mathrm{mag\,arcsec^{-2}}$.

The lack of cirrus structures brighter than $28.5\,\mathrm{mag\,arcsec^{-2}}$ suggests they provide scarce (if any) contamination at brighter levels in our VST image, hence we set our detection limit at $28.4\,\mathrm{mag\,arcsec^{-2}}$ in SDSS r band. From the opposite point of view, the low resolution of Planck857 makes it pointless to use such image to find any cirrus structure in our optical image (Fig. 4.19, bottom right panel). Should these exist, a positive matching between our VST and Planck 857 images would require extremely

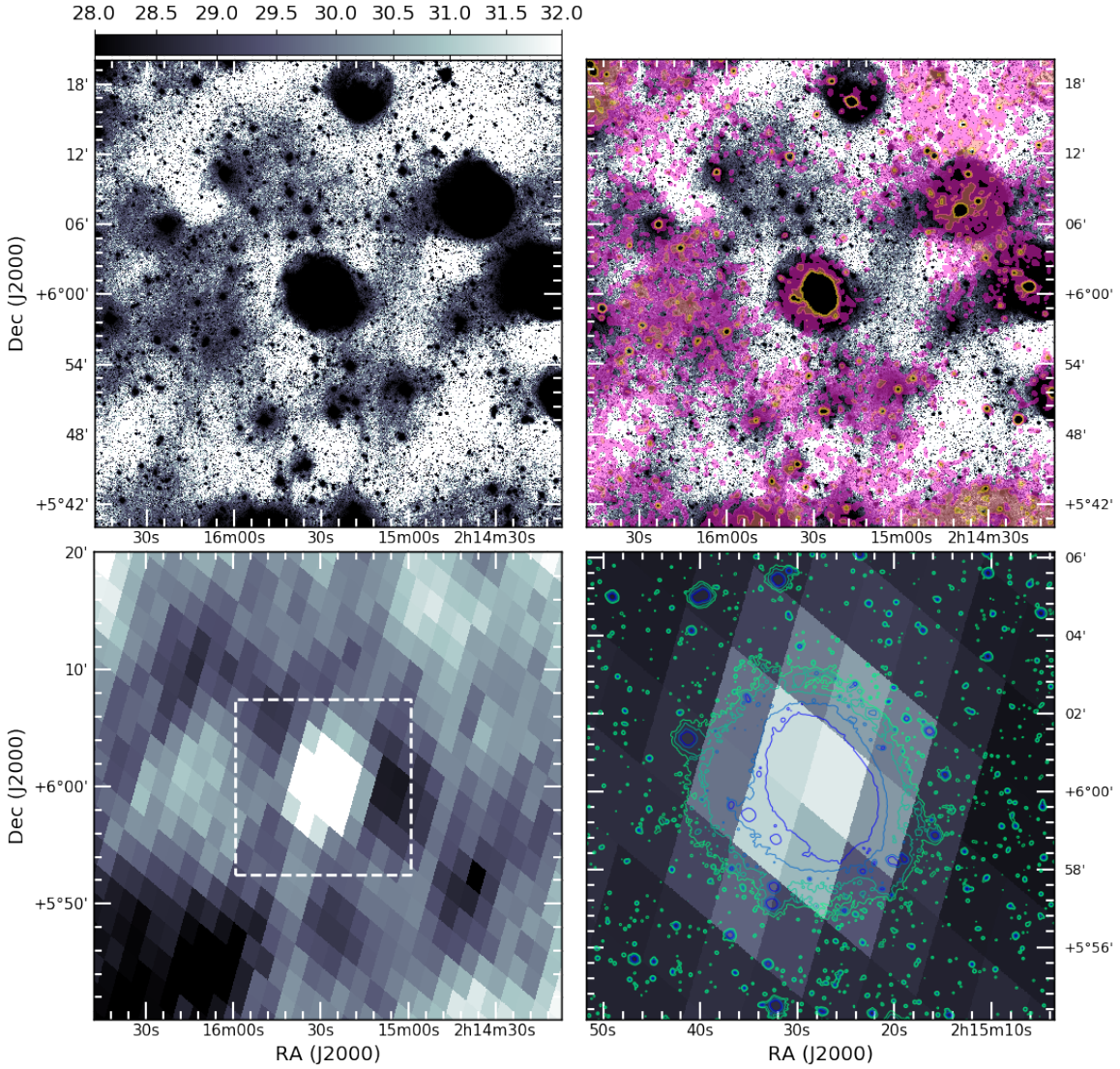

Fig. 4.19 *Top left panel*: central $40' \times 40'$ of the VST optical image in SDSS r band of CIG 96. The surface brightness is indicated on top of the figure in mag arcsec^{-2} (SDSS r band) favouring the levels that enhance the Galactic cirrus located in the field of our galaxy, which show up from $\mu_{r\ SDSS} \simeq 28.5$ mag arcsec^{-2}. *Top right panel*: background, the same $40' \times 40'$ VST optical image as in top left panel; foreground, overlay of WISE band 3 (12 μm) smoothed image contours (Gaussian kernel of 21 pixel radius). *Bottom left panel*: $40' \times 40'$ Planck 857 GHz image of CIG 96. The dashed white square indicates the approximate area selected for the bottom images. *Bottom right panel*: background, $12' \times 12'$ Planck 857 GHz image; foreground, 25.0, 26.0, 27.0, 27.5 mag arcsec^{-2} smoothed (Gaussian kernel of 7 pixel radius) optical contours from VST image (SDSS r band).

large and bright structures, easily detectable in both images; however, we do not find such large structures, preventing the use of the Planck857 image in this case.

WISE3 emission is shown in Fig. 4.19, top right panel, over the optical VST image. A quick glance at both Planck857 and WISE3 emission shows there is good correspondence between them, as expected. However, this is not the case for the optical−infrared images. Despite its higher resolution, the WISE3 image only matches some areas from the optical image, showing no significant emission nearby CIG 96.

In summary, Planck857 and WISE3 images show no signs of large, diffuse and faint structures over CIG 96 that might be interfering with our optical detection limits. However, we cannot confirm a full correspondence between any of the infrared images and the diffuse optical emission. Consequently, these diffuse structures must be considered as an unavoidable limit of the surface brightness of our VST image, raising it to 28.4 mag arcsec^{-2}.

Chapter 5

Discussion

In this section we discuss the implications of the close environment of CIG 96, the pseudoring main properties like colour, age and possible origins, as well as the different HI features detected.

5.1 The environment of CIG 96: companions and implications on the isolation

As introduced in 2.1.1, all galaxies have their first neighbours within a certain distance from a particular galaxy and have a certain level of interaction or dynamical forces between them. Taking into account the number of companions and the tidal force magnitude, the level of isolation of the host can be defined. The two parameters that we use to quantify the isolation degree of a galaxy from CIG, such as CIG 96, are the local number density, η_k, that accounts for the number neighbour galaxies within a radius of 0.5 or 1 Mpc (depending on the criteria selected), and the tidal force estimation, Q, that quantifies how much the host is affected by its neighbourhood.

According to the NASA/IPAC Extragalactic Database (NED), CIG 96 has 5 identified galaxies within a radius of 1 Mpc: NGC 864 COM01 (the aforementioned companion), HIPASS J0217+06, UGC 01677, UGC 01670 and UGC 01803.

NGC 864 COM01 is the closest and brightest neighbour (see Sect. 4.2.5), located to the East. The companion and HIPASS J0217+06 have similar sizes and both are at least 5 mag (m_B) fainter than CIG 96. The latter is located to the North-East and it is only visible close to the limit of our VST image, where the region is heavily contaminated by a close star. UGC 01677 and UGC 01670 are located to the North-West of CIG 96, beyond the limits of all available images and last, UGC 01803 is an edge−on galaxy located to the North-East. The properties of these neighbours are summarised in Table 5.1.

Table 5.1 Companions of CIG 96 within 1 Mpc [a]

Name	m_B [b]	D_{maj} [c]	PD [d]	V_{cen} [e]
NGC 864 COM01	16.38	0.6 / 3.3	15.24 [f] / 90 [f] / E	1578 [f]
HIPASS J0217+06	16.50	1.6 / 9.4	40.03 / 235 / NE	1549
UGC 01677	18.00	0.9 / 5.3	76.70 / 450 / NW	1575
UGC 01670	14.80	2.2 / 13.0	83.73 / 495 / NW	1593
UGC 01803	14.70	2.8 / 16.5	89.26 / 527 / NE	1615

Notes.
[a] Data from the NASA/IPAC Extragalactic Database (NED) unless stated otherwise.
[b] Apparent B magnitude.
[c] Diameter in arcmin / kpc.
[d] Projected distance in arcmin / kpc / direction of the galaxy.
[e] Central velocity in km s^{-1}, LSRK.
[f] This work.

As explained in Sect. 2.1.1, we used the methods from the two works of Verley et al. (2007c) (V07) and Argudo-Fernández et al. (2013) (A13) to calculate the isolation parameters of CIG 96.

V07 consider the first $k-$th similar sized neighbours within a 500 kpc radius. In the case of CIG 96 only the closest two neighbours, i.e. NGC 864 COM01, HIPASS J0217+06 are selected and the isolation parameters are $\eta_k^{V07} = 0.877$ and $Q_{0.5}^{V07} = -1.981$. A13 extend the radius up to 1 Mpc, i.e. they consider the 5 neighbours mentioned above, and calculate the isolation parameters with photometric and spectroscopic data. The Q parameter of CIG 96 can not be calculated with the photometric data because they contain no neighbour that violates the necessary criteria to measure the Q between them and the host. However, the spectroscopic data allow to obtain

the isolation parameters for CIG 96 being $\eta_k^{A13} = 0.68$ and $Q^{A13} = -3.41$, the same calculate. This method is also used by Argudo-Fernández et al. (2014), where they focus on identifying the satellites around host galaxies from CIG, distinguish them from the Large Scale Structure (LSS) and quantify their effect over the host galaxy.

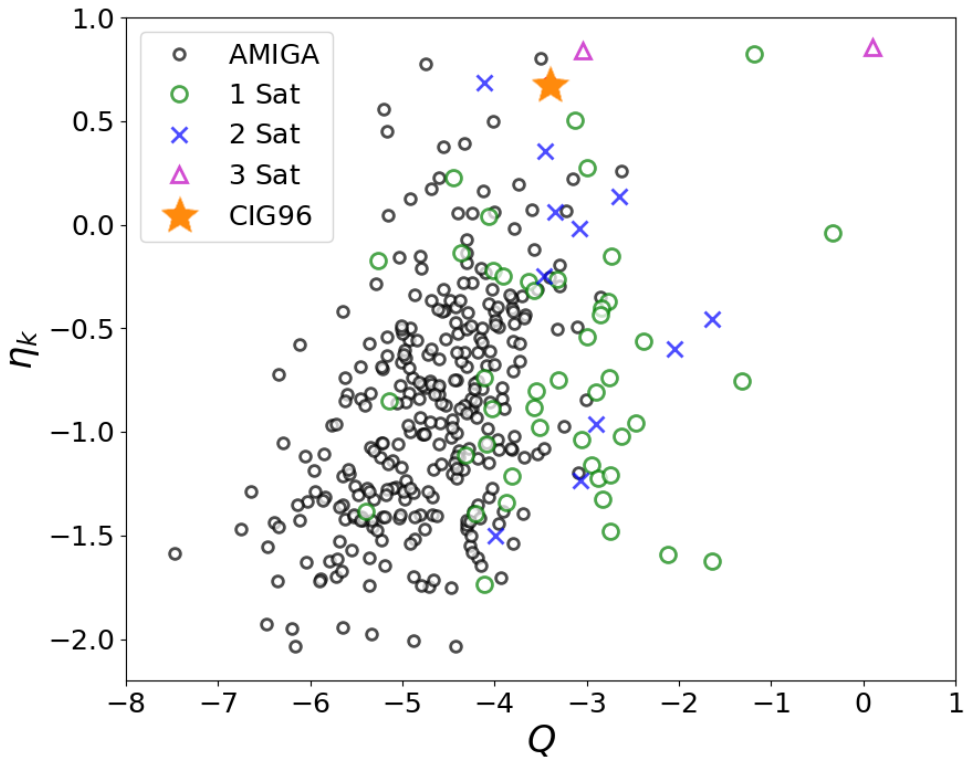

Fig. 5.1 Representation in the isolation parameters of the subsample generated with spectroscopic data of CIG galaxies as calculated by Argudo-Fernández et al. (2014) (q.v. Fig. 8 of that work). Lower values of local number density η_k and tidal force estimation Q represent higher isolation. CIG 96 position is highlighted.

According to the spectroscopic data of A13, the position of CIG 96 is highlighted in Fig. 5.1 where lower values of η_k and Q represent higher isolation. The rest of galaxies shown for comparison corresponds to the subsample of galaxies used in Argudo-Fernández et al. (2014) with 0, 1, 2 or 3 dynamically linked satellites (physically bound neighbours, q.v. Fig. 5 in that work). The 5 closest companions of CIG 96 within 1 Mpc are responsible for raising the η_k parameter, whereas the Q value is similar to galaxies with 1 or 2 satellites. However, CIG 96 has no satellite around it. This

apparent contradiction reinforces a very relevant point: the isolation parameters are meant for statistical interpretations rather than to understand the environment of a particular galaxy. The physical interpretation of these parameters is that the populated environment of CIG 96 does not contain massive galaxies and, among all the neighbours, the closest companion included, none are affecting the evolution of CIG 96, as supported by all our observations.

5.1.1 Isolation time estimation

As defined by Verdes-Montenegro et al. (2005) and in agreement with the isolation criteria, the isolation time estimates the minimum time a galaxy has been free of interactions with major companions. It is defined as follows: let D be the diameter of CIG 96, the time that a hypothetical companion of $d = 4 \times D$ size needs to cover a distance of $20 \times d$ by travelling at a typical 'field' velocity of $150\,\mathrm{km\,s^{-1}}$ is $\sim$11.5 Gyr, i.e. almost the age of the Universe, implying no recent interaction.

The isolation time of CIG 96 with respect to each of the previous neighbours yields different results. When taking the closest companion, NGC 864 COM01, travelling at a relative velocity of $33\,\mathrm{km\,s^{-1}}$ with respect to CIG 96, the isolation time of CIG 96 results in $\sim$2.7 Gyr. The rest of the targets, located farther away, yield isolation times of $\sim$11 Gyr or higher than the age of the Universe, i.e. they could not have interacted with CIG 96 in the past.

5.1.2 Connection between CIG 96 and the companion and limitation by cirrus

Despite the depth reached with our HI cube and optical images, we detect no signs of gaseous or stellar features between CIG 96 and the gas−rich companion (see Sect. 4.1.4 and 4.1.1) nor any other more distant galaxies. The lack of detection supports the hypothesis of a long-lived isolation of CIG 96 where its asymmetrical HI distribution (see Fig. 4.4) may come from internal processes rather than an external agent with the exception of an absorbed small companion. HI asymmetries caused by major mergers interactions are detectable within 0.4−0.7 Gyr (Holwerda et al., 2011c), i.e.

approximately within one or two full rotations of CIG 96 ($T_{rot}^{CIG\,96} \simeq 0.4$ Gyr). However, the high isolation of the galaxy rules out encounters with major companions for, at least, the last ∼2.7 Gyr.

The Galactic cirrus are observed from a level of 28.5 mag arcsec^{-2} (SDSS r) to fainter surface brightness, affecting a remarkable area of the field around CIG 96. Infrared images may play a relevant role for the cirrus identification and future removal, hence allowing reaching lower limits in surface brightness. In this case, the two Planck857 and WISE3 images discussed do not manage to fully trace these structures at the sensitivity and spatial resolution required to remove them from the optical images. Since cirrus cannot be avoided by introducing any changes in the observational and data treatment strategy, they set an observational limit to our optical images, hampering the detection of fainter structures in polluted areas.

5.2 Origins of the features of CIG 96

The structures observed in CIG 96 do not show an unique or evident origin. The isolation level of the galaxy guarantees no encounters with major companions, suggesting that either minor events or internal secular evolutionary processes could be behind these features. Next, we discuss the different possibilities.

5.2.1 HI features

For decades it is known that the HI in spiral galaxies frequently shows asymmetries and lopsidedness (Baldwin et al., 1980; Richter and Sancisi, 1994). However, the origin of such features in the isolated galaxies from CIG is unknown. The asymmetries of CIG 96 represent an excellent use case that have motivated all the observations and discussion of this work.

As described in Sect. 4.1.2 and 4.1.3 and shown in Figs. 4.2, 4.4 and 4.7, we observe two external HI clouds, the NW and SE HI features, that do not seem to belong to the main HI body of CIG 96; also, there is a region with a remarkable receding velocity in the outermost Southwestern region. The NW HI feature is a

clumpy, almost continuous cloud spread throughout $\sim$70 km s^{-1} and connected to the galaxy approximately along the direction of its minor axis. This connection may be traced down to channels 24 and 25 (1560 and 1570 km s^{-1}, respectively), where the HI cloud and the galaxy join showing no perturbation in the velocity field. The SE HI feature consists of a few gaseous clouds located in the same spatial location and spread along $\sim$40 km s^{-1}. However, the lack of any noticeable perturbation over the outermost HI of CIG 96 suggest this feature has had little (if any) effect on the Eastern side of the galaxy.

It is also important to remark that none of these two features show any optical counterpart down to our detection limits.

The most distant HI region located at about $\sim$7' ($\sim$41 kpc) from the center along the direction of the major axis, indicated with a cyan arrow in Fig. 4.7) shows a receding velocity that is $\sim 30 - 40$ km s^{-1} above the expected $\sim$1430 km s^{-1} of this region. E05 proposed this region as a possible kinematically detached clump from the galaxy. The 0^{th} moment of our HI cube (Fig. 4.4) and the P/V cuts over the major axis show such kinematical detachment as well as small and scattered unresolved HI clouds. However, they do not provide evidence of a physical detachment in the Southwestern region (indicated with the cyan arrow in Fig. 4.7, top panel), which is larger than any of the small HI cloud nearby. The inspection of the 1^{st} moment map suggests the farthest Southern region might be warped but this would imply an external agent like a minor merger or the accretion of gas (Bournaud et al., 2005; Jog and Combes, 2009) that we do not find at our column density limit of $N_{HI} = 8.9 \times 10^{18}$ cm^{-2}. For this reason, we cannot rule out the cold gas accretion below the already low column density reached as a candidate to explain such features.

The P/V profile along the minor axis of CIG 96 (Fig. 4.7) shows emission in a wide gradient of velocities, going up to +85 km s^{-1} in the receding side and down to -145 km s^{-1} in the approaching side with respect to its central velocity. Beam effects may contribute to such dispersion (Bosma, 1978) by introducing part of the surrounding emission at different velocities. However, with the current resolution of 28"$\times$28", this effect can only explain dispersions up to $\pm 60 - 70$ km s^{-1} approximately. Counter-rotating gas clouds may also contribute to the high velocity dispersion but we do not detect any signatures of such features in the major axis, where they would

likely be visible. An outflow or the infall of extraplanar gas of different speeds may also explain the wide range of velocities but we do not detect any signs of either of them in any channel of the map.

5.2.2 Accretion of cold HI clouds

High and intermediate velocity HI clouds around the Milky Way may reach masses of $10^7 M_\odot$. However, the clouds of the Local Group have smaller typical total masses of $M_{HI}^{cloud} \simeq 10^5 - 10^6 M_\odot$ (Wakker et al., 1999) and they are expected to be several orders of magnitude below the total mass of their host galaxies.

With respect to CIG 96, from our HI cube we compute a total HI mass of $M_{CIG\ 96} \approx 10^{12} M_\odot$. The two NW and SE HI features have total masses of ~ 3.1 and $1.6 \times 10^6 M_\odot$, respectively, being are close to the detection limit achieved with our HI cube ($0.7 \times 10^6 M_\odot$). The NW HI feature meets the HI mass, spatial distribution and velocity ranges criteria to consider it a possible infalling cloud that overlaps with CIG 96 in channels $23 - 25$ (velocities $1550 - 1570\,\mathrm{km\,s^{-1}}$).

As discussed by T. C. Scott et al. (2014), these clouds are not expected to fall on an extension of the rotation curve. This reinforces that the previously discussed Southwestern side of the galaxy is likely to be the warped edge of the HI disc instead of an accreted HI cloud.

5.2.3 Pseudoring colour, column densities and minor mergers

HI is disrupted more easily than the faint optical halo substructures, which may live longer (Peñarrubia et al., 2005) than the $\sim 1.5 - 3\,\mathrm{Gyr}$ established by the quantified isolation criteria (see Sect. 5.1). The external pseudoring of CIG 96 is HI rich except for its Southern and Northeastern sides where the gas is scarce. The pseudoring colours in the Southern side are clearly redder than in the rest of the ring, in particular in the bluer Northern and Northwestern side where SF is taking place in a number of scattered regions according to their blue colours. This colour difference agrees with *GALEX* NUV and FUV results discussed by E11a.

The SF regions with high UV emission match the bluer regions of the North-Northwestern side of the pseudoring, and consistently show column densities above $8.5{\times}10^{20}\,\mathrm{cm}^{-2}$. These are higher than the redder regions which coincide with areas where the HI seems disturbed and show much lower HI column densities, as shown in the bottom panel of Fig. 4.17. The N_{HI} is measured with a beam larger than the size of the optical regions. Once resolved, we would expect to achieve an even higher N_{HI} level in the bluest regions, reaching the nominal SF value of $10^{21}\,\mathrm{cm}^{-2}$. Also, the anticorrelation observed between the scaled $g-r$ and N_{HI} seems to break in the $70°-180°$arc. This is the Eastern side of the pseudoring where the emission is very diffuse so any correlation or anticorrelation between $g-r$ and N_{HI} in this area is uncertain.

Among the mechanisms that involve the SF enhancement or quenching as well as HI asymmetries are the minor mergers with low-mass, dwarf galaxies. On the one hand, one or a few recent minor mergers with HI rich small galaxies (wet mergers) are expected to leave clear HI footprints tracing such events, let alone orbiting stellar structures (Martínez-Delgado et al., 2009) or SF enhancement in the areas where the merging occurred, i.e., bluer colours would be expected in the Southern and Northeastern areas instead of the redder colours we find. Also, these mergers could have occurred in the more diffuse and incomplete regions of the pseudoring but, again, footprints of such events are missing. On the other hand, any minor mergers with one or a few HI poor companions (dry mergers) might explain the stripped gas as well as the consequent SF quenching (even extinction) of the Northeastern and Southern regions. However, we find no optical or gaseous signature in any of these sections and the 0^{th} and 1^{st} moments indicate no link between the possible warp in the Southern arc of the pseudoring. One or various possible encounters with ultra−diffuse galaxies (UDG) of large mass−to−light ratios (P. van Dokkum et al., 2016) might be responsible for the SF in the pseudoring yet no UDG or interaction remains are detected in our observations.

The tidal footprints from older minor mergers ($t > 0.7\,\mathrm{Gyr}$, Holwerda et al. 2011c) might have disappeared within one or two galaxy revolutions. Should they have left any optical counterparts that might still be visible, they would be expected to be weak and diffuse. We may discard any candidate brighter than our SB limit.

However, the cirrus at $\mu_{r\ SDSS} = 28.5\,\mathrm{mag\,arcsec^{-2}}$ or larger prevent the detection of any candidate fainter than this limit, i.e., based solely on these optical observations, we may not discard one or more minor mergers may be responsible for the colour index variation in the pseudoring or that there actually exist counterparts to the HI features. Consequently, old minor mergers remain as a possible candidate to explain the stellar and gaseous features of CIG 96.

5.2.4 Age of the pseudoring

The blue colour of the $g - r$ representations is a good tracer of the age of the stellar population in the optical wavelengths. Schawinski et al. (2009) propose three different models to discuss age according to the $g - r$ colour observed (see Fig. 5.2). Model 1 assumes an instantaneous burst of SF with an exponential decay of 100 Myr; model 2 considers an instantaneous burst of SF with instantaneous decay as well of 10 Myr; last, model 3 assumes a constant SFR.

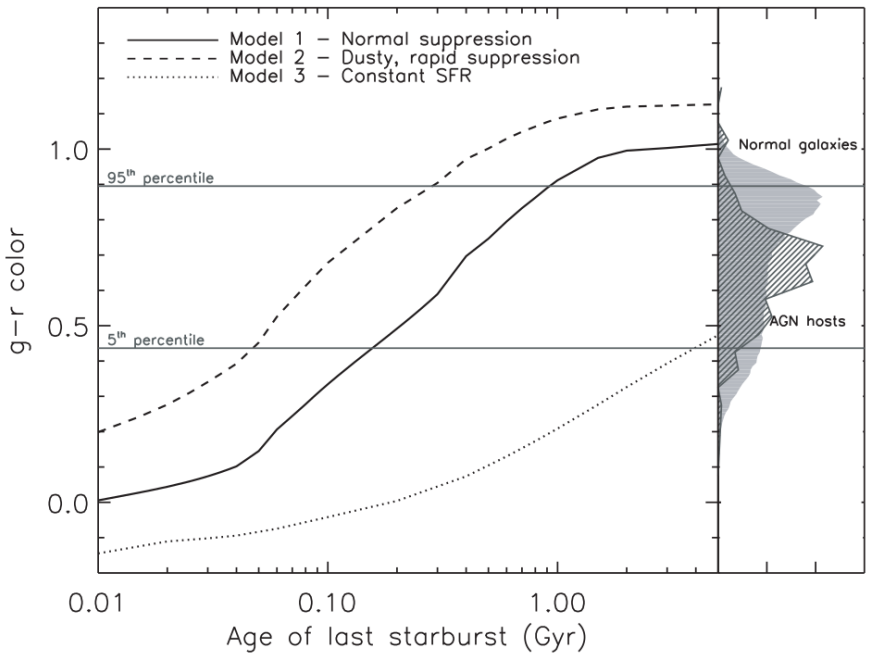

Fig. 5.2 Timescales for optical colours of AGN host galaxies and the three star formation scenarios probing the limits of possible colour evolution based on stellar evolution models (Maraston, 2005). Credit: Figure 3 from Schawinski et al. (2009).

The colour nature of the pseudoring of CIG 96 does not fit with models 1 and 2 age estimations because so recent SF would require nearby companions, powerful enough as to trigger it, or else, a transfer of gas from the inner parts towards the pseudoring in a lower period of time than the dynamical timescale of the galaxy. We do not detect signs of any of these requirements, what leads us to consider model 3 as a more likely scenario. According to it, the continuous and slow ingestion of gas from the central parts of the galaxy into the pseudoring might explain a constant SF during at least 1 Gyr.

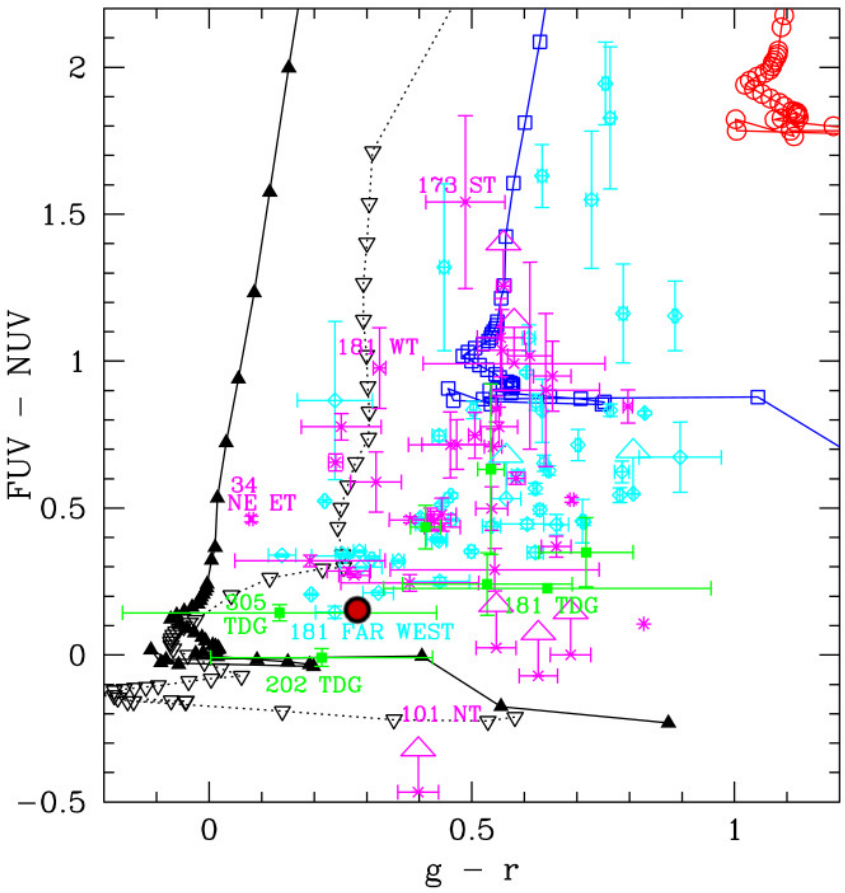

Fig. 5.3 GALEX FUV−NUV vs. $g - r$ colours for the main discs of the interacting galaxy sample (cyan marks) and their tidal features (magenta crosses), as studies by Smith et al. (2010). The position of the bluest region of the pseudoring, as measured in this work, is indicated with a large red dot according to the FUV−NUV values from E11a. Credit: Figure 19 from Smith et al. (2010).

Additionally, E11a found that the outer parts of CIG 96 have ultraviolet colours of FUV−NUV = 0.1−0.2 $\mathrm{mag}_{AB}\,\mathrm{arcsec}^{-2}$. According to this interval FUV−NUV, the low metallicity model proposed by Smith et al. (2010) fits with the expected lower metallicity in the outskirts of a galaxy (see Fig. 5.3 and position of the bluest regions of the pseudoring of CIG 96). However, it yields ages lower than 100 Myr for the pseudoring. We discard the option of a companion since we would expect to detect it further than just its influence on the outskirts.

5.2.5 Origin of the pseudoring

The rings located 2−2.5 times the radius of the bar of the galaxy are labelled as Outer Rings (OR) (Buta, 2017). OR are typical in barred galaxies and their origin is gas accumulation in the outer Lindblad resonance (OLR) (Schommer and Sullivan, 1976).

On the one hand, we find no signatures in either the optical or HI observations that suggest a collisional origin, in agreement with its high isolation level. On the other hand, the OLR is located at a distance slightly beyond twice the bar radius (Athanassoula et al., 1982). In the case of CIG 96, the bar and pseudoring optical radius are ∼5 kpc (∼30”) and ∼21 kpc (∼130”), respectively, i.e. the pseudoring is located over 4 times farther than the bar, making such distance too large to be considered an OLR of the bar, as discussed by E05.

An oval shape of the bright inner disc of the spiral galaxy might be a more reliable source to explain the origin of the pseudoring, as discussed briefly by E11a. These non-axisymmetric kinematical features can produce disturbances on the motions of gas clouds located in the outer HI disc, resulting in complete or partial resonance rings (Schwarz, 1981; Verdes-Montenegro et al., 1995; Buta and Combes, 1996). In agreement with what is expected to be found in these resonance rings, the pseudoring of CIG 96 has a symmetric shape and it is partially defined, showing diffuse optical emission and low HI column densities in regions to the North-East and South-West.

An apparent misalignment between the galaxy center and the pseudoring might be suggested by external isophotes of CIG 96 (q.v. Figs. 3.5 and 4.18). This is confirmed by the different elliptical fittings of the pseudoring that consistently show its center lies ∼1.2 kpc (∼12”) to the South of the galaxy center. However, the diffuse optical

Eastern side of the pseudoring and the high contamination of bright stars around the galaxy prevent a reliable global isophotal fitting analysis and further discussion on this regard.

The nearby stars also prevent resolving clearly the two elongated and faint arms or extensions that depart from the North and South of the disc. However, both the UV data analysed by E11a and our CAHA optical images (q.v., Figs. 3.5 and 4.13, central panel, yellow crosses) show that the Northern and Southern extensions connect the disc and the outermost regions of the galaxy where, respectively, they join the Western and Eastern sides of the pseudoring.

Chapter 6

Conclusions

The AMIGA project makes use of the CIG catalog, a sample that shows the most symmetric HI integrated profiles when compared to any other sample, even field galaxies. However, some of its members present very asymmetric profiles as well as other features whose origins remain unknown. If large asymmetries are mostly generated by interactions, the lopsidedness of certain isolated galaxies such as CIG 96 should not be observed.

CIG 96 is an isolated galaxy of the AMIGA sample with a 16% asymmetry in its HI integrated profile (see Fig. 4.1) as well as an actively star forming external pseudoring detected in the HI, optical and UV ranges (see Fig. 4.9). Our deep optical and HI observations have yielded unprecedented detail of the stellar and gaseous components of the main body and outskirts of CIG 96. The wide field of view of $1^\circ \times 1^\circ$ of VST telescope and the wavelet filtered 21 cm data from VLA/EVLA telescope allowed us to reach a maximum surface brightness and column density level of $\mu_{r\ SDSS}$ =28.7mag arcsec^{-2} and $N_{HI} = 8.9 \times 10^{18}$ cm^{-2} (5σ, beam size of 28"×28"), respectively. The optical data show in detail the structure of the pseudoring as well as a gradient in its $g - r$ colour index (see Fig. 4.13). Moreover, the HI data show previously undetected features very close to the galaxy (see Fig. 4.4).

Next, we present the main conclusions of this thesis dissertation:

- Down to these limits, we do not find any gaseous or stellar connection between CIG 96 and any galaxy in its close environment, including its closest, largest and HI rich companion NGC 864 COM01, located 15.2' (∼90 kpc) to the East (projected distance, see Fig. 4.18). Scattered Galactic cirrus show up from 28.5mag arcsec^{-2} (SDSS r band, see Fig. 3.3) in the surroundings of the galaxy and prevent any positive detection of further faint optical features beyond this depth.

- We find two low−mass HI features (∼$10^6 M_\odot$) located to the North-West and South-East edges of the galaxy, namely, the NW and SE HI features (see Fig. 4.2). The NW HI feature is visible along a number of immediate channels of the HI cube and depicts a low column density cloud ($N_{HI}^{NW} \simeq 6.5{\times}10^{19}$ cm^{-2}) connected with CIG 96 slightly to the North of its minor axis. We think that the SE HI feature, however, is a series of thin, small and spatially aligned clouds ($N_{HI}^{SE} \simeq 4.9{\times}10^{19}$ cm^{-2}) that stand out in the 0^{th} moment. The individual channels of the HI cube show that the different clouds that compose this feature are not connected between them and show no direct effect on the immediate gas of the disc edge despite its close proximity.

- We find a colour index difference of $g - r \simeq 0.4$ mag between two sides of the partially complete pseudoring (PA$_{redder}$ =70°−258° and PA$_{bluer}$ =258°−38°) that cannot be assigned to any instrumental effect (see Fig. 4.13). No environmental cause (external gas accretion or minor merger) has been identified in our data as to explain such change in the $g - r$ colour index. The outermost SF regions detected with NUV and FUV images from GALEX coherently match the blue regions of the pseudoring, which also show N_{HI} values close to 10^{21} cm^{-2}, the nominal SF value. The cause for the higher concentration of N_{HI} in certain areas of the pseudoring is still to be found.

- We have reviewed different SF models based on the FUV−NUV and $g-r$ colours to determine the approximate age of the pseudoring of CIG 96. We may discard a short lived pseudoring (∼100 Myr or younger) caused by a very recent encounter with either a similar sized galaxy (the isolation criteria discard them) or a small galaxy (we would expect to see the merger remains); instead, they favour an older pseudoring (∼1 Gyr).

- Despite the fact that bars are usually relevant candidates to play a critical role in the secular evolution of the outskirts of a galaxy by leading the matter to concentrate in the OLR, such is not the case for CIG 96. First, we do not find any significant matter concentration in the OLR of CIG 96 and, second, the pseudoring is located at almost double the radius of the expected location of the OLR based on the bar size. For these reasons, we cannot consider a bar driven accumulation of matter in the OLR as the pseudoring origin. Either an oval distortion or old, elongated arms expelled from the inner parts of the disc are more fitting explanations of the origin of the faint, distant from the galaxy center and circular pseudoring of CIG 96. SF regions are expected in secular evolution and they may be triggered by external factors such as encounters with smaller and fainter infalling HI clouds. However, we do not find evidence of any external event that may explain the SF regions of the pseudoring of CIG 96. Their origin still remains unknown.

- The lack of any remarkable tidal features or other stellar components leads us to consider that, on the one hand, any major encounter with similar sized galaxies must have never occurred, as guaranteed by the isolation times and criteria (see Sect. 5.1); on the other hand, any possible minor merger must have taken place before the last two revolutions of CIG 96 ($t > 0.8$ Gyr, approximately), letting the footprints of such encounters disappear within such time.

Chapter 7

Ongoing and future work

As described further in Chapter 2, CIG 96 has constituted the model case for the study of the causes of the HI asymmetries in the integrated profiles, out of the 184 isolated galaxies of the sample created for this purpose. Also, introduced in Sect. 2.4, other targets were observed along the thesis development with different telescopes. In this section I present possible new insights on CIG 96 as well as the rest of VST observations, possible follow−up orientations of this work.

7.1 Next steps for CIG 96

CIG 96 has proved to be a galaxy of high interest due to the particular features of its disc and close outskirts. Some questions from the earlier publications still remain unsolved and new ones have arisen throughout the work presented in this dissertation.

The pseudoring as a whole yields numerous possible approaches. For instance, the cause or causes of this structure, the colour difference and the regions with star formation may have large implications on the understanding of galaxy secular evolution, especially due to the isolation of CIG 96. A natural follow−up is to perform simulations with different internal and external initial conditions that may fit with the current morphology and kinematics of the pseudoring and offer more precise estimates of its age. Also, infrared observations in the millimeter or submillimeter ranges (ALMA

being a perfect candidate) might trace the molecular gas and expand our knowledge on the star forming regions of the pseudoring.

Our interferometric observations were designed to recover as much emission as possible (VLA and EVLA in D and mainly C configurations) aiming to detect faint gaseous structures. Observing further in D configuration or the observations from VLASS survey (taken in B and A configurations, currently under development at JVLA) might help to bring up other structures of different sizes and densities that can complement the already detected features residing in the outskirts of the galaxy.

7.2 A first look at other targets of the sample

It has been proved in this dissertation that the deep optical observations are a key tool for the study of the causes of the asymmetric HI integrated profiles. For this reason, all the optical data presented and described in Sect. 2.4 guarantee the continuation of the project and may potentially open new research paths within the AMIGA project.

Out of the previously mentioned observations, 10 galaxies were observed with OmegaCAM instrument at VST. These galaxies are CIG 11, CIG 33, CIG 59, CIG 152, CIG 154, CIG 279, CIG 568, CIG 1002, CIG 1027 and CIG 1047 and, as CIG 96, they were all reduced with AstroWISE pipeline. We discarded CIG 1027 in the current context because it has been reported by different works as an interacting system (Verley et al., 2007b, and references therein), as our observations also confirm.

A total of 7 OBs per galaxy were submitted, accounting for a total exposure time of 4h 47min distributed in 16 exposures of 154 s per OB, all taken with the SDSS r filter and mean seeing $\leqslant 1.2$". The resulting images cover a wider field of view than the expected $1^\circ \times 1^\circ$ due to the dithering patterns yet the homogeneous coverage is approximately of such size. In Table 7.1 we indicate the distance to the galaxies, their inclination, major axis, field of view of such homogeneous coverage, the surface brightness limit reached in each case, whether the field presented signs of cirrus and their asymmetry ratios. In the following sections, we present a brief introduction of the results for each one of them.

Table 7.1 Data of the other galaxies observed with Omegacam (VST) and reduced with AstroWISE pipeline.

Target	Type [a]	D [b]	I [c]	d_{ang} [d]	d_{phys} [d]	FoV [e]	SB_{lim} [f]	Cirrus [g]	$\mathcal{A}_{1/h}$ [h]
CIG 11	Scd	52.5	67.0	1.57	23.9	62'×61'	27.8	Y	1.45 ± 0.07
CIG 33	Scd	59.7	40.2	1.03	17.8	62'×63'	29.0	N	1.42 ± 0.04
CIG 59	Scd	57.2	38.5	1.27	21.2	61'×63'	28.9	N	1.07 ± 0.01
CIG 152	Scd	32.3	62.1	1.36	12.7	60'×62'	28.6	N	1.46 ± 0.06
CIG 154	Sc	59.7	40.2	1.03	17.8	61'×62'	28.3	Y	1.08 ± 0.07
CIG 279	Sbc	22.5	70.8	1.64	10.8	61'×61'	28.3	N	1.10 ± 0.05
CIG 568	Sc	135.7	26.2	1.03	40.7	61'×62'	27.3	P	1.08 ± 0.07
CIG 1002	Sc	89.7	62.9	1.11	28.9	60'×60'	27.6	Y	1.51 ± 0.08
CIG 1047	Sbc	32.6	90.0	2.04	19.3	61'×61'	27.9	Y	1.27 ± 0.04

Notes.
[a] Morphological type according to Fernández Lorenzo et al. (2012).
[b] Physical distance to the galaxy, in Mpc, from Fernández Lorenzo et al. (2012).
[c] Inclination between line of sight and polar axis, in degrees, from Fernández Lorenzo et al. (2012).
[d] Angular and physical sizes of the major axis, in arcmin and kpc, respectively, from Fernández Lorenzo et al. (2012).
[e] Field of view with homogeneous coverage, in arcmin × arcmin.
[f] Surface brightness limit in SDSS r band reached in the indicated field of view, in mag arcsec^{-2}.
[g] Presence of cirrus in the field brighter than the SB limit (Yes/No/Possible).
[h] HI asymmetry parameter and final error, according to E11b.

7.2.1 CIG 11

The field around CIG 11 shows some signs of cirrus, especially to the West of the galaxy (see Fig. 7.2). There are no apparent traces of tidal tails or other strong stellar features that can suggest the high asymmetric HI profile ($\mathcal{A}_{1/h}$= 1.45) of this galaxy.

7.2.2 CIG 33

The image of CIG 33 has the faintest surface brightness level among the VST observations up to date (see Fig. 7.3). The Southern and North-Northwestern areas of the galaxy show signs of perturbations at levels of ∼28.5 mag arcsec^{-2} (similar to those of CIG 96). We cannot discard that either of these is the result of the crossing of a companion.

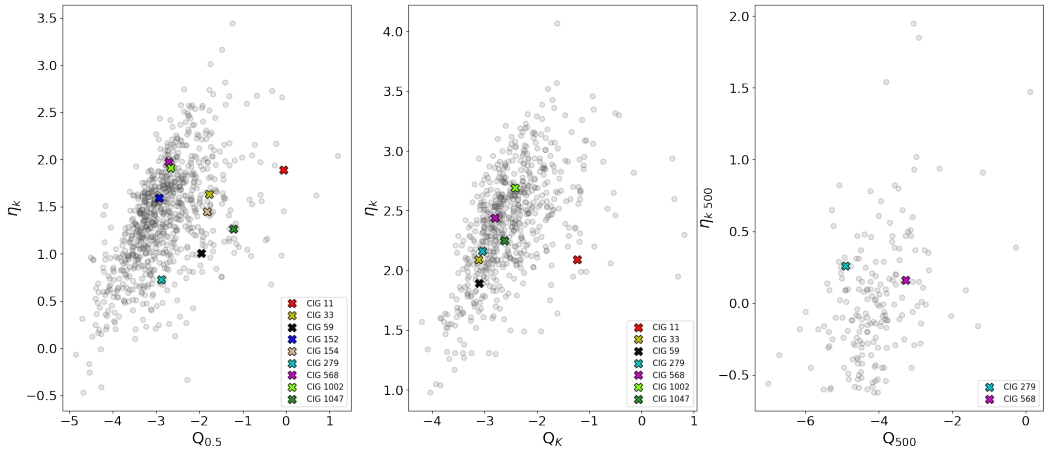

Fig. 7.1 *Left panel*: position of CIG 11, CIG 33, CIG 59, CIG 152, CIG 154, CIG 279, CIG 568, CIG 1002 and CIG 1047 in the isolation map, according to the isolation parameters of V07. The grey points represent the isolation values for all the AMIGA galaxies with available data for comparison. *Central panel*: same as in the left panel but according to the isolation parameters revised by A13, using photometric data. CIG 152 and CIG 154 could not be computed due to the lack of photometric data. *Right panel*: same as in the central panel but according to the isolation parameters revised by A13, using spectroscopic data. The isolation could be computed only for CIG 279 and CIG 568.

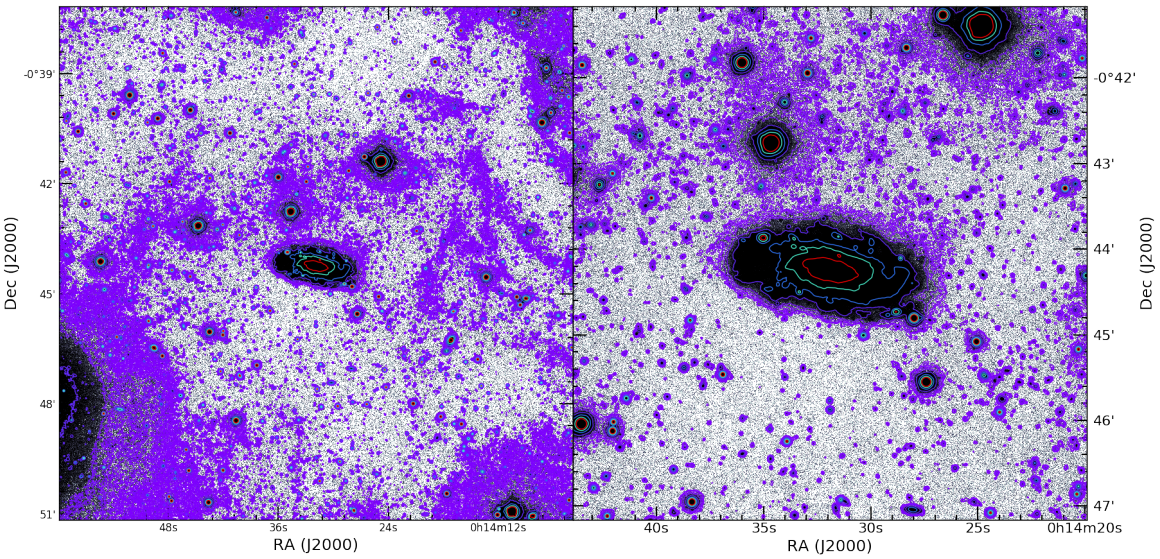

Fig. 7.2 CIG 11. *Left panel*: central 14'×14' of the VST image. Contours are set on 22, 23, 24, 25, 26.0, 26.5, 27.0, 27.3, 27.7 mag arcsec^{-2} and smoothed with a Gaussian kernel of 3 pixel radius. *Right panel*: closer view of the galaxy, central 6'×6' of the image. Same contours as in the left panel.

Table 7.2 Isolation parameters according to V07 and A13 and HI integrated profile asymmetry level of the galaxies observed with Omegacam (VST).

Target	η_k / $Q_{0.5}$ [a] V07	η_k / $Q_{0.5}$ [b] A13, photom.	η_k / $Q_{0.5}$ [c] A13, spectr.
CIG 11	1.889 / -0.059	2.09 / -1.23	–
CIG 33	1.634 / -1.771	2.09 / -3.11	–
CIG 59	1.004 / -1.957	1.89 / -3.1	–
CIG 152	1.591 / -2.929	–	–
CIG 154	1.449 / -1.825	–	–
CIG 279	0.725 / -2.875	2.16 / -3.04	0.26 / -4.91
CIG 568	1.972 / -2.708	2.44 / -2.8	0.16 / -3.28
CIG 1002	1.910 / -2.657	2.69 / -2.42	–
CIG 1047	1.261 / -1.214	2.25 / -2.62	-

Notes.
[a] Isolation criteria of Verley et al. (2007c).
[b] Isolation criteria according to the photometric data of Argudo-Fernández et al. (2013).
[c] Isolation criteria according to the spectroscopic data of Argudo-Fernández et al. (2013).

7.2.3 CIG 59

This image shows a certain over−subtraction of the sky in a 1'−2' radius around the galaxy that we could not remove in the reduction process. This is likely due to the removal of the halos produced by the close bright stars. We detect the flocculent elongated arms down to 28.6−28.9 mag arcsec^{-2} (see Fig. 7.4).

7.2.4 CIG 152

Despite the large star to the East, the almost overlapping star to the South-Southeast and a certain over−subtraction in the sky nearby to the galaxy, there is a clear double feature in the close surroundings: a small galaxy located ∼1' to the West and, specially, a diffuse cloud of approximately 20"×20" located ∼1' to the North and possibly connected to CIG 152 (see Fig. 7.5). There is no clear evidence of cirrus in the field.

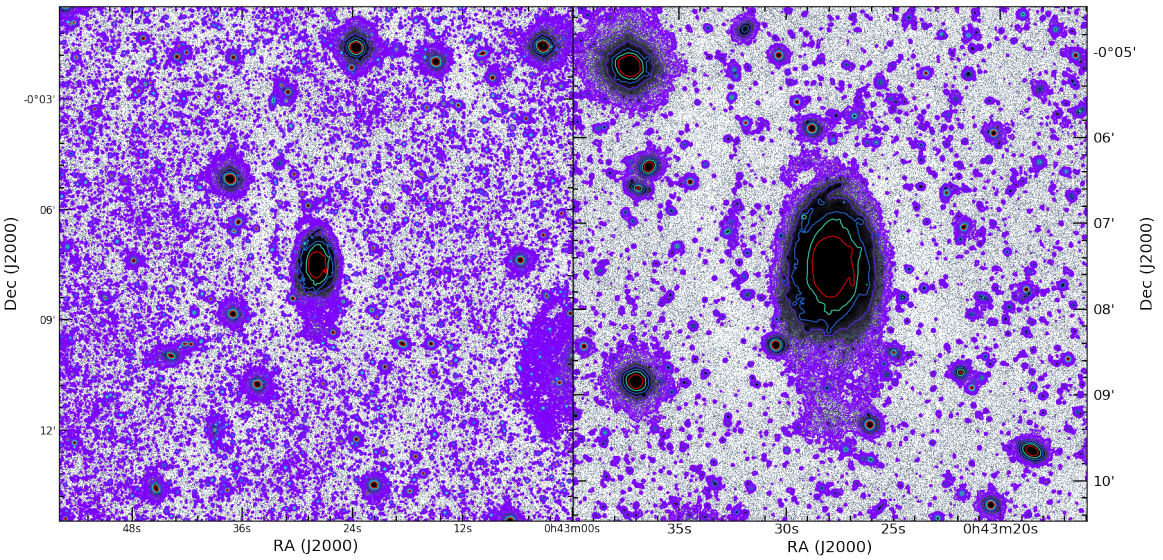

Fig. 7.3 CIG 33. *Left panel*: central 14'×14' of the VST image. Contours are set on 22, 23, 24, 25, 26.0, 26.5, 27.0, 27.5, 28.0, 28.5, 28.9 mag arcsec^{-2} and smoothed with a Gaussian kernel of 3 pixel radius. *Right panel*: closer view of the galaxy, central 6'×6' of the image. Same contours as in the left panel.

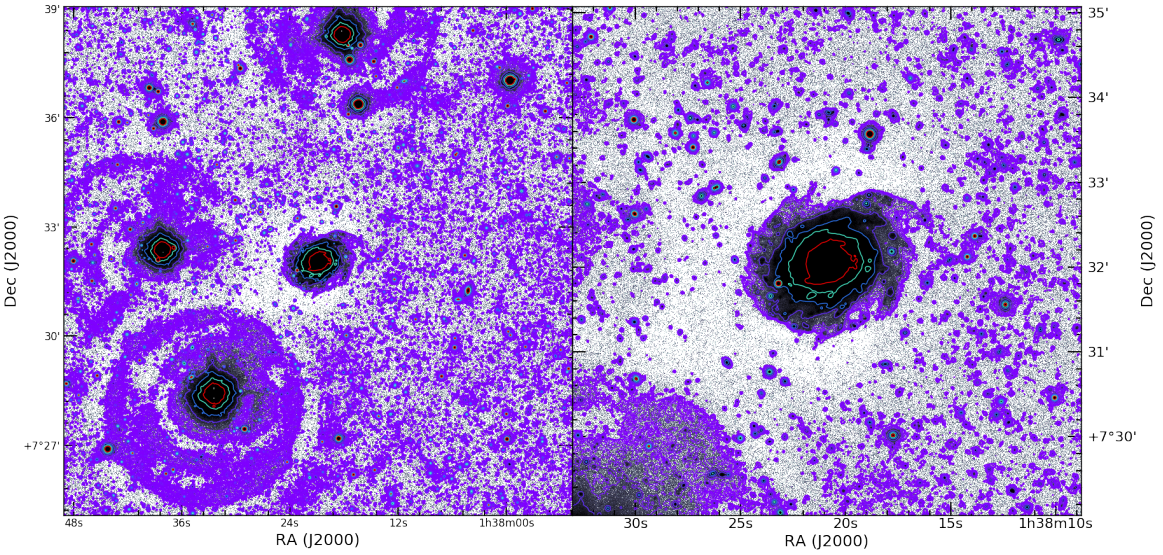

Fig. 7.4 CIG 59. *Left panel*: central 14'×14' of the VST image. Contours are set on 22, 23, 24, 25, 26.0, 26.5, 27.0, 27.5, 28.0, 28.4, 28.8 mag arcsec^{-2} and smoothed with a Gaussian kernel of 3 pixel radius. *Right panel*: closer view of the galaxy, central 6'×6' of the image. Same contours as in the left panel.

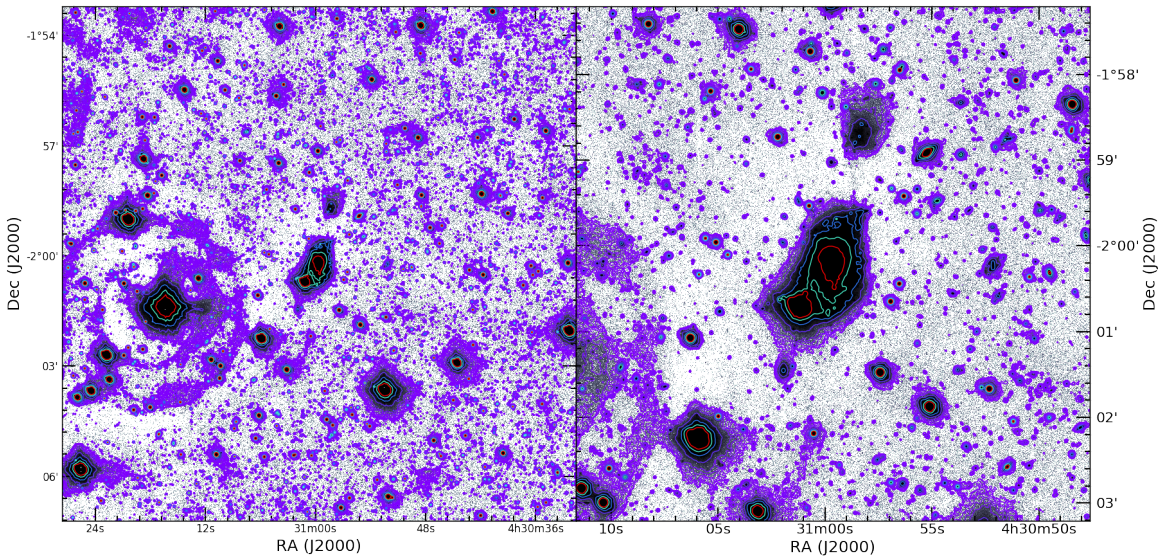

Fig. 7.5 CIG 152. *Left panel*: central 14'×14' of the VST image. Contours are set on 22, 23, 24, 25, 26.0, 26.5, 27.0, 27.5, 28.0, 28.5 mag arcsec^{-2} and smoothed with a Gaussian kernel of 3 pixel radius. *Right panel*: closer view of the galaxy, central 6'×6' of the image. Same contours as in the left panel.

7.2.5 CIG 154

This galaxy does not show remarkable features in the surroundings except for a slight over−subtraction around it (see Fig. 7.6). The field seems clean yet there may be very faint cirrus showing up at the detection limit of the image. To confirm this, a deeper image would be necessary.

7.2.6 CIG 279

The body and close outskirts of this galaxy show no particular feature neither signs of cirrus. However, there is an elongated and diffuse structure of approximately 1'-1.5' size located at ∼1' to the South-East of CIG 279 (see Fig. 7.7).

7.2.7 CIG 568

The image of CIG 568 reached a lower surface brightness level than others yet it shows a diffuse and large structure that surrounds the galaxy departing from the North towards

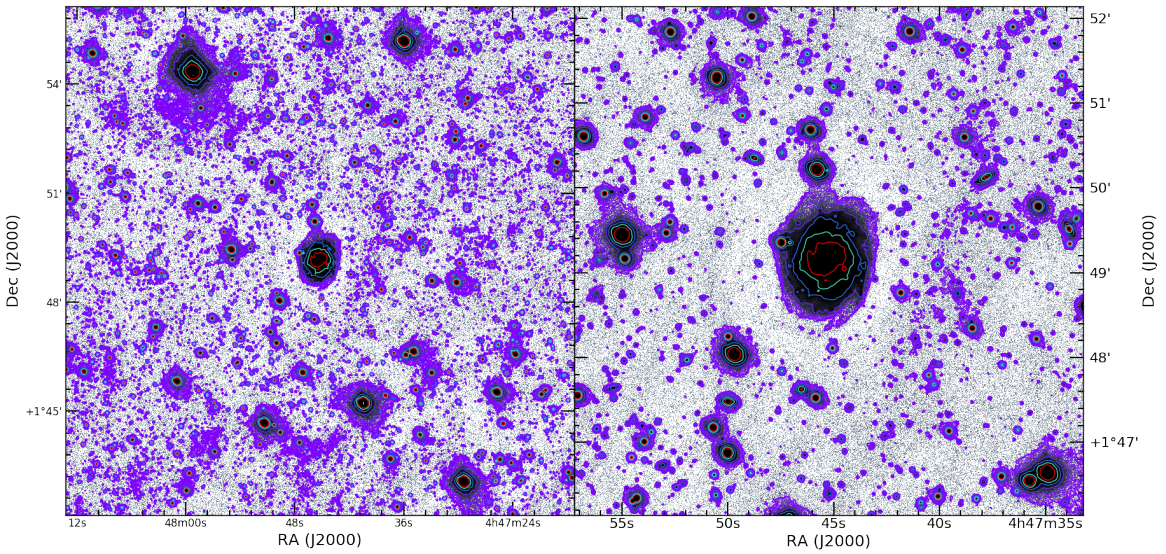

Fig. 7.6 CIG 154. *Left panel*: central 14'×14' of the VST image. Contours are set on 22, 23, 24, 25, 26.0, 26.5, 27.0, 27.5, 28.0, 28.2 mag arcsec^{-2} and smoothed with a Gaussian kernel of 3 pixel radius. *Right panel*: closer view of the galaxy, central 6'×6' of the image. Same contours as in the left panel.

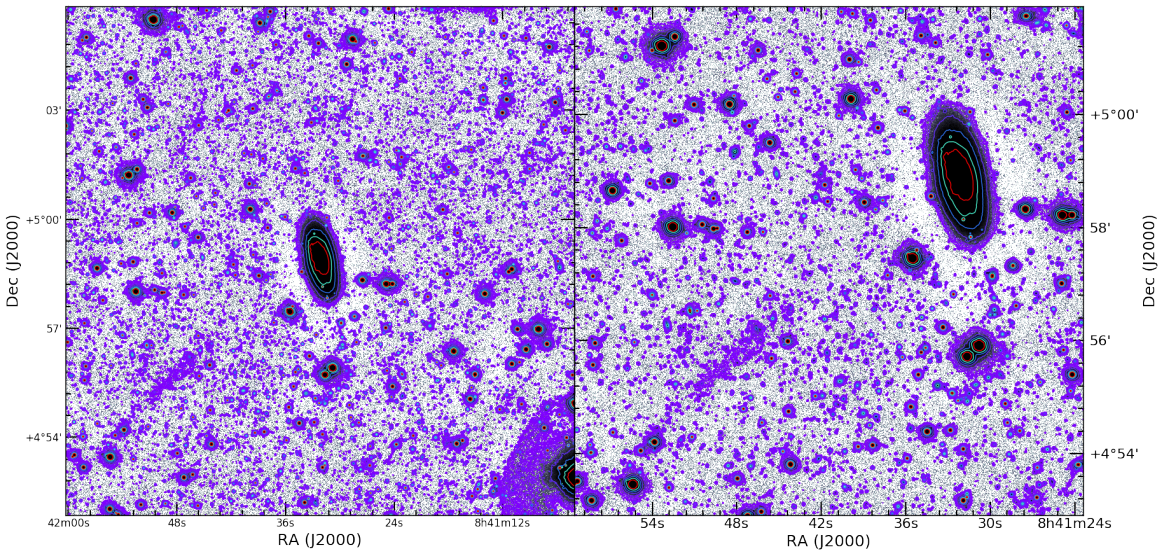

Fig. 7.7 CIG 279. *Left panel*: central 14'×14' of the VST image. Contours are set on 22, 23, 24, 25, 26.0, 26.5, 27.0, 27.5, 28.0, 28.2 mag arcsec^{-2} and smoothed with a Gaussian kernel of 3 pixel radius. *Right panel*: closer view of the galaxy, central 6'×6' of the image. Same contours as in the left panel.

the North-West. We cannot confirm its nature but we cannot confirm whether it is due to cirrus or a stellar structure (see Fig. 7.8). However, there is a very faint, diffuse and

elongated structure of ∼30” size located ∼1’ to the South of the galaxy. This structure seems independent and there are no evidences of a connection to the contaminated Eastern side of the image neither the previously mentioned diffuse structure to the North-Northwestern side.

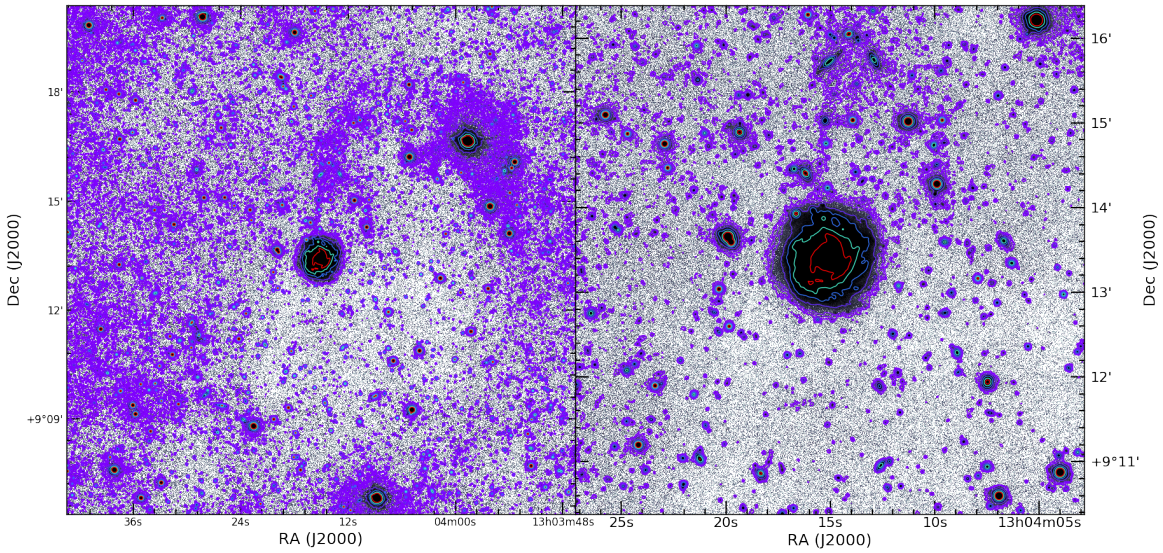

Fig. 7.8 CIG 568. *Left panel*: central 14’×14’ of the VST image. Contours are set on 22, 23, 24, 25, 26.0, 26.4, 26.6, 26.8, 27.0, 27.2, 27.3, 27.4 mag arcsec^{-2} and smoothed with a Gaussian kernel of 3 pixel radius. *Right panel*: closer view of the galaxy, central 6’×6’ of the image. Same contours as in the left panel.

7.2.8 CIG 1002

The field around this galaxy is heavily contaminated by cirrus that hinder the positive identification of optical structures around it (see Fig. 7.9). There is another galaxy located in the Southwestern edge of CIG 1002 towards the Western side of uncertain nature. A search in redshift did not return any detections.

7.2.9 CIG 1047

CIG 1047 is an edge−on galaxy and it is surrounded by cirrus. Despite the bright star to the South-West, the same side of the galaxy shows an elongation, slightly warped towards the West (see Fig. 7.10).

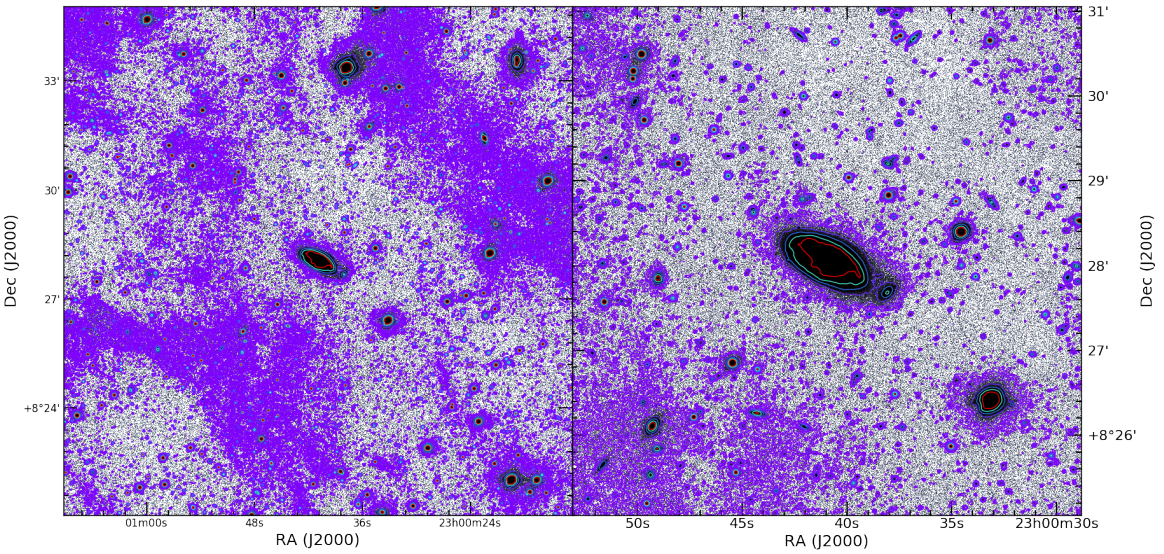

Fig. 7.9 CIG 1002. *Left panel*: central 14'×14' of the VST image. Contours are set on 22, 23, 24, 25, 26.0, 26.5, 27.0, 27.5 mag arcsec^{-2} and smoothed with a Gaussian kernel of 3 pixel radius. *Right panel*: closer view of the galaxy, central 6'×6' of the image. Same contours as in the left panel.

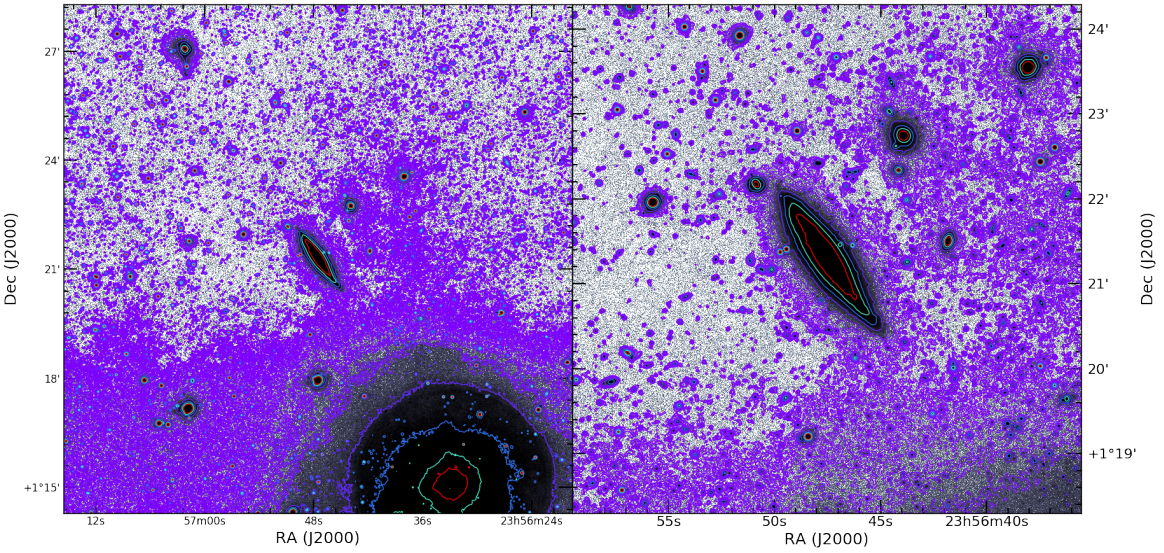

Fig. 7.10 CIG 1047. *Left panel*: central 14'×14' of the VST image. Contours are set on 22, 23, 24, 25, 26.0, 26.5, 27.0, 27.5, 27.8 mag arcsec^{-2} and smoothed with a Gaussian kernel of 3 pixel radius. *Right panel*: closer view of the galaxy, central 6'×6' of the image. Same contours as in the left panel.

7.3 Future work with the targets of the sample

The previous images, from Fig. 7.2 to 7.10, the tables 7.1 and 7.2, and the isolation plots of Fig. 7.1 are shown as an introduction to the forthcoming steps to be taken in the framework of the deep observations of highly isolated galaxies and no statistical conclusion can be extracted from them yet.

The targets of the sample built to study the asymmetries in isolated galaxies (see Sect. 2.3) cover a wide range of the two asymmetry parameters. Currently, the 32 targets already observed with different telescopes, including the 10 galaxies observed with VST in Sect. 7.2, show asymmetry parameters that span from $Q \simeq$-3.3 to $\simeq 0$ and $\eta_k \simeq 0.7$ to $\simeq 2$ according to V07, from $Q \simeq$-4.2 to $\simeq$-1.2 and $\eta_k \simeq 1.0$ to $\simeq 2.7$ according to A13 photometric data and from $Q \simeq$-5.4 to $\simeq$-3.3 and $\eta_k \simeq 0$ to $\simeq 0.8$ according to A13 spectroscopic data. Besides, the distribution of the HI asymmetry ratios is also well covered throughout the sample. Some targets show highly symmetrical HI integrated profiles, e.g. $\mathcal{A}_{1/h\ CIG\ 772} = 1.00 \pm 0.05$, that raise up to highly asymmetrical profiles, e.g. $\mathcal{A}_{1/h\ CIG\ 1002} = 1.51 \pm 0.08$.

Taking the model case of CIG 96 as the leading example, the next steps to be followed with other targets may include a thorough study of the deep images at the lowest surface brightness levels reached in each case, a revision and search for atypical features in the inner components of the galaxy as well as in the outskirts that may account for the asymmetrical HI profiles, obtaining images in different optical bands to perform colour analysis of the galaxy and the relevant faint structures, a detailed study of the implications of any faint features with respect to their isolation level, any possible correlation between the isolation level with the HI asymmetry ratios and, in the end, the search for any clues that may help to expand our knowledge on galaxy formation and evolution.

References

Aars, C. E., P. M. Marcum, and M. N. Fanelli (2001). "A Study of the Projected Galaxy Density around Nine Isolated Elliptical Galaxies". In: *AJ* 122, pp. 2923–2939. DOI: 10.1086/324106.

Abell, G. O. (1958). "The Distribution of Rich Clusters of Galaxies." In: *ApJS* 3, p. 211. DOI: 10.1086/190036.

Abell, G. O., H. G. Corwin Jr., and R. P. Olowin (1989). "A catalog of rich clusters of galaxies". In: *ApJS* 70, pp. 1–138. DOI: 10.1086/191333.

Abolfathi, B. et al. (2018). "The Fourteenth Data Release of the Sloan Digital Sky Survey: First Spectroscopic Data from the Extended Baryon Oscillation Spectroscopic Survey and from the Second Phase of the Apache Point Observatory Galactic Evolution Experiment". In: *ApJS* 235, 42, p. 42. DOI: 10.3847/1538-4365/aa9e8a. arXiv: 1707.09322.

Abraham, R. G., F. Valdes, H. K. C. Yee, and S. van den Bergh (1994). "The morphologies of distant galaxies. 1: an automated classification system". In: *ApJ* 432, pp. 75–90. DOI: 10.1086/174550.

Abraham, R. G. and P. G. van Dokkum (2014). "Ultra-Low Surface Brightness Imaging with the Dragonfly Telephoto Array". In: *PASP* 126, p. 55. DOI: 10.1086/674875. arXiv: 1401.5473 [astro-ph.IM].

Abraham, R. G. et al. (1996). "The Morphologies of Distant Galaxies. II. Classifications from the Hubble Space Telescope Medium Deep Survey". In: *ApJS* 107, p. 1. DOI: 10.1086/192352.

Adelman-McCarthy, J. K. et al. (2006). "The Fourth Data Release of the Sloan Digital Sky Survey". In: *ApJS* 162, pp. 38–48. DOI: 10.1086/497917. eprint: astro-ph/0507711.

Aguerri, J. A. L., I. Agulli, A. Diaferio, and C. Dalla Vecchia (2017). "Deep spectroscopy in nearby galaxy clusters - III. Orbital structure of galaxies in Abell 85". In: *MNRAS* 468, pp. 364–377. DOI: 10.1093/mnras/stx457. arXiv: 1703.00740.

Agulli, I. et al. (2016). "Deep spectroscopy of nearby galaxy clusters - I. Spectroscopic luminosity function of Abell 85". In: *MNRAS* 458, pp. 1590–1603. DOI: 10.1093/mnras/stw422. arXiv: 1602.07308.

References

Ahn, C. P. et al. (2012). "The Ninth Data Release of the Sloan Digital Sky Survey: First Spectroscopic Data from the SDSS-III Baryon Oscillation Spectroscopic Survey". In: *ApJS* 203, 21, p. 21. DOI: 10.1088/0067-0049/203/2/21. arXiv: 1207.7137 [astro-ph.IM].

Alatalo, K. et al. (2015). "Star Formation Suppression in Compact Group Galaxies: A New Path to Quenching?" In: *ApJ* 812, 117, p. 117. DOI: 10.1088/0004-637X/812/2/117. arXiv: 1509.05779.

Annibali, F., R. Grützbauch, R. Rampazzo, A. Bressan, and W. W. Zeilinger (2011). "Nature vs. nurture in the low-density environment: structure and evolution of early-type dwarf galaxies in poor groups". In: *A&A* 528, A19, A19. DOI: 10.1051/0004-6361/201015635. arXiv: 1011.4965.

Ansdell, M. et al. (2018). "ALMA Survey of Lupus Protoplanetary Disks. II. Gas Disk Radii". In: *ApJ* 859, 21, p. 21. DOI: 10.3847/1538-4357/aab890. arXiv: 1803.05923 [astro-ph.EP].

Argudo-Fernández, M. et al. (2013). "The AMIGA sample of isolated galaxies. XII. Revision of the isolation degree for AMIGA galaxies using the SDSS". In: *A&A* 560, A9, A9. DOI: 10.1051/0004-6361/201321326. arXiv: 1311.0856 [astro-ph.CO].

Argudo-Fernández, M. et al. (2014). "Effects of the environment on galaxies in the Catalogue of Isolated Galaxies: physical satellites and large scale structure". In: *A&A* 564, A94, A94. DOI: 10.1051/0004-6361/201322498. arXiv: 1402.5526.

Ashley, T., C. E. Simpson, B. G. Elmegreen, M. Johnson, and N. R. Pokhrel (2017). "The HI Chronicles of LITTLE THINGS BCDs. III. Gas Clouds in and around Mrk 178, VII Zw 403, and NGC 3738". In: *AJ* 153, 132, p. 132. DOI: 10.3847/1538-3881/aa5ca7. arXiv: 1701.08169.

Ashley, T. et al. (2014). "The H I Chronicles of LITTLE THINGS BCDs II: The Origin of IC 10's H I Structure". In: *AJ* 148, 130, p. 130. DOI: 10.1088/0004-6256/148/6/130. arXiv: 1409.5406.

Athanassoula, E. (2003). "What determines the strength and the slowdown rate of bars?" In: *MNRAS* 341, pp. 1179–1198. DOI: 10.1046/j.1365-8711.2003.06473.x. eprint: astro-ph/0302519.

— (2010). "Structures in Galaxies: Nature versus Nurture. Input from Theory and Simulations". In: *Galaxies in Isolation: Exploring Nature Versus Nurture*. Ed. by L. Verdes-Montenegro, A. Del Olmo, and J. Sulentic. Vol. 421. Astronomical Society of the Pacific Conference Series, p. 157. arXiv: 0910.5180 [astro-ph.CO].

— (2013). "Bars and secular evolution in disk galaxies: Theoretical input". In: *Secular Evolution of Galaxies*. Ed. by J. Falcón-Barroso and J. H. Knapen, p. 305.

Athanassoula, E., A. Bosma, M. Creze, and M. P. Schwarz (1982). "On the sizes of rings and lenses in disk galaxies". In: *A&A* 107, pp. 101–106.

Athanassoula, E. and A. Misiriotis (2002). "Morphology, photometry and kinematics of N -body bars - I. Three models with different halo central concentrations".

In: *MNRAS* 330, pp. 35–52. DOI: 10.1046/j.1365-8711.2002.05028.x. eprint: astro-ph/0111449.

Baldwin, J. E., D. Lynden-Bell, and R. Sancisi (1980). "Lopsided galaxies". In: *MNRAS* 193, pp. 313–319. DOI: 10.1093/mnras/193.2.313.

Balkowski, C. and P. Chamaraux (1981). "The H I content of isolated galaxies". In: *A&A* 97, pp. 223–231.

Banerjee, A., N. N. Patra, J. N. Chengalur, and A. Begum (2013). "A slow bar in the dwarf irregular galaxy NGC 3741". In: *MNRAS* 434, pp. 1257–1263. DOI: 10.1093/mnras/stt1083. arXiv: 1308.3029.

Beckwith, S. V. W. et al. (2006). "The Hubble Ultra Deep Field". In: *AJ* 132, pp. 1729–1755. DOI: 10.1086/507302. eprint: astro-ph/0607632.

Bijaoui, A. (1991). In: *The Wavelet Transform, Data Analysis Workshop 3*.

Binney, J. J. (1992). "WARPS". In: *ARA&A* 30, pp. 51–74. DOI: 10.1146/annurev.aa.30.090192.000411.

Bitsakis, T. et al. (2016). "Studying the evolution of galaxies in compact groups over the past 3 Gyr - II. The importance of environment in the suppression of star formation". In: *MNRAS* 459, pp. 957–970. DOI: 10.1093/mnras/stw686. arXiv: 1603.06007.

Bland-Hawthorn, J., P. R. Maloney, A. Stephens, A. Zovaro, and A. Popping (2017). "In Search of Cool Flow Accretion onto Galaxies: Where Does the Disk Gas End?" In: *ApJ* 849, 51, p. 51. DOI: 10.3847/1538-4357/aa8f45. arXiv: 1709.08733.

Blanton, M. R. and J. Moustakas (2009). "Physical Properties and Environments of Nearby Galaxies". In: *ARA&A* 47, pp. 159–210. DOI: 10.1146/annurev-astro-082708-101734. arXiv: 0908.3017.

Borthakur, S., M. S. Yun, and L. Verdes-Montenegro (2010). "Detection of Diffuse Neutral Intragroup Medium in Hickson Compact Groups". In: *ApJ* 710, 385-407, pp. 385–407. DOI: 10.1088/0004-637X/710/1/385. arXiv: 0912.0297 [astro-ph.CO].

Bosma, A. (1978). "The distribution and kinematics of neutral hydrogen in spiral galaxies of various morphological types". PhD thesis. PhD Thesis, Groningen Univ., (1978).

— (2017). "HI in the Outskirts of Nearby Galaxies". In: *Outskirts of Galaxies*. Ed. by J. H. Knapen, J. C. Lee, and A. Gil de Paz. Vol. 434. Astrophysics and Space Science Library, p. 209. DOI: 10.1007/978-3-319-56570-5_7. arXiv: 1612.05272.

Bosma, A. and K. C. Freeman (1993). "On the central surface brightness problem in disk galaxies". In: *AJ* 106, pp. 1394–1404. DOI: 10.1086/116734.

Bouquin, A. Y. K. et al. (2018). "The GALEX/S^{4}G Surface Brightness and Color Profiles Catalog. I. Surface Photometry and Color Gradients of Galaxies". In: *ApJS* 234, 18, p. 18. DOI: 10.3847/1538-4365/aaa384. arXiv: 1710.00955.

References

Bourke, Tyler L. et al., eds. (2015). *Proceedings, Advancing Astrophysics with the Square Kilometre Array (AASKA14)*. Vol. AASKA14. SISSA. SISSA. URL: http://pos.sissa.it/cgi-bin/reader/conf.cgi?confid=215.

Bournaud, F., F. Combes, C. J. Jog, and I. Puerari (2005). "Lopsided spiral galaxies: evidence for gas accretion". In: *A&A* 438, pp. 507–520. DOI: 10.1051/0004-6361:20052631. eprint: astro-ph/0503314.

Brisbin, D. et al. (2017). "An ALMA survey of submillimeter galaxies in the COSMOS field: Multiwavelength counterparts and redshift distribution". In: *A&A* 608, A15, A15. DOI: 10.1051/0004-6361/201730558. arXiv: 1708.05748.

Broeils, A. H. and H. van Woerden (1994). "A search for spiral galaxies with extended HI disks." In: *A&AS* 107, pp. 129–176.

Bundy, K. et al. (2015). "Overview of the SDSS-IV MaNGA Survey: Mapping nearby Galaxies at Apache Point Observatory". In: *ApJ* 798, 7, p. 7. DOI: 10.1088/0004-637X/798/1/7. arXiv: 1412.1482.

Buta, R. J. (2013). "Galaxy Morphology". In: *Secular Evolution of Galaxies*. Ed. by J. Falcón-Barroso and J. H. Knapen, p. 155.

— (2017). "Galactic rings revisited - I. CVRHS classifications of 3962 ringed galaxies from the Galaxy Zoo 2 Database". In: *MNRAS* 471, pp. 4027–4046. DOI: 10.1093/mnras/stx1829. arXiv: 1707.06589.

Buta, R. J. and F. Combes (1996). "Galactic Rings". In: *Fund. Cosmic Phys.* 17, pp. 95–281.

Buta, R. J., S. Vasylyev, H. Salo, and E. Laurikainen (2005). "The Distribution of Bar and Spiral Arm Strengths in Disk Galaxies". In: *AJ* 130, pp. 506–523. DOI: 10.1086/431251. eprint: astro-ph/0505079.

Buta, R. J. and X. Zhang (2009). "Pattern Corotation Radii from Potential-Density Phase-Shifts for 153 OSUBGS Sample Galaxies". In: *ApJS* 182, pp. 559–583. DOI: 10.1088/0067-0049/182/2/559. arXiv: 0903.4695.

Buta, R. J. et al. (2015). "A Classical Morphological Analysis of Galaxies in the Spitzer Survey of Stellar Structure in Galaxies (S4G)". In: *ApJS* 217, 32, p. 32. DOI: 10.1088/0067-0049/217/2/32. arXiv: 1501.00454.

Cappellari, M. et al. (2011). "The ATLAS 3D project - I. A volume-limited sample of 260 nearby early-type galaxies: science goals and selection criteria". In: *MNRAS* 413, pp. 813–836. DOI: 10.1111/j.1365-2966.2010.18174.x. arXiv: 1012.1551.

Clauwens, B., J. Schaye, and M. Franx (2015). "An assessment of the evidence from ATLAS 3D for a variable initial mass function". In: *MNRAS* 449, pp. 4091–4104. DOI: 10.1093/mnras/stv603. arXiv: 1406.0854.

Colbert, J. W., J. S. Mulchaey, and A. I. Zabludoff (2001). "The Optical and Near-Infrared Morphologies of Isolated Early-Type Galaxies". In: *AJ* 121, pp. 808–819. DOI: 10.1086/318758. eprint: astro-ph/0010534.

Colless, M. et al. (2001). "The 2dF Galaxy Redshift Survey: spectra and redshifts". In: *MNRAS* 328, pp. 1039–1063. DOI: 10.1046/j.1365-8711.2001.04902.x. eprint: astro-ph/0106498.

Comerón, S. et al. (2010). "AINUR: Atlas of Images of NUclear Rings". In: *MNRAS* 402, pp. 2462–2490. DOI: 10.1111/j.1365-2966.2009.16057.x. arXiv: 0908.0272.

Condon, J. J. et al. (1998). "The NRAO VLA Sky Survey". In: *AJ* 115, pp. 1693–1716. DOI: 10.1086/300337.

Connolly, A. J., A. S. Szalay, M. Dickinson, M. U. SubbaRao, and R. J. Brunner (1997). "The Evolution of the Global Star Formation History as Measured from the Hubble Deep Field". In: *ApJ* 486, pp. L11–L14. DOI: 10.1086/310829. eprint: astro-ph/9706255.

Conselice, C. J. (2003). "The Relationship between Stellar Light Distributions of Galaxies and Their Formation Histories". In: *ApJS* 147, pp. 1–28. DOI: 10.1086/375001. eprint: astro-ph/0303065.

— (2014). "The Evolution of Galaxy Structure Over Cosmic Time". In: *ARA&A* 52, pp. 291–337. DOI: 10.1146/annurev-astro-081913-040037. arXiv: 1403.2783.

Cormier, D. et al. (2016). "The BLUEDISK Survey: molecular gas distribution and scaling relations in the context of galaxy evolution". In: *MNRAS* 463, pp. 1724–1739. DOI: 10.1093/mnras/stw2097. arXiv: 1608.07607.

Crnojević, D. et al. (2014). "A PAndAS view of M31 dwarf elliptical satellites: NGC 147 and NGC 185". In: *MNRAS* 445, pp. 3862–3877. DOI: 10.1093/mnras/stu2003. arXiv: 1409.7065.

Davidge, T. J. (2015). "The Star-forming Histories of the Nucleus, Bulge, and Inner Disk of NGC 5102: Clues to the Evolution of a Nearby Lenticular Galaxy". In: *ApJ* 799, 97, p. 97. DOI: 10.1088/0004-637X/799/1/97. arXiv: 1412.2086.

Davis, T. A. et al. (2014). "The ATLAS 3D Project - XXVIII. Dynamically driven star formation suppression in early-type galaxies". In: *MNRAS* 444, pp. 3427–3445. DOI: 10.1093/mnras/stu570. arXiv: 1403.4850.

de Vaucouleurs, G. (1958). "Photoelectric photometry of the Andromeda nebula in the UBV system". In: *ApJ* 128, p. 465. DOI: 10.1086/146564.

— (1959). "Classification and Morphology of External Galaxies." In: *Handbuch der Physik* 53, p. 275.

de Vaucouleurs, G. et al. (1991). *Third Reference Catalogue of Bright Galaxies. Volume I: Explanations and references. Volume II: Data for galaxies between 0^h and 12^h. Volume III: Data for galaxies between 12^h and 24^h.*

del Río, M. S., E. Brinks, and J. Cepa (2004). "High-Resolution H I Observations of the Galaxy NGC 404: A Dwarf S0 with Abundant Interstellar Gas". In: *AJ* 128, pp. 89–102. DOI: 10.1086/421358. eprint: astro-ph/0403467.

References

Duc, P.-A. et al. (2015). "The ATLAS 3D project - XXIX. The new look of early-type galaxies and surrounding fields disclosed by extremely deep optical images". In: *MNRAS* 446, pp. 120–143. DOI: 10.1093/mnras/stu2019. arXiv: 1410.0981.

Durbala, A. (2009). "Galaxies in extreme environments: Isolated galaxies versus compact groups". PhD thesis. The University of Alabama.

Durbala, A., J. W. Sulentic, and L. Verdes-Montenegro (2008). "The Interplay between Bulge-Disk-Bar Photometric Measures in the Most Isolated Spiral Galaxies". In: *American Astronomical Society Meeting Abstracts 212*. Vol. 40. Bulletin of the American Astronomical Society, p. 215.

Eggen, O. J., D. Lynden-Bell, and A. Sandage (1962). "Evidence from the motions of old stars that the Galaxy collapsed." In: *ApJ* 136, p. 748. DOI: 10.1086/147433.

Eke, V. R. et al. (2004). "Galaxy groups in the 2dFGRS: the group-finding algorithm and the 2PIGG catalogue". In: *MNRAS* 348, pp. 866–878. DOI: 10.1111/j.1365-2966.2004.07408.x. eprint: astro-ph/0402567.

Erroz-Ferrer, S. et al. (2012). "Hα kinematics of S^{4}G spiral galaxies - I. NGC 864". In: *MNRAS* 427, pp. 2938–2949. DOI: 10.1111/j.1365-2966.2012.21768.x. arXiv: 1208.1409.

Espada, D. et al. (2005). "The large asymmetric HI envelope of the isolated galaxy NGC 864 (CIG 96)". In: *A&A* 442, pp. 455–459. DOI: 10.1051/0004-6361:20052743. eprint: astro-ph/0506769.

Espada, D. et al. (2011a). "Star Formation in the Extended Gaseous Disk of the Isolated Galaxy CIG 96". In: *ApJ* 736, 20, p. 20. DOI: 10.1088/0004-637X/736/1/20. arXiv: 1107.0588.

Espada, D. et al. (2011b). "The AMIGA sample of isolated galaxies. VIII. The rate of asymmetric H i profiles in spiral galaxies". In: *A&A* 532, A117, A117. DOI: 10.1051/0004-6361/201016117. arXiv: 1107.0601.

Ewen, H. I. and E. M. Purcell (1951). "Observation of a Line in the Galactic Radio Spectrum: Radiation from Galactic Hydrogen at 1,420 Mc./sec." In: *Nature* 168, p. 356. DOI: 10.1038/168356a0.

Fernández Lorenzo, M. et al. (2012). "The AMIGA sample of isolated galaxies. X. A first look at isolated galaxy colors". In: *A&A* 540, A47, A47. DOI: 10.1051/0004-6361/201118660. arXiv: 1201.5834.

Fernández Lorenzo, M. et al. (2014). "Are (Pseudo)bulges in Isolated Galaxies Actually Primordial Relics?" In: *ApJ* 788, L39, p. L39. DOI: 10.1088/2041-8205/788/2/L39. arXiv: 1405.3644.

Fernández, X. et al. (2013). "A Pilot for a Very Large Array H I Deep Field". In: *ApJ* 770, L29, p. L29. DOI: 10.1088/2041-8205/770/2/L29. arXiv: 1303.2659.

Fitzpatrick, E. L. (1999). "Correcting for the Effects of Interstellar Extinction". In: *PASP* 111, pp. 63–75. DOI: 10.1086/316293. eprint: astro-ph/9809387.

Fliri, J. and I. Trujillo (2016). "The IAC Stripe 82 Legacy Project: a wide-area survey for faint surface brightness astronomy". In: *MNRAS* 456, pp. 1359–1373. DOI: 10.1093/mnras/stv2686. arXiv: 1603.04474.

Fouqué, P., N. Durand, L. Bottinelli, L. Gouguenheim, and G. Paturel (1990). "An HI survey of late-type galaxies in the Southern Hemisphere. I - The SGC sample". In: *A&AS* 86, pp. 473–502.

Freeman, K. C. (1970). "On the Disks of Spiral and S0 Galaxies". In: *ApJ* 160, p. 811. DOI: 10.1086/150474.

Friesen, R. K. et al. (2017). "The Green Bank Ammonia Survey: First Results of NH3 Mapping of the Gould Belt". In: *ApJ* 843, 63, p. 63. DOI: 10.3847/1538-4357/aa6d58. arXiv: 1704.06318.

Geller, M. J. and J. P. Huchra (1983). "Groups of galaxies. III - The CfA survey". In: *ApJS* 52, pp. 61–87. DOI: 10.1086/190859.

Giese, N., T. van der Hulst, P. Serra, and T. Oosterloo (2016). "Non-parametric estimation of morphological lopsidedness". In: *MNRAS* 461, pp. 1656–1673. DOI: 10.1093/mnras/stw1426. arXiv: 1606.07387.

Giovanelli, R. et al. (2005). "The Arecibo Legacy Fast ALFA Survey. I. Science Goals, Survey Design, and Strategy". In: *AJ* 130, pp. 2598–2612. DOI: 10.1086/497431. eprint: astro-ph/0508301.

Gomes, J. M. et al. (2016). "Spiral-like star-forming patterns in CALIFA early-type galaxies". In: *A&A* 585, A92, A92. DOI: 10.1051/0004-6361/201525974. arXiv: 1511.00744.

Gregory, S. A. and L. A. Thompson (1978). "The Coma/A1367 supercluster and its environs". In: *ApJ* 222, pp. 784–799. DOI: 10.1086/156198.

Grossmann, A. and J. Morlet (1985). In: *Mathematics+Physics, Lecture on recent results, ed. L. Streit (Singapore: World Scientific)*.

Haynes, M. P., L. van Zee, D. E. Hogg, M. S. Roberts, and R. J. Maddalena (1998). "Asymmetry in high-precision global H I profiles of isolated spiral galaxies". In: *AJ* 115, p. 62. DOI: 10.1086/300166.

Hickson, P. (1982). "Systematic properties of compact groups of galaxies". In: *ApJ* 255, pp. 382–391. DOI: 10.1086/159838.

Högbom, J. A. (1974). "Aperture Synthesis with a Non-Regular Distribution of Interferometer Baselines". In: *A&AS* 15, p. 417.

Holmberg, E. (1958). "A photographic photometry of extragalactic nebulae." In: *Meddelanden fran Lunds Astronomiska Observatorium Serie II* 136, p. 1.

Holmes, L. et al. (2015). "The incidence of bar-like kinematic flows in CALIFA galaxies". In: *MNRAS* 451, pp. 4397–4411. DOI: 10.1093/mnras/stv1254. arXiv: 1506.01378.

Holwerda, B. W. et al. (2011a). "Quantified H I morphology - I. Multi-wavelength analysis of the THINGS galaxies". In: *MNRAS* 416, pp. 2401–2414. DOI: 10.1111/j.1365-2966.2011.18938.x. arXiv: 1104.3291.

— (2011b). "Quantified H I morphology - II. Lopsidedness and interaction in WHISP column density maps". In: *MNRAS* 416, pp. 2415–2425. DOI: 10.1111/j.1365-2966.2011.17683.x. arXiv: 1104.3292.

Holwerda, B. W. et al. (2011c). "Quantified H I morphology - III. Merger visibility times from H I in galaxy simulations". In: *MNRAS* 416, pp. 2426–2436. DOI: 10.1111/j.1365-2966.2011.18940.x. arXiv: 1104.3306.

Hubble, E. P. (1926). "Extragalactic nebulae." In: *ApJ* 64. DOI: 10.1086/143018.

— (1936). *Realm of the Nebulae*.

Huchtmeier, W. K. (1994). "Neutral hydrogen observations of elliptical galaxies". In: *A&A* 286, pp. 389–394.

Hughes, D. H. et al. (1998). "High-redshift star formation in the Hubble Deep Field revealed by a submillimetre-wavelength survey". In: *Nature* 394, pp. 241–247. DOI: 10.1038/28328. eprint: astro-ph/9806297.

Hunter, D. A. et al. (2012). "Little Things". In: *AJ* 144, 134, p. 134. DOI: 10.1088/0004-6256/144/5/134. arXiv: 1208.5834.

Hunter, D. A. et al. (2018). "Wide-field Imaging of the Environments of LITTLE THINGS Dwarf Irregular Galaxies". In: *ApJ* 852, 114, p. 114. DOI: 10.3847/1538-4357/aa9feb.

Ilbert, O. et al. (2005). "The VIMOS-VLT deep survey. Evolution of the galaxy luminosity function up to z = 2 in first epoch data". In: *A&A* 439, pp. 863–876. DOI: 10.1051/0004-6361:20041961. eprint: astro-ph/0409134.

Iodice, E. et al. (2017). "The Fornax Deep Survey with VST. II. Fornax A: A Two-phase Assembly Caught in the Act". In: *ApJ* 839, 21, p. 21. DOI: 10.3847/1538-4357/aa6846. arXiv: 1703.07989.

Irwin, J. (1995). "Galaxies and Their Environments". In: *PASP* 107, p. 715. DOI: 10.1086/133613.

Irwin, J. et al. (2012). "Continuum Halos in Nearby Galaxies: An EVLA Survey (CHANG-ES). I. Introduction to the Survey". In: *AJ* 144, 43, p. 43. DOI: 10.1088/0004-6256/144/2/43. arXiv: 1205.5694.

Jarrett, T. H. et al. (2012). "Constructing a WISE High Resolution Galaxy Atlas". In: *AJ* 144, 68, p. 68. DOI: 10.1088/0004-6256/144/2/68. arXiv: 1208.0362.

Jenkins, A. et al. (2001). "The mass function of dark matter haloes". In: *MNRAS* 321, pp. 372–384. DOI: 10.1046/j.1365-8711.2001.04029.x. eprint: astro-ph/0005260.

Jog, C. J. and F. Combes (2009). "Lopsided spiral galaxies". In: *Phys. Rep.* 471, pp. 75–111. DOI: 10.1016/j.physrep.2008.12.002. arXiv: 0811.1101.

Jones, M. G. et al. (2018). "The AMIGA sample of isolated galaxies. XIII. The HI content of an almost "nurture free" sample". In: *A&A* 609, A17, A17. DOI: 10.1051/0004-6361/201731448. arXiv: 1710.03034.

Karachentsev, I. D. (1972). "Catalogue of isolated pairs of galaxies in the northern hemisphere." In: *Soobshcheniya Spetsial'noj Astrofizicheskoj Observatorii* 7.

Karachentseva, V. E. (1973). "The Catalogue of Isolated Galaxies," in: *Astrofizicheskie Issledovaniia Izvestiya Spetsial'noj Astrofizicheskoj Observatorii* 8.

Karachentseva, V. E., I. D. Karachentsev, and A. L. Shcherbanovsky (1979). "Isolated triplets of galaxies. I - List". In: *Astrofizicheskie Issledovaniia Izvestiya Spetsial'noj Astrofizicheskoj Observatorii* 11, pp. 3–39.

Katkov, I. Y., O. K. Sil'chenko, I. V. Chilingarian, R. I. Uklein, and O. V. Egorov (2016). "Stellar counter-rotation in lenticular galaxy NGC 448". In: *MNRAS* 461, pp. 2068–2076. DOI: 10.1093/mnras/stw1452. arXiv: 1606.04862.

Kennicutt Jr., R. C. et al. (2003). "SINGS: The SIRTF Nearby Galaxies Survey". In: *PASP* 115, pp. 928–952. DOI: 10.1086/376941. eprint: astro-ph/0305437.

Kereš, D., N. Katz, D. H. Weinberg, and R. Davé (2005). "How do galaxies get their gas?" In: *MNRAS* 363, pp. 2–28. DOI: 10.1111/j.1365-2966.2005.09451.x. eprint: astro-ph/0407095.

Kerr, F. J. and D. Lynden-Bell (1986). "Review of galactic constants". In: *MNRAS* 221, pp. 1023–1038. DOI: 10.1093/mnras/221.4.1023.

Kleijn, Gijs A. Verdoes et al. (2013). "Monitoring the photometric behavior of Omega-CAM with Astro-WISE". In: *Exper. Astron.* 35, pp. 103–130. DOI: 10.1007/s10686-012-9325-y. arXiv: 1212.6120 [astro-ph.IM].

Klypin, A., I. Karachentsev, D. Makarov, and O. Nasonova (2015). "Abundance of field galaxies". In: *MNRAS* 454, pp. 1798–1810. DOI: 10.1093/mnras/stv2040. arXiv: 1405.4523.

Knapp, G. R., E. L. Turner, and P. E. Cunniffe (1985). "The statistical distribution of the neutral-hydrogen content of elliptical galaxies". In: *AJ* 90, pp. 454–468. DOI: 10.1086/113751.

Kormendy, J. and R. C. Kennicutt Jr. (2004). "Secular Evolution and the Formation of Pseudobulges in Disk Galaxies". In: *ARA&A* 42, pp. 603–683. DOI: 10.1146/annurev.astro.42.053102.134024. eprint: astro-ph/0407343.

Kornreich, D. A., M. P. Haynes, K. P. Jore, and R. V. E. Lovelace (2001). "Asymmetry in Isolated, Morphologically Normal SA Galaxies". In: *AJ* 121, pp. 1358–1368. DOI: 10.1086/319402. eprint: astro-ph/0012432.

Kornreich, D. A., M. P. Haynes, R. V. E. Lovelace, and L. van Zee (2000). "Departures From Axisymmetric Morphology and Dynamics in Spiral Galaxies". In: *AJ* 120, pp. 139–164. DOI: 10.1086/301422. eprint: astro-ph/0004113.

References

Laine, J. et al. (2014). "Morphology and environment of galaxies with disc breaks in the S^{4}G and NIRS0S". In: *MNRAS* 441, pp. 1992–2012. DOI: 10.1093/mnras/stu628. arXiv: 1404.0559.

Lee, J. C., H. S. Hwang, and H. Chung (2018). "A study of environmental effects on galaxy spin using MaNGA data". In: *MNRAS* 477, pp. 1567–1577. DOI: 10.1093/mnras/sty729. arXiv: 1802.10265.

Leon, S., G. Meylan, and F. Combes (2000). "Tidal tails around 20 Galactic globular clusters. Observational evidence for gravitational disk/bulge shocking". In: *A&A* 359, pp. 907–931. eprint: astro-ph/0006100.

Leon, S. and L. Verdes-Montenegro (2003). "Revised positions for CIG galaxies". In: *A&A* 411, pp. 391–395. DOI: 10.1051/0004-6361:20034141. eprint: astro-ph/0310220.

Leon, S. et al. (2008). "The AMIGA sample of isolated galaxies. VI. Radio continuum properties of isolated galaxies: a very radio-quiet sample". In: *A&A* 485, pp. 475–486. DOI: 10.1051/0004-6361:20078533. arXiv: 0804.0132.

Leon, S. et al. (2016). "Anatomy of a blazar in the (sub-)millimeter: ALMA observations of PKS 0521-365". In: *A&A* 586, A70, A70. DOI: 10.1051/0004-6361/201527146. arXiv: 1510.07536.

Levy, R. C. et al. (2018). "The EDGE-CALIFA Survey: Molecular and Ionized Gas Kinematics in Nearby Galaxies". In: *ArXiv e-prints*. arXiv: 1804.05853.

Lin, C. C. and F. H. Shu (1964). "On the Spiral Structure of Disk Galaxies." In: *ApJ* 140, p. 646. DOI: 10.1086/147955.

Lin, L., C. Li, Y. He, T. Xiao, and E. Wang (2017). "Bar-induced Central Star Formation as Revealed by Integral Field Spectroscopy from CALIFA". In: *ApJ* 838, 105, p. 105. DOI: 10.3847/1538-4357/aa657a. arXiv: 1609.05287.

Lisenfeld, U. et al. (2007). "The AMIGA sample of isolated galaxies. III. IRAS data and infrared diagnostics". In: *A&A* 462, pp. 507–523. DOI: 10.1051/0004-6361:20066144. eprint: astro-ph/0610784.

Lisenfeld, U. et al. (2011). "The AMIGA sample of isolated galaxies. IX. Molecular gas properties". In: *A&A* 534, A102, A102. DOI: 10.1051/0004-6361/201117056. arXiv: 1108.2130.

Lisenfeld, U. et al. (2017). "The role of molecular gas in galaxy transition in compact groups". In: *A&A* 607, A110, A110. DOI: 10.1051/0004-6361/201730898. arXiv: 1708.09159.

Little, B. and R. G. Carlberg (1991). "Bar-disc angular momentum exchange". In: *MNRAS* 251, pp. 227–242. DOI: 10.1093/mnras/251.2.227.

Lupton, R (2005). "" In: *http://classic.sdss.org/dr5/algorithms/sdssUBVRITransform.html*.

Madau, P., L. Pozzetti, and M. Dickinson (1998). "The Star Formation History of Field Galaxies". In: *ApJ* 498, pp. 106–116. DOI: 10.1086/305523. eprint: astro-ph/9708220.

Madau, P. et al. (1996). "High-redshift galaxies in the Hubble Deep Field: colour selection and star formation history to z˜4". In: *MNRAS* 283, pp. 1388–1404. DOI: 10.1093/mnras/283.4.1388. eprint: astro-ph/9607172.

Maraston, C. (2005). "Evolutionary population synthesis: models, analysis of the ingredients and application to high-z galaxies". In: *MNRAS* 362, pp. 799–825. DOI: 10.1111/j.1365-2966.2005.09270.x. eprint: astro-ph/0410207.

Marquez, I. and M. Moles (1996). "Effects of the interaction on the properties of spiral galaxies. I. The data." In: *A&AS* 120, pp. 1–34.

Márquez, I. et al. (2002). "Rotation curves and metallicity gradients from HII regions in spiral galaxies". In: *A&A* 393, pp. 389–407. DOI: 10.1051/0004-6361:20021036. eprint: astro-ph/0207020.

Márquez, I. et al. (2003). "The detection of stellar velocity dispersion drops in the central regions of five isolated Seyfert spirals". In: *A&A* 409, pp. 459–467. DOI: 10.1051/0004-6361:20031059. eprint: astro-ph/0306497.

Martin, N. F. et al. (2016). "The PAndAS View of the Andromeda Satellite System. II. Detailed Properties of 23 M31 Dwarf Spheroidal Galaxies". In: *ApJ* 833, 167, p. 167. DOI: 10.3847/1538-4357/833/2/167. arXiv: 1610.01158.

Martin, N. F. et al. (2017). "A Rogues Gallery of Andromeda's Dwarf Galaxies. I. A Predominance of Red Horizontal Branches". In: *ApJ* 850, 16, p. 16. DOI: 10.3847/1538-4357/aa901a. arXiv: 1704.01586.

Martínez-Delgado, D. et al. (2008). "The Ghost of a Dwarf Galaxy: Fossils of the Hierarchical Formation of the Nearby Spiral Galaxy NGC 5907". In: *ApJ* 689, 184-193, pp. 184–193. DOI: 10.1086/592555. arXiv: 0805.1137.

Martínez-Delgado, D. et al. (2009). "Discovery of a Giant Stellar Tidal Stream Around The Disk Galaxy NGC 4013". In: *ApJ* 692, pp. 955–963. DOI: 10.1088/0004-637X/692/2/955. arXiv: 0812.3219.

Martínez-Delgado, D. et al. (2010). "Stellar Tidal Streams in Spiral Galaxies of the Local Volume: A Pilot Survey with Modest Aperture Telescopes". In: *AJ* 140, pp. 962–967. DOI: 10.1088/0004-6256/140/4/962. arXiv: 1003.4860.

Martínez-Delgado, D. et al. (2012). "Dwarfs Gobbling Dwarfs: A Stellar Tidal Stream around NGC 4449 and Hierarchical Galaxy Formation on Small Scales". In: *ApJ* 748, L24, p. L24. DOI: 10.1088/2041-8205/748/2/L24. arXiv: 1112.2154.

Martínez-Delgado, D. et al. (2015). "A Stellar Tidal Stream Around the Whale Galaxy, NGC 4631". In: *AJ* 150, 116, p. 116. DOI: 10.1088/0004-6256/150/4/116. arXiv: 1410.6368.

Martini, P., M. W. Regan, J. S. Mulchaey, and R. W. Pogge (2003). "Circumnuclear Dust in Nearby Active and Inactive Galaxies. I. Data". In: *ApJS* 146, pp. 353–406. DOI: 10.1086/367817. eprint: astro-ph/0212396.

References

Mateus, A., L. Sodré, R. Cid Fernandes, and G. Stasińska (2007). "Semi-empirical analysis of Sloan Digital Sky Survey galaxies - IV. A nature via nurture scenario for galaxy evolution". In: *MNRAS* 374, pp. 1457–1472. DOI: 10.1111/j.1365-2966.2006.11290.x. eprint: astro-ph/0604063.

Matthews, L. D., W. van Driel, and J. S. Gallagher III (1998). "High-Resolution, High Signal-to-Noise, Global H i Spectra of Southern, Extreme Late-Type Spiral Galaxies". In: *AJ* 116, pp. 1169–1185. DOI: 10.1086/300492.

McCracken, H. J. et al. (2012). "UltraVISTA: a new ultra-deep near-infrared survey in COSMOS". In: *A&A* 544, A156, A156. DOI: 10.1051/0004-6361/201219507. arXiv: 1204.6586 [astro-ph.CO].

McDermid, R. M. et al. (2015). "The ATLAS 3D Project - XXX. Star formation histories and stellar population scaling relations of early-type galaxies". In: *MNRAS* 448, pp. 3484–3513. DOI: 10.1093/mnras/stv105. arXiv: 1501.03723.

McGlynn, T. and K. Scollick (1994). "SkyView". In: *Astronomical Data Analysis Software and Systems III*. Ed. by D. R. Crabtree, R. J. Hanisch, and J. Barnes. Vol. 61. Astronomical Society of the Pacific Conference Series, p. 34.

McMullin, J. P., B. Waters, D. Schiebel, W. Young, and K. Golap (2007). "CASA Architecture and Applications". In: *Astronomical Data Analysis Software and Systems XVI*. Ed. by R. A. Shaw, F. Hill, and D. J. Bell. Vol. 376. Astronomical Society of the Pacific Conference Series, p. 127.

Merritt, A. et al. (2016). "The Dragonfly Nearby Galaxies Survey. II. Ultra-Diffuse Galaxies near the Elliptical Galaxy NGC 5485". In: *ApJ* 833, 168, p. 168. DOI: 10.3847/1538-4357/833/2/168. arXiv: 1610.01609.

Miville-Deschênes, M.-A. et al. (2016). "Probing interstellar turbulence in cirrus with deep optical imaging: no sign of energy dissipation at 0.01 pc scale". In: *A&A* 593, A4, A4. DOI: 10.1051/0004-6361/201628503. arXiv: 1605.08360.

Muldrew, S. I. et al. (2012). "Measures of galaxy environment - I. What is 'environment'?" In: *MNRAS* 419, pp. 2670–2682. DOI: 10.1111/j.1365-2966.2011.19922.x. arXiv: 1109.6328.

Myers, S. T., S. A. Baum, and C. J. Chandler (2014). "The Karl G. Jansky Very Large Array Sky Survey (VLASS)". In: *American Astronomical Society Meeting Abstracts #223*. Vol. 223. American Astronomical Society Meeting Abstracts, p. 236.01.

Nair, P. B. and R. G. Abraham (2010). "A Catalog of Detailed Visual Morphological Classifications for 14,034 Galaxies in the Sloan Digital Sky Survey". In: *ApJS* 186, pp. 427–456. DOI: 10.1088/0067-0049/186/2/427. arXiv: 1001.2401.

Neugebauer, G. et al. (1984). "The Infrared Astronomical Satellite (IRAS) mission". In: *ApJ* 278, pp. L1–L6. DOI: 10.1086/184209.

Niemi, S.-M. (2011). "Properties of Galaxies and Groups: Nature versus Nurture". PhD thesis. PhD Thesis, 2011.

Oesch, P. A. et al. (2016). "A Remarkably Luminous Galaxy at z=11.1 Measured with Hubble Space Telescope Grism Spectroscopy". In: *ApJ* 819, 129, p. 129. DOI: 10.3847/0004-637X/819/2/129. arXiv: 1603.00461.

Palumbo, G. G. C., P. Saracco, P. Hickson, and C. Mendes de Oliveira (1995). "Environment of compact groups of galaxies". In: *AJ* 109, pp. 1476–1484. DOI: 10.1086/117377.

Peebles, P. J. E. (1969). "Origin of the Angular Momentum of Galaxies". In: *ApJ* 155, p. 393. DOI: 10.1086/149876.

Peñarrubia, J. et al. (2005). "A Comprehensive Model for the Monoceros Tidal Stream". In: *ApJ* 626, pp. 128–144. DOI: 10.1086/429903. eprint: astro-ph/0410448.

Peng, C. Y., L. C. Ho, C. D. Impey, and H.-W. Rix (2010). "Detailed Decomposition of Galaxy Images. II. Beyond Axisymmetric Models". In: *AJ* 139, pp. 2097–2129. DOI: 10.1088/0004-6256/139/6/2097. arXiv: 0912.0731.

Perez-Torres, M.A. et al. (2015). *The Spanish Square Kilometre Array White Book*. Sociedad Española de Astronomía, p. 289.

Phillips, A. C. et al. (1997). "The Nature of Compact Galaxies in the Hubble Deep Field. I. Global Properties1," in: *ApJ* 489, pp. 543–558. DOI: 10.1086/304796.

Pilbratt, G. L. (2003). "Herschel Space Observatory mission overview". In: *IR Space Telescopes and Instruments*. Ed. by J. C. Mather. Vol. 4850. Proc. SPIE, pp. 586–597. DOI: 10.1117/12.461767.

Pisano, D. J., E. M. Wilcots, and C. T. Liu (2002). "An H I/Optical Atlas of Isolated Galaxies". In: *ApJS* 142, pp. 161–222. DOI: 10.1086/341787.

Planck Collaboration et al. (2014). "Planck 2013 results. I. Overview of products and scientific results". In: *A&A* 571, A1, A1. DOI: 10.1051/0004-6361/201321529. arXiv: 1303.5062.

Planck Collaboration et al. (2016). "Planck 2015 results. XIII. Cosmological parameters". In: *A&A* 594, A13, A13. DOI: 10.1051/0004-6361/201525830. arXiv: 1502.01589.

Pohlen, M., R.-J. Dettmar, R. Lütticke, and G. Aronica (2002). "Outer edges of face-on spiral galaxies. Deep optical imaging of NGC 5923, UGC 9837 and NGC 5434". In: *A&A* 392, pp. 807–816. DOI: 10.1051/0004-6361:20020994.

Portas, A. et al. (2011). "H I Asymmetries in the Isolated Galaxy CIG 292". In: *ApJ* 739, L27, p. L27. DOI: 10.1088/2041-8205/739/1/L27. arXiv: 1106.5976.

Prada, F. et al. (2003). "Observing the Dark Matter Density Profile of Isolated Galaxies". In: *ApJ* 598, pp. 260–271. DOI: 10.1086/378669. eprint: astro-ph/0301360.

Reichard, T. A., T. M. Heckman, G. Rudnick, J. Brinchmann, and G. Kauffmann (2008). "The Lopsidedness of Present-Day Galaxies: Results from the Sloan Digital Sky Survey". In: *ApJ* 677, 186-200, pp. 186–200. DOI: 10.1086/526506. arXiv: 0710.0589.

Reichard, T. A. et al. (2009). "The Lopsidedness of Present-Day Galaxies: Connections to the Formation of Stars, the Chemical Evolution of Galaxies, and the Growth of Black Holes". In: *ApJ* 691, pp. 1005–1020. DOI: 10.1088/0004-637X/691/2/1005. arXiv: 0809.3310.

Richter, O.-G. and R. Sancisi (1994). "Asymmetries in disk galaxies. How often? How strong?" In: *A&A* 290.

Rix, H.-W. and D. Zaritsky (1995). "Nonaxisymmetric Structures in the Stellar Disks of Galaxies". In: *ApJ* 447, p. 82. DOI: 10.1086/175858. eprint: astro-ph/9505111.

Roberts, M. S. (1962). "The neutral hydrogen content of late-type spiral galaxies." In: *AJ* 67, pp. 437–446. DOI: 10.1086/108752.

— (1975). "Radio Observations of Neutral Hydrogen in Galaxies". In: *Galaxies and the Universe*. Ed. by A. Sandage, M. Sandage, and J. Kristian. the University of Chicago Press, p. 309.

Sabater, J., L. Verdes-Montenegro, S. Leon, P. Best, and J. Sulentic (2012). "The AMIGA sample of isolated galaxies. XI. Optical characterisation of nuclear activity". In: *A&A* 545, A15, A15. DOI: 10.1051/0004-6361/201118692. arXiv: 1205.6825 [astro-ph.CO].

Sabater, J. et al. (2008). "The AMIGA sample of isolated galaxies. VII. Far-infrared and radio continuum study of nuclear activity". In: *A&A* 486, pp. 73–83. DOI: 10.1051/0004-6361:20078785. arXiv: 0803.0335.

Salmon, B. et al. (2018). "RELICS: A Candidate Galaxy Arc at z˜10 and Other Brightly Lensed z>6 Galaxies". In: *American Astronomical Society Meeting Abstracts 231*. Vol. 231. American Astronomical Society Meeting Abstracts, p. 454.12.

Sánchez, S. F. et al. (2012). "CALIFA, the Calar Alto Legacy Integral Field Area survey. I. Survey presentation". In: *A&A* 538, A8, A8. DOI: 10.1051/0004-6361/201117353. arXiv: 1111.0962.

Sancisi, R. (1976). "Warped HI Disks in Galaxies". In: *A&A* 53, p. 159.

Sandage, A. (1961). *The Hubble Atlas of Galaxies*.

— (1976). "High-latitude reflection nebulosities illuminated by the galactic plane". In: *AJ* 81, p. 954. DOI: 10.1086/111975.

Sandage, A., M. Sandage, and J. Kristian (1975). *Galaxies and the Universe*.

Savage, B. D. and J. S. Mathis (1979). "Observed properties of interstellar dust". In: *ARA&A* 17, pp. 73–111. DOI: 10.1146/annurev.aa.17.090179.000445.

Schawinski, K. et al. (2009). "Do Moderate-Luminosity Active Galactic Nuclei Suppress Star Formation?" In: *ApJ* 692, pp. L19–L23. DOI: 10.1088/0004-637X/692/1/L19. arXiv: 0901.1663 [astro-ph.GA].

Schommer, R. A. and W. T. Sullivan III (1976). "Do the ring-like structures in the galaxy NGC 4736 represent Lindblad resonances". In: *Astrophys. Lett.* 17, pp. 191–196.

Schwarz, M. P. (1981). "The response of gas in a galactic disk to bar forcing". In: *ApJ* 247, pp. 77–88. DOI: 10.1086/159011.

Scott, N. et al. (2013). "The ATLAS 3D project - XXI. Correlations between gradients of local escape velocity and stellar populations in early-type galaxies". In: *MNRAS* 432, pp. 1894–1913. DOI: 10.1093/mnras/sts422. arXiv: 1211.4615.

Scott, T. C. et al. (2014). "A ˜ 12 kpc H i extension and other H i asymmetries in the isolated galaxy CIG 340 (IC 2487)". In: *A&A* 567, A56, A56. DOI: 10.1051/0004-6361/201423701. arXiv: 1405.2594.

Sellwood, J. A. and J. J. Binney (2002). "Radial mixing in galactic discs". In: *MNRAS* 336, pp. 785–796. DOI: 10.1046/j.1365-8711.2002.05806.x. eprint: astro-ph/0203510.

Sengupta, C. et al. (2012). "H I asymmetry in the isolated galaxy CIG 85 (UGC 1547)". In: *A&A* 546, A95, A95. DOI: 10.1051/0004-6361/201219948. arXiv: 1209.0786.

Serra, P. et al. (2010). "Early-type Galaxies in Isolation: an HI Perspective with ATLAS 3D". In: *Galaxies in Isolation: Exploring Nature Versus Nurture*. Ed. by L. Verdes-Montenegro, A. Del Olmo, and J. Sulentic. Vol. 421. Astronomical Society of the Pacific Conference Series, p. 49.

Serra, P. et al. (2012). "The ATLAS 3D project - XIII. Mass and morphology of H I in early-type galaxies as a function of environment". In: *MNRAS* 422, pp. 1835–1862. DOI: 10.1111/j.1365-2966.2012.20219.x. arXiv: 1111.4241 [astro-ph.CO].

Serra, P. et al. (2014). "The ATLAS 3D project - XXVI. H I discs in real and simulated fast and slow rotators". In: *MNRAS* 444, pp. 3388–3407. DOI: 10.1093/mnras/stt2496. arXiv: 1401.3180.

Shapley, A. E. (2011). "Physical Properties of Galaxies from z = 2-4". In: *ARA&A* 49, pp. 525–580. DOI: 10.1146/annurev-astro-081710-102542. arXiv: 1107.5060.

Sheth, K. et al. (2010). "The Spitzer Survey of Stellar Structure in Galaxies (S4G)". In: *PASP* 122, p. 1397. DOI: 10.1086/657638. arXiv: 1010.1592.

Silva, D. R. and G. D. Bothun (1998). "The Ages of Disturbed Field Elliptical Galaxies. I. Global Properties". In: *AJ* 116, pp. 85–101. DOI: 10.1086/300394.

Skrutskie, M. F. et al. (1997). "The Two Micron All Sky Survey (2MASS): Overview and Status." In: *The Impact of Large Scale Near-IR Sky Surveys*. Ed. by F. Garzon, N. Epchtein, A. Omont, B. Burton, and P. Persi. Vol. 210. Astrophysics and Space Science Library, p. 25. DOI: 10.1007/978-94-011-5784-1_4.

Smith, B. J., M. L. Giroux, C. Struck, and M. Hancock (2010). "Spirals, Bridges, and Tails: A Galaxy Evolution Explorer Ultraviolet Atlas of Interacting Galaxies". In: *AJ* 139, pp. 1212–1241. DOI: 10.1088/0004-6256/139/3/1212.

References

Spector, O. and N. Brosch (2016). "Extremely isolated galaxies - I. Sample and simulation analysis". In: *MNRAS* 456, pp. 885–908. DOI: 10.1093/mnras/stv2662. arXiv: 1601.00964.

Springel, V. et al. (2005). "Simulations of the formation, evolution and clustering of galaxies and quasars". In: *Nature* 435, pp. 629–636. DOI: 10.1038/nature03597. eprint: astro-ph/0504097.

Springob, C. M., M. P. Haynes, R. Giovanelli, and B. R. Kent (2005). "A Digital Archive of H I 21 Centimeter Line Spectra of Optically Targeted Galaxies". In: *ApJS* 160, pp. 149–162. DOI: 10.1086/431550. eprint: astro-ph/0505025.

Stoughton, C. et al. (2002). "Sloan Digital Sky Survey: Early Data Release". In: *AJ* 123, pp. 485–548. DOI: 10.1086/324741.

Strateva, I. et al. (2001). "Color Separation of Galaxy Types in the Sloan Digital Sky Survey Imaging Data". In: *AJ* 122, pp. 1861–1874. DOI: 10.1086/323301. eprint: astro-ph/0107201.

Sulentic, J. W. et al. (2006). "The AMIGA sample of isolated galaxies. II. Morphological refinement". In: *A&A* 449, pp. 937–949. DOI: 10.1051/0004-6361:20054020. eprint: astro-ph/0511652.

Tacconi, L. J. et al. (2013). "Phibss: Molecular Gas Content and Scaling Relations in z ˜ 1-3 Massive, Main-sequence Star-forming Galaxies". In: *ApJ* 768, 74, p. 74. DOI: 10.1088/0004-637X/768/1/74. arXiv: 1211.5743.

Tapia, T. et al. (2017). "Formation of S0 galaxies through mergers. Evolution in the Tully-Fisher relation since z $\sim$ 1". In: *A&A* 604, A105, A105. DOI: 10.1051/0004-6361/201628821. arXiv: 1706.03803.

Terrón, V. and M. Fernández (2011). "LEMON: an (almost) completely automated differential-photometry pipeline". In: *Highlights of Spanish Astrophysics VI*. Ed. by M. R. Zapatero Osorio, J. Gorgas, J. Maíz Apellániz, J. R. Pardo, and A. Gil de Paz, pp. 755–761.

The Dark Energy Survey Collaboration (2005). "The Dark Energy Survey". In: *ArXiv Astrophysics e-prints*. eprint: astro-ph/0510346.

Thilker, D. A. et al. (2010). "NGC 404: A Rejuvenated Lenticular Galaxy on a Merger-induced, Blueward Excursion Into the Green Valley". In: *ApJ* 714, pp. L171–L175. DOI: 10.1088/2041-8205/714/1/L171. arXiv: 1003.4985.

Tifft, W. G. and W. K. Huchtmeier (1990). "Comparisons between 21 CM data from Effelsberg and Greenbank". In: *A&AS* 84, pp. 47–58.

Trujillo, I. and J. Fliri (2016). "Beyond 31 mag arcsec-2: The Frontier of Low Surface Brightness Imaging with the Largest Optical Telescopes". In: *ApJ* 823, 123, p. 123. DOI: 10.3847/0004-637X/823/2/123. arXiv: 1510.04696.

Trujillo, I., J. Roman, M. Filho, and J. Sánchez Almeida (2017). "The Nearest Ultra Diffuse Galaxy: UGC 2162". In: *ApJ* 836, 191, p. 191. DOI: 10.3847/1538-4357/aa5cbb. arXiv: 1701.03804.

Turner, E. L. and J. R. Gott III (1975). "Evidence for a spatially homogeneous component of the universe - Single galaxies". In: *ApJ* 197, pp. L89–L93. DOI: 10.1086/181785.

Ulvestad, J. S. and L. C. Ho (2002). "A Search for Active Galactic Nuclei in Sc Galaxies with H II Spectra". In: *ApJ* 581, pp. 925–931. DOI: 10.1086/344442. eprint: astro-ph/0208460.

Valentijn, E. A. et al. (2007). "Astro-WISE: Chaining to the Universe". In: *Astronomical Data Analysis Software and Systems XVI*. Ed. by R. A. Shaw, F. Hill, and D. J. Bell. Vol. 376. Astronomical Society of the Pacific Conference Series, p. 491. eprint: astro-ph/0702189.

van Dokkum, P. G. (2005). "The Recent and Continuing Assembly of Field Elliptical Galaxies by Red Mergers". In: *AJ* 130, pp. 2647–2665. DOI: 10.1086/497593. eprint: astro-ph/0506661.

van Dokkum, P. G. et al. (2008). "Confirmation of the Remarkable Compactness of Massive Quiescent Galaxies at z ~ 2.3: Early-Type Galaxies Did not Form in a Simple Monolithic Collapse". In: *ApJ* 677, L5, p. L5. DOI: 10.1086/587874. arXiv: 0802.4094.

van Dokkum, P. G. et al. (2015). "Forty-seven Milky Way-sized, Extremely Diffuse Galaxies in the Coma Cluster". In: *ApJ* 798, L45, p. L45. DOI: 10.1088/2041-8205/798/2/L45. arXiv: 1410.8141.

van Dokkum, P. et al. (2016). "A High Stellar Velocity Dispersion and 100 Globular Clusters for the Ultra-diffuse Galaxy Dragonfly 44". In: *ApJ* 828, L6, p. L6. DOI: 10.3847/2041-8205/828/1/L6. arXiv: 1606.06291.

Varela, J. et al. (2004). "Properties of isolated disk galaxies". In: *A&A* 420, pp. 873–879. DOI: 10.1051/0004-6361:20035697. eprint: astro-ph/0403146.

Venhola, A. et al. (2017). "The Fornax Deep Survey with VST. III. Low surface brightness dwarfs and ultra diffuse galaxies in the center of the Fornax cluster". In: *A&A* 608, A142, A142. DOI: 10.1051/0004-6361/201730696. arXiv: 1710.04616.

Verdes-Montenegro, L., A. Bosma, and E. Athanassoula (1995). "The three rings of the isolated galaxy NGC 7217." In: *A&A* 300, p. 65.

Verdes-Montenegro, L. et al. (2001). "Where is the neutral atomic gas in Hickson groups?" In: *A&A* 377, pp. 812–826. DOI: 10.1051/0004-6361:20011127. eprint: astro-ph/0108223.

Verdes-Montenegro, L. et al. (2005). "The AMIGA project. I. Optical characterization of the CIG catalog". In: *A&A* 436, pp. 443–455. DOI: 10.1051/0004-6361:20042280. eprint: astro-ph/0504201.

Verley, S. (2005). "Environmental quantification and Halpha characterisation of the most isolated galaxies in the local Universe". PhD thesis. Universidad de Granada.

Verley, S., F. Combes, L. Verdes-Montenegro, G. Bergond, and S. Leon (2007a). "Star formation in isolated AMIGA galaxies: dynamical influence of bars". In: *A&A* 474, pp. 43–53. DOI: 10.1051/0004-6361:20077650. arXiv: 0707.4127.

Verley, S. et al. (2007b). "The AMIGA sample of isolated galaxies. IV. A catalogue of neighbours around isolated galaxies". In: *A&A* 470, pp. 505–513. DOI: 10.1051/0004-6361:20077307. arXiv: 0705.0479.

Verley, S. et al. (2007c). "The AMIGA sample of isolated galaxies. V. Quantification of the isolation". In: *A&A* 472, pp. 121–130. DOI: 10.1051/0004-6361:20077481. arXiv: 0706.2555.

Vettolani, G., R. de Souza, and G. Chincarini (1986). "Isolated galaxies". In: *A&A* 154, pp. 343–348.

Wakker, B. P. et al. (1999). "Accretion of low-metallicity gas by the Milky Way". In: *Nature* 402, pp. 388–390. DOI: 10.1038/46498.

Walker, L. M. et al. (2013). "The Optical Green Valley versus Mid-infrared Canyon in Compact Groups". In: *ApJ* 775, 129, p. 129. DOI: 10.1088/0004-637X/775/2/129. arXiv: 1307.6559.

Walter, F. et al. (2008). "THINGS: The H I Nearby Galaxy Survey". In: *AJ* 136, pp. 2563–2647. DOI: 10.1088/0004-6256/136/6/2563. arXiv: 0810.2125.

Werner, M. W. et al. (2004). "The Spitzer Space Telescope Mission". In: *ApJS* 154, pp. 1–9. DOI: 10.1086/422992. eprint: astro-ph/0406223.

White, S. D. M. (1983). "Astronomy: Galactic irregularities - nature or nurture". In: *Nature* 302, p. 756. DOI: 10.1038/302756a0.

White, S. D. M. and M. J. Rees (1978). "Core condensation in heavy halos - A two-stage theory for galaxy formation and clustering". In: *MNRAS* 183, pp. 341–358. DOI: 10.1093/mnras/183.3.341.

Williams, R. E. et al. (1996). "The Hubble Deep Field: Observations, Data Reduction, and Galaxy Photometry". In: *AJ* 112, p. 1335. DOI: 10.1086/118105. eprint: astro-ph/9607174.

Winkel, B. et al. (2016). "The Effelsberg-Bonn H I Survey: Milky Way gas. First data release". In: *A&A* 585, A41, A41. DOI: 10.1051/0004-6361/201527007. arXiv: 1512.05348 [astro-ph.IM].

York, D. G. et al. (2000). "The Sloan Digital Sky Survey: Technical Summary". In: *AJ* 120, pp. 1579–1587. DOI: 10.1086/301513. eprint: astro-ph/0006396.

Zaritsky, D. and H.-W. Rix (1997). "Lopsided Spiral Galaxies and a Limit on the Galaxy Accretion Rate". In: *ApJ* 477, pp. 118–127. DOI: 10.1086/303692. eprint: astro-ph/9608086.

Zaritsky, D., R. Smith, C. Frenk, and S. D. M. White (1993). "Satellites of spiral galaxies". In: *ApJ* 405, pp. 464–478. DOI: 10.1086/172379.

Zhang, J., R. Abraham, P. van Dokkum, A. Merritt, and S. Janssens (2018). "The Dragonfly Nearby Galaxies Survey. IV. A Giant Stellar Disk in NGC 2841". In: *ApJ* 855, 78, p. 78. DOI: 10.3847/1538-4357/aaac81. arXiv: 1802.02583.

Zwicky, F., E. Herzog, P. Wild, M. Karpowicz, and C. T. Kowal (1961). *Catalogue of galaxies and of clusters of galaxies, Vol. I.*

Appendix A

Sample calibration and imaging script for HI data

On the reproducibility of the results and figures of this dissertation

With the aim of making the results and images presented in this thesis as accessible and reproducible as possible, we have created a GitHub repository named AMIGA deep-obs (release v0) (with doi:10.5281/zenodo.1295480) that contains the following scripts:

- all the files corresponding to the calibration and imaging of the VLA and EVLA data − Python v2.7, CASA software ready
- the observing blocks submitted to the VST telescope − text files, p2pp tool ready
- the reduction and calibration scripts used in the Astro-WISE pipeline to reduce and calibrate the VST data − in Python v3.0, Astro-WISE pipeline ready
- the scripts used to produce all the images and figures shown in the current dissertation − Python v2.7, iPython Notebook ready.

Sample calibration and imaging script for HI data

As described in Sect. 3.1, the calibration and imaging of the different measurements sets (MS) of CIG 96 was done with CASA software. The following is a sample calibration script (for the second MS taken on the 29^th of July, 2013) that includes the inspection of the MS, correction of the position of the antennas, flagging of defective data, selection of the reference antenna, delays correction, flux density calculation, bandpass, phase and amplitude calibrations, regridding and splitting of the HI line, $uv-$continuum subtraction, and imaging of the data into a datacube. In total, we performed the calibration of 13 MS from EVLA and 2 from VLA, that were combined into the final HI datacube used in the analysis (see Sect. 4.1).

```
# -*- coding: iso-8859-1 -*-
### EVLA DATA REDUCTION
### Project: 13A-341
### Dataset date: 29jul13b
### Original dataset name: 13A-341.sb24028522.eb24167588
    .56502.374954375.ms
### Renamed as: cig96_13.ms
###
### Configuration: C (8/10)

### Import of EVLA data from SDM format:
##########################################
# Original data file gets now CASA format and a new name: "cig96_13.ms"
importevla(asdm='cig96_13', vis='cig96_13.ms')

### Listobs inspection:
#######################
listobs(vis='cig96_13.ms')

### Data inspection via plotms:
###############################
# Prior to anything else, there is dummy scan, field=0, so we remove it:
flagdata(vis='cig96_13.ms', mode='manual', field='0')
# We run plotms to inspect the general aspect of the data:
plotms(vis='cig96_13.ms',xaxis='channel',yaxis='amp',field='1',spw='0',
    coloraxis='field',avgtime='1e9')
```

```
25 plotms(vis='cig96_13.ms',xaxis='time',yaxis='amp',field='1',spw='0',
       coloraxis='field',avgchannel='1e9')
26
27 # Antenna position correction:
28 ##############################
29 gencal(vis='cig96_13.ms', caltable='cig96_13.ms.antpos', caltype='antpos
       ')
30
31 ### Plot with the spatial distribution of the antennae:
32 ########################################################
33 plotants(vis='cig96_13.ms',figfile='cig96_13.ms.plotants.png')
34
35 ### Flagging:
36 #############
37 # Log file provides with some insight of the antennae status, corruption
       , etc.:
38 flagdata(vis='cig96_13.ms', mode='manual', field='', antenna='ea19',
       flagbackup=True)
39 ### Shadowing correction over the whole .ms:
40 flagdata(vis='cig96_13.ms', mode='shadow', flagbackup=True)
41 ### Zero clipping correction over the whole .ms:
42 flagdata(vis='cig96_13.ms', mode='clip', clipzeros=True, flagbackup=True
       )
43 ### Field 1 (bandpass and flux calibrator): quacking of the first 30
       seconds (all antennas showing low amplitudes):
44 flagdata(vis='cig96_13.ms', mode='quack', field='1', quackinterval=30.0,
        quackmode='beg')
45 # bad antennas:
46 flagdata(vis='cig96_13.ms', mode='manual', scan='2', antenna='3&5',
       correlation='LL', flagbackup=True)
47 # there is a baseline, 5&15 in LL correllation, that shows a higher Amp
       in Amp vs channel plot, we remove it:
48 flagdata(vis='cig96_13.ms', mode='manual', scan='2', antenna='5&15',
       correlation='LL', flagbackup=True)
49 # Quacking needed:
50 flagdata(vis='cig96_13.ms', mode='quack', field='2', quackinterval=5.0,
       quackmode='beg')
51 # bad antennas: baseline 3&5 always shows the highest amplitudes in LL
       pol., quite above the average values of 0.015 in Amp
```

```
52 flagdata(vis='cig96_13.ms', mode='manual', field='2', antenna='3&5',
       correlation='LL', flagbackup=True)
53 # it has the RFI in channel ~350:
54 flagdata(vis='cig96_13.ms', mode='manual', field='2', spw = '0:330~380')
55 # and a small one in ~1250:
56 flagdata(vis='cig96_13.ms', mode='manual', field='2', antenna='4&8', spw
       = '0:1253')
57 # and the MW HI emission in ~1960:
58 flagdata(vis='cig96_13.ms', mode='manual', field='2', spw = '0:1940~1975
       ')
59 ### Field 3 (CIG96) flagging:
60 # quacking of the first 10 seconds of the rest of the scans:
61 flagdata(vis='cig96_13.ms', mode='quack', field='3', quackinterval=10.0,
        quackmode='beg')
62 # same RFI in ~350 and MW emission as in field 2; no RFI in ~1250:
63 flagdata(vis='cig96_13.ms', mode='manual', field='3', spw = '0:330~380')
64 flagdata(vis='cig96_13.ms', mode='manual', field='3', spw = '0:1940~1975
       ')
65
66 ### Reference antenna selection:
67 ##################################
68 # After checking plotants, we select this one because it is quite
       central:
69 refant='ea10'
70
71 ### Opacity and gaincurve corrections:
72 ########################################
73 # No opacity or gaincurve correction needed.
74
75 ### Delays correction:
76 ######################
77 # Prior to the bandpass correction, we need to correct the phase
       variations with time (they are large). We use the bandpass calibrator
        in field 1 with the antenna position correction table:
78 gaincal(vis='cig96_13.ms', caltable='cig96_13.ms.delays', field='1',
       refant='ea10', gaintype='K', gaintable=['cig96_13.ms.antpos'])
79
80 ### Flux density:
81 #################
82 # First, we check the list of available models:
```

```
83 setjy(vis='cig96_13.ms', listmodels=T)
84 # The model chosen has to be in accordance with the calibrator and band
       selected: 3C48 in L band:
85 setjy(vis='cig96_13.ms', field='1', modimage='/mnt/scops/data/data/
       paramimo/casapy-42.2.30986-1-64b/data/nrao/VLA/CalModels/3C48_L.im')
86
87 ### Bandpass calibration:
88 ##########################
89 # For the bandpass and flux (field=1) and phase (field=2) calibrators we
       use solution interval time of solint='5s':
90 gaincal(vis='cig96_13.ms', caltable='cig96_13.ms.bpphase5s', field='1',
       refant='ea10', calmode='p', solint='5s', minsnr=5.0, gaintable=['
       cig96_13.ms.antpos', 'cig96_13.ms.delays'])
91
92 # The solution interval of 5 seconds has been calculated following with
       the VLA exp.time
93 # calculator using the parameters:
94 #
95 # Freq. = 1.42 GHz
96 # Medium elevation (summer time)
97 # Bandwith freq. = 16 MHz (see listobs)
98 # RMS noise = 1.5 mJy
99 #
100 # The calculator estimates less than one second (0.2s) is enough to get
       such SNR or even higher
101 # so we set solint=5s since 5s is the shortest integration time of our
       data. This should mean that # there should be a solution for all the
       intervals.
102
103 # We see the phase VS time figures to see that the phase is now waaayyy
       flatter:
104 plotcal(caltable='cig96_13.ms.bpphase5s', xaxis='time', yaxis='phase')
105
106 # Apply phase solutions on the fly:
107 bandpass(vis='cig96_13.ms', caltable='cig96_13.ms.bandpass5s', field='1'
       , refant='ea10', solint='inf', solnorm=T, minsnr=3.0, minblperant=3,
       gaintable=['cig96_13.ms.bpphase5s', 'cig96_13.ms.antpos', 'cig96_13.
       ms.delays'], interp=['nearest'])
108
109 # We check again the solutions:
```

```
110 plotcal(caltable='cig96_13.ms.bpphase5s', field='1', xaxis='time', yaxis
    ='phase')
111 # Difference in phase is less, phase shows a flatter behaviour now.
112
113 ### Phase and amplitude calibration:
114 ####################################
115 # Phase calibration for the calibrators, fields 1 and 2 (spw 0, where
    the line is):
116 gaincal(vis='cig96_13.ms',caltable='cig96_13.ms.intphase', field='1,2',
    refant='ea10', calmode='p', solint='5s', minsnr=5.0, gaintable=['
    cig96_13.ms.antpos', 'cig96_13.ms.delays', 'cig96_13.ms.bandpass5s'])
117 # We create another calibration table, using solint='inf', i.e., finding
     one solution over the whole scan, to use FOR THE TARGET later on:
118 gaincal(vis='cig96_13.ms', caltable='cig96_13.ms.scanphase', field='1,2'
    , refant='ea10', calmode='p', solint='inf', minsnr=5.0, gaintable=['
    cig96_13.ms.antpos', 'cig96_13.ms.delays', 'cig96_13.ms.bandpass5s'])
119 # Derive amplitude solutions:
120 gaincal(vis='cig96_13.ms', caltable='cig96_13.ms.amp', field='1',
    refant='ea10', calmode='ap', solint='inf', minsnr=5.0, gaintable=['
    cig96_13.ms.antpos', 'cig96_13.ms.delays', 'cig96_13.ms.bandpass5s',
    'cig96_13.ms.intphase'], gainfield=['','','','1'],append=True)
121 gaincal(vis='cig96_13.ms', caltable='cig96_13.ms.amp', field='2',
    refant='ea10', calmode='ap', solint='inf', minsnr=5.0, gaintable=['
    cig96_13.ms.antpos', 'cig96_13.ms.delays', 'cig96_13.ms.bandpass5s',
    'cig96_13.ms.intphase'], gainfield=['','','','2'],append=True)
122
123 # Now I derive the flux for the rest of the sources. Note that the flux
    table REPLACES the amp.gcal in terms of future application of the
    calibration to the data, (i.e., it's not an incremental table) UNLESS
     we set incremental=T (as of CASA 4.0):
124 myflux = fluxscale(vis='cig96_13.ms', caltable='cig96_13.ms.amp',
    fluxtable='cig96_13.ms.flux', reference='1', transfer='2',
    incremental=False)
125
126 ### Application of the calibration to the .ms file:
127 ###################################################
128 applycal(vis='cig96_13.ms', field='1', gaintable=['cig96_13.ms.antpos',
    'cig96_13.ms.delays', 'cig96_13.ms.bandpass5s', 'cig96_13.ms.intphase
    ', 'cig96_13.ms.flux'], gainfield=['','','','1',''], calwt=F)
```

```
129 applycal(vis='cig96_13.ms', field='2', gaintable=['cig96_13.ms.antpos',
        'cig96_13.ms.delays', 'cig96_13.ms.bandpass5s', 'cig96_13.ms.intphase
        ', 'cig96_13.ms.flux'], gainfield=['','','','2',''], calwt=F)
130 applycal(vis='cig96_13.ms', field='3', gaintable=['cig96_13.ms.antpos',
        'cig96_13.ms.delays', 'cig96_13.ms.bandpass5s', 'cig96_13.ms.
        scanphase', 'cig96_13.ms.flux'], gainfield=['','','','2',''], calwt=F
        )
131
132 ### Regridding of the .ms to a new frame:
133 ##########################################
134 cvel(vis='cig96_13.ms', outputvis='cig96_13.ms.cvel', mode='velocity',
        field='', spw='0', restfreq='1.42040575177GHz', outframe='LSRK',
        veltype='radio')
135
136 ### Splitting of CIG96:
137 ########################
138 # Splitting of field = 3 (CIG96) calibrated data, in the spw=0:
139 split(vis='cig96_13.ms.cvel', datacolumn='corrected', outputvis='
        cig96_13.cvel.corr.ms', field='3', spw='0:400~1700')
140 # Split of the whole spw:
141 split(vis='cig96_13.ms', datacolumn='corrected', outputvis='cig96_13.
        corr.spw0.ms', field='3', spw='0')
142 # Emission in the higher frequency: the emission line is seen in 1.4203
        GHz. We split the fields in spw=0 from channel 780 to 1600:
143 split(vis='cig96_13.ms', datacolumn='corrected', outputvis='cig96_13.
        corr.emission.ms', field='3', spw='0:780~1600')
144 # Splitting CIG96 fields in spw=0 with time binning of 20s and channel
        width of 10 channels:
145 split(vis='cig96_13.ms.cvel', datacolumn='corrected', outputvis='
        cig96_13.corr.20s.10chan.ms', width=10, timebin='20s', field='3', spw
        ='0:451~1700')
146
147 ### UV continuum subtraction:
148 ##############################
149 uvcontsub(vis='cig96_13.cvel.corr.ms', field='0', fitspw='
        0:50~350;900~1050', fitorder=1)
150 uvcontsub(vis='cig96_13.corr.20s.10chan.ms', field='0', fitspw='
        0:15~30;90~105', fitorder=1)
151 # Also, for the second emission in 1.4203 GHz, the emission is in a very
         noisy region so the continuum  subtraction won't be perfect, likely
```

```
    more noisy on higher frequencies since the continuum is selected in
    channels 780~1000:
uvcontsub(vis='cig96_13.corr.emission.ms', field='0', fitspw='
    0:0~510;710~1300')
# For the time-channel binned file, we subtract as follows:
uvcontsub(vis='cig96_13.corr.20s.10chan.ms', field='0', fitspw='
    0:45~93;110~181')
# For the whole spw 0 we use an as extended as possible continuum:
uvcontsub(vis='cig96_13.corr.spw0.ms', field='0', fitspw='
    0:300~365;396~460;490~920;1110~1520')

### Clean of the continuum subtracted data:
##########################################
# Weighting natural with the factor of 6.25064 for the channel smoothing
     that will be necessary to combine with VLA data:
clean(vis='cig96_13.cvel.corr.ms.contsub', imagename='cig96_13.cvel.corr
    .contsub.natural.line', field='0', spw='0:450~800', mode='frequency',
     start=450, nchan=351, niter=10000, width='48.830kHz', threshold='1.5
    mJy', interactive=T, npercycle=100, imsize=[200,200], phasecenter='',
     cell='8.0arcsec', restfreq='1.42040575177GHz', weighting='natural',
    usescratch=T)
# Weighting uniform:
clean(vis='cig96_13.corr.ms.contsub', imagename='cig96_13.corr.v3.
    contsub.uniform.line', field='0', spw='0:510~730', mode='channel',
    start=0, niter=10000, threshold='1.2mJy', interactive=T, npercycle
    =100, imsize=[200,200], phasecenter='', cell='15.0arcsec', restfreq='
    1.4204GHz', weighting='uniform', usescratch=T)
# Weighting Briggs rob=0.0:
clean(vis='cig96_13.corr.ms.contsub', imagename='cig96_13.corr.v3.
    contsub.rob0.0.line', field='0', spw='0:510~730', mode='channel',
    start=0, niter=10000, threshold='1.2mJy', interactive=T, npercycle
    =100, imsize=[200,200], phasecenter='', cell='15.0arcsec', restfreq='
    1.4204GHz', weighting='briggs', robust='0.0', usescratch=T)
# Computation of moments:
immoments(imagename='cig96_13.cvel.corr.contsub.natural.line.image',
    axis='spectral', moments=[0,1], outfile='cig96_13.cvel.corr.contsub.
    natural.line.image.mom')
# For the time-channel binned file, we clean as follows:
# Weighting natural:
```

```
170 clean(vis='cig96_13.corr.20s.10chan.ms.contsub', imagename='cig96_13.
    corr.20s.10chan.ms.contsub.natural.line.image', field='0', spw='
    0:93~110', mode='channel', start=0, niter=1000, threshold='1.2mJy',
    interactive=T, npercycle=100, imsize=[200,200], phasecenter='', cell=
    '15.0arcsec', restfreq='1.4204GHz', weighting='natural', usescratch=T
    )
171 # For the spw 0 split dataset:
172 clean(vis='cig96_13.corr.spw0.ms.contsub', imagename='cig96_13.corr.spw0
    .ms.contsub.natural.line', field='0', spw='0:920~1110', mode='channel
    ', start=920, nchan=190, niter=10000, threshold='1.2mJy', interactive
    =T, npercycle=100, imsize=[200,200], phasecenter='', cell='10.0arcsec
    ', restfreq='1.4204GHz', weighting='natural', usescratch=T)
173
174 ### Corrected data inspection via msview:
175 ##########################################
176 # We inspect the baselines that present solar interferences via msview
    and flag again
177 flagdata(vis='cig96_13.ms', mode='manual', field='1', spw='0', antenna='
    ea07;ea01;ea02;ea05;ea20')
178 # We flag the baselines that have shown interferences:
179 flagdata(vis='cig96_13.ms', mode='manual', field='1', spw='0', antenna='
    2&8;5&26;5&20;8&13;8&12;2&12', flagbackup=True)
180 # We now delete the calibration to perform it again with the new flagged
     data:
181 # To do so, we restart from the beginning, right after the flagging.
182 # After applying the whole calibration again, we split field = 3 (CIG96)
     re-calibrated data, in the spw=0:
183 split(vis='cig96_13.ms', datacolumn='corrected', outputvis='cig96_13.
    corr.v2.ms', field='3', spw='0:399~2047')
184 split(vis='cig96_13.ms', datacolumn='corrected', outputvis='cig96_13.
    corr.allfields.ms', field='1~3', spw='0')
185 # and redo the continuum subtraction:
186 uvcontsub(vis='cig96_13.corr.v2.ms', field='0', fitspw='0:0~510;730~1300
    ')
187 # Cleaning: weighting natural:
188 clean(vis='cig96_13.corr.v2.ms.contsub', imagename='cig96_13.corr.v2.
    contsub.natural.line', field='0', spw='0:510~730', mode='channel',
    start=0, niter=10000, threshold='1.2mJy', interactive=T, npercycle
    =100, imsize=[300,300], phasecenter='', cell='15.0arcsec', restfreq='
    1.4204GHz', weighting='natural', usescratch=T)
```

```
189
190 # ################## END
191
192 # # IN CASE YOU WISH TO RESET THE WHOLE CALIBRATION, TAKE THE FOLLOWING
        STEPS:
193 # #
194 # # clearcal(vis='xxx')
195 # #
196 # # flagdata(vis='xxx',mode=unflag)
197 # #
198 # # Ready to redo calibration!
```

Appendix B

Observing CIG 96 with VST: example of an observing block (OB)

On the reproducibility of the results and figures of this dissertation

With the aim of making the results and images presented in this thesis as accessible and reproducible as possible, we have created a GitHub repository named AMIGA deep-obs (release v0) (with doi:10.5281/zenodo.1295480). See Appendix A for further information.

The following is a complete observing block (OB) as submitted to VST−ESO to observe CIG 96. Qualitatively, the initial commands (lines 1 to 29) set the observation title, target information and main observational constraints. The acquisition template (indicated as `ACQUISITION.TEMPLATE.NAME "OMEGACAM_img_acq"`, lines 31 to 42) sets up the telescope in the original coordinates of the pointing, defined as `ra` and `dec` parameters (Right Ascension and Declination, lines 16 and 17) so the following observing

templates (indicated as `TEMPLATE.NAME "OMEGACAM_img_obs_offset"`, lines 44 to 51 and following templates) may start performing the observations in the correct position.

Taking the first observing template as an example, it applies first any offset in RA and DEC indicated by the parameters `TEL.TARG.OFFSETALPHA` (in arcsec, line 48) and `TEL.TARG.OFFSETDELTA` (in arcsec, line 49). Then, it performs the observation with the corresponding exposure time, indicated by the parameter `DET1.WIN1.UIT1` (in seconds, line 45). After this initial exposure is finished, a new template is executed. As in the first template, the telescope will apply the new corresponding offset in RA and DEC (lines 57 and 58) and perform a new observation of an exposure time (line 54). This process is only altered by the acquisition of an extra bias halfway through the OB to study the bias evolution throughout the night (lines 134 to 135). The remaining observing templates are finished afterwards.

Out of the 8 OBs dedicated to observe of CIG 96, the first seven have the exact same commands. The only difference between the first 7 and the 8^{th} and last OB is simply that the last performs a few less exposures than the previous, but there are no changes in the observing strategy, requirements or parameters of the OB. This and the rest of scripts for the OBs can be found in the AMIGA deep-obs GitHub.

```
1  IMPEX.VERSION "2.0"
2  name                          "CIG0096_1"
3  userComments                  ""
4  InstrumentComments            ""
5  userPriority                  "1"
6  type                          "O"
7  finding_chart_list            "cig0096.jpeg "
8
9  TARGET.NAME                   "CIG0096"
10 propRA                        "0.000000"
11 propDec                       "0.000000"
12 diffRA                        "0.000000"
13 diffDec                       "0.000000"
14 equinox                       "J2000"
15 epoch                         "2000.0"
16 ra                            " 02:15:27.640"
17 dec                           " 06:00:09.100"
```

```
18 objectClass                          "Unknown"
19
20 CONSTRAINT.SET.NAME                  "CIG0096"
21 seeing                               "2.0"
22 sky_transparency                     "Photometric"
23 air_mass                             "2.0"
24 fractional_lunar_illumination        "0.3"
25 moon_angular_distance                "60"
26 twilight                             "0"
27
28 OBSERVATION.DESCRIPTION.NAME "CIG0096"
29 instrument "OMEGACAM"
30
31 ACQUISITION.TEMPLATE.NAME "OMEGACAM_img_acq"
32 TEL.ROT.OFFANGLE   "0"
33 TEL.GS1.ALPHA      "0"
34 TEL.GS1.DELTA      "0"
35 TEL.GS1.MAG        "12"
36 TEL.GS2.ALPHA      "0"
37 TEL.GS2.DELTA      "0"
38 TEL.GS2.MAG        "12"
39 TEL.ADC.TYPE       "NONE"
40 INS.FILT.NAME      "r_SDSS"
41 OCS.AG.START       "F"
42 OCS.IA.START       "T"
43
44 TEMPLATE.NAME "OMEGACAM_img_obs_offset"
45 DET1.WIN1.UIT1              "154"
46 SEQ.NEXPO                   "1"
47 SEQ.RET2ORIG                "F"
48 TEL.TARG.OFFSETALPHA        "0.0"
49 TEL.TARG.OFFSETDELTA        "0.0"
50 INS.FILT.NAME               "r_SDSS"
51 OCS.STRTG                   "Deep"
52
53 TEMPLATE.NAME "OMEGACAM_img_obs_offset"
54 DET1.WIN1.UIT1              "154"
55 SEQ.NEXPO                   "1"
56 SEQ.RET2ORIG                "F"
57 TEL.TARG.OFFSETALPHA        "-37.8"
```

```
58 TEL.TARG.OFFSETDELTA       "45.61"
59 INS.FILT.NAME              "r_SDSS"
60 OCS.STRTG                  "Deep"
61
62 TEMPLATE.NAME "OMEGACAM_img_obs_offset"
63 DET1.WIN1.UIT1             "154"
64 SEQ.NEXPO                  "1"
65 SEQ.RET2ORIG               "F"
66 TEL.TARG.OFFSETALPHA       "680.9"
67 TEL.TARG.OFFSETDELTA       "523.3"
68 INS.FILT.NAME              "r_SDSS"
69 OCS.STRTG                  "Deep"
70
71 TEMPLATE.NAME "OMEGACAM_img_obs_offset"
72 DET1.WIN1.UIT1             "154"
73 SEQ.NEXPO                  "1"
74 SEQ.RET2ORIG               "F"
75 TEL.TARG.OFFSETALPHA       "-72.1"
76 TEL.TARG.OFFSETDELTA       "112.2"
77 INS.FILT.NAME              "r_SDSS"
78 OCS.STRTG                  "Deep"
79
80 TEMPLATE.NAME "OMEGACAM_img_obs_offset"
81 DET1.WIN1.UIT1             "154"
82 SEQ.NEXPO                  "1"
83 SEQ.RET2ORIG               "F"
84 TEL.TARG.OFFSETALPHA       "1389.3"
85 TEL.TARG.OFFSETDELTA       "-14.4"
86 INS.FILT.NAME              "r_SDSS"
87 OCS.STRTG                  "Deep"
88
89 TEMPLATE.NAME "OMEGACAM_img_obs_offset"
90 DET1.WIN1.UIT1             "154"
91 SEQ.NEXPO                  "1"
92 SEQ.RET2ORIG               "F"
93 TEL.TARG.OFFSETALPHA       "-43.2"
94 TEL.TARG.OFFSETDELTA       "87.0"
95 INS.FILT.NAME              "r_SDSS"
96 OCS.STRTG                  "Deep"
97
```

```
 98 TEMPLATE.NAME "OMEGACAM_img_obs_offset"
 99 DET1.WIN1.UIT1              "154"
100 SEQ.NEXPO                   "1"
101 SEQ.RET2ORIG                "F"
102 TEL.TARG.OFFSETALPHA        "340.7"
103 TEL.TARG.OFFSETDELTA        "-673.9"
104 INS.FILT.NAME               "r_SDSS"
105 OCS.STRTG                   "Deep"
106
107 TEMPLATE.NAME "OMEGACAM_img_obs_offset"
108 DET1.WIN1.UIT1              "154"
109 SEQ.NEXPO                   "1"
110 SEQ.RET2ORIG                "F"
111 TEL.TARG.OFFSETALPHA        "39.6"
112 TEL.TARG.OFFSETDELTA        "-94.2"
113 INS.FILT.NAME               "r_SDSS"
114 OCS.STRTG                   "Deep"
115
116 TEMPLATE.NAME "OMEGACAM_img_obs_offset"
117 DET1.WIN1.UIT1              "154"
118 SEQ.NEXPO                   "1"
119 SEQ.RET2ORIG                "F"
120 TEL.TARG.OFFSETALPHA        "-728.2"
121 TEL.TARG.OFFSETDELTA        "-471.0"
122 INS.FILT.NAME               "r_SDSS"
123 OCS.STRTG                   "Deep"
124
125 TEMPLATE.NAME "OMEGACAM_img_obs_offset"
126 DET1.WIN1.UIT1              "154"
127 SEQ.NEXPO                   "1"
128 SEQ.RET2ORIG                "F"
129 TEL.TARG.OFFSETALPHA        "-1.69"
130 TEL.TARG.OFFSETDELTA        "92.4"
131 INS.FILT.NAME               "r_SDSS"
132 OCS.STRTG                   "Deep"
133
134 TEMPLATE.NAME "OMEGACAM_img_cal_bias"
135 SEQ.NEXPO                  "1"
136
137 TEMPLATE.NAME "OMEGACAM_img_obs_offset"
```

```
138 DET1.WIN1.UIT1              "154"
139 SEQ.NEXPO                   "1"
140 SEQ.RET2ORIG                "F"
141 TEL.TARG.OFFSETALPHA        "-576.5"
142 TEL.TARG.OFFSETDELTA        "-679.6"
143 INS.FILT.NAME               "r_SDSS"
144 OCS.STRTG                   "Deep"
145
146 TEMPLATE.NAME "OMEGACAM_img_obs_offset"
147 DET1.WIN1.UIT1              "154"
148 SEQ.NEXPO                   "1"
149 SEQ.RET2ORIG                "F"
150 TEL.TARG.OFFSETALPHA        "46.8"
151 TEL.TARG.OFFSETDELTA        "-110.4"
152 INS.FILT.NAME               "r_SDSS"
153 OCS.STRTG                   "Deep"
154
155 TEMPLATE.NAME "OMEGACAM_img_obs_offset"
156 DET1.WIN1.UIT1              "154"
157 SEQ.NEXPO                   "1"
158 SEQ.RET2ORIG                "F"
159 TEL.TARG.OFFSETALPHA        "-538.8"
160 TEL.TARG.OFFSETDELTA        "-789.7"
161 INS.FILT.NAME               "r_SDSS"
162 OCS.STRTG                   "Deep"
163
164 TEMPLATE.NAME "OMEGACAM_img_obs_offset"
165 DET1.WIN1.UIT1              "154"
166 SEQ.NEXPO                   "1"
167 SEQ.RET2ORIG                "F"
168 TEL.TARG.OFFSETALPHA        "-39.6"
169 TEL.TARG.OFFSETDELTA        "116.7"
170 INS.FILT.NAME               "r_SDSS"
171 OCS.STRTG                   "Deep"
172
173 TEMPLATE.NAME "OMEGACAM_img_obs_offset"
174 DET1.WIN1.UIT1              "154"
175 SEQ.NEXPO                   "1"
176 SEQ.RET2ORIG                "F"
177 TEL.TARG.OFFSETALPHA        "1274.0"
```

```
178 TEL.TARG.OFFSETDELTA        "192.9"
179 INS.FILT.NAME               "r_SDSS"
180 OCS.STRTG                   "Deep"
181
182 TEMPLATE.NAME "OMEGACAM_img_obs_offset"
183 DET1.WIN1.UIT1              "154"
184 SEQ.NEXPO                   "1"
185 SEQ.RET2ORIG                "F"
186 TEL.TARG.OFFSETALPHA        "64.9"
187 TEL.TARG.OFFSETDELTA        "-101.4"
188 INS.FILT.NAME               "r_SDSS"
189 OCS.STRTG                   "Deep"
```

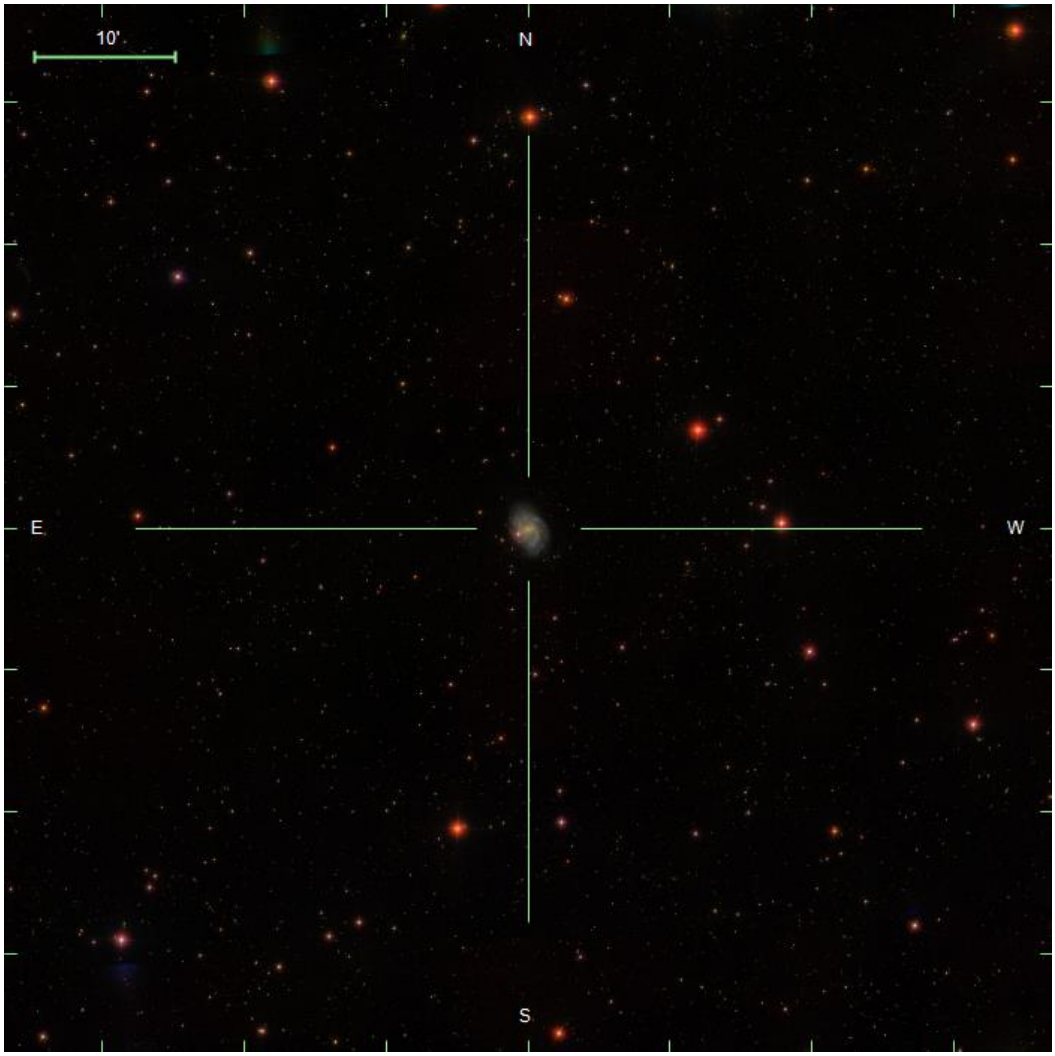

Fig. B.1 Finding chart image of CIG 96 (extracted from SDSS Navigate tool) submitted along with the OB to confirm the position and the approximate expected field of view.

Appendix C

Reduction and calibration steps with Astro-WISE

On the reproducibility of the results and figures of this dissertation

With the aim of making the results and images presented in this thesis as accessible and reproducible as possible, we have created a GitHub repository named AMIGA deep-obs (release v0) (with doi:10.5281/zenodo.1295480). See Appendix A for further information.

As indicated in Sect. 3.2.1.3, we used a modified version (Venhola et al., 2017) of Astro-WISE pipeline (Valentijn et al., 2007) to reduce and calibrate the VST data of CIG 96. The following is the complete script (in Python environment) used for this purpose. It is divided in the next ordered tasks: data acquisition, target selection and modified environment for the reduction (lines 1 to 12), calibration of all the nights with available data (lines 13 to 117), tasks for the background subtraction, reduction, astrometry calculation and regridding (lines 119 to 131), frames visualisation and inspection (lines 133 to 139), selection of good frames (lines 141 to 146), co−addition

of all images to create the final image (lines 148 to 150), final image retrieval (lines 152 to 155) and image download steps (lines 157 to end). This and the rest of reduction and calibration scripts can be found in the AMIGA deep-obs GitHub.

```
1  # SET PROJECT, PRIVILEGES AND IMPORT NECESSARY FEEDING FUNCTIONS
2
3  context.set_project('AMIGADEEP')
4  context.set_privileges(2)
5  exec(open('/data/users/ramirez/support_scripts/singlejobsender3.py').
       read())
6  exec(open('/data/users/ramirez/support_scripts/select_frames3.py').
       read())
7
8  # CIG96 DATA
9
10 target = 'CIG0096'
11 cigra, cigdec = 33.8, 6.0
12
13 # PHOTOMETRY FOR ALL NIGHTS
14
15 # NIGHT 1
16
17 date_start, date_end = [datetime.datetime(2016, 10, 6), datetime.
       datetime(2016, 10, 7)]
18 date_query = ((RawScienceFrame.DATE_OBS>date_start)&(RawScienceFrame.
       DATE_OBS<date_end)&(RawScienceFrame.OBJECT=='STD,ZEROPOINT'))
19 len(date_query)
20 names = [i.filename for i in date_query]
21 len(names)
22 singlejobsender('Reduce', names, cigra, cigdec)
23 query = ((ReducedScienceFrame.creation_date>datetime.date.today())&(
       ReducedScienceFrame.OBJECT=='STD,ZEROPOINT'))
24 names=[i.filename for i in query]
25 singlejobsender('Astrometry', names, cigra, cigdec)
26 singlejobsender('Photom', names, cigra, cigdec)
27
28 # NIGHT 2
29
```

```
30 date_start, date_end = [datetime.datetime(2016, 10, 9), datetime.
       datetime(2016, 10, 10)]
31 date_query = ((RawScienceFrame.DATE_OBS>date_start)&(RawScienceFrame.
       DATE_OBS<date_end)&(RawScienceFrame.OBJECT=='STD,ZEROPOINT'))
32 len(date_query)
33 names = [i.filename for i in date_query]
34 len(names)
35 singlejobsender('Reduce', names, cigra, cigdec)
36 query = ((ReducedScienceFrame.creation_date>datetime.date.today())&(
       ReducedScienceFrame.OBJECT=='STD,ZEROPOINT'))
37 names=[i.filename for i in query]
38 singlejobsender('Astrometry', names, cigra, cigdec)
39 singlejobsender('Photom', names, cigra, cigdec)
40
41 # NIGHT 3
42
43 date_start, date_end = [datetime.datetime(2016, 10, 20), datetime.
       datetime(2016, 10, 21)]
44 date_query = ((RawScienceFrame.DATE_OBS>date_start)&(RawScienceFrame.
       DATE_OBS<date_end)&(RawScienceFrame.OBJECT=='STD,ZEROPOINT'))
45 len(date_query)
46 names = [i.filename for i in date_query]
47 len(names)
48 singlejobsender('Reduce', names, cigra, cigdec)
49 query = ((ReducedScienceFrame.creation_date>datetime.date.today())&(
       ReducedScienceFrame.OBJECT=='STD,ZEROPOINT'))
50 names=[i.filename for i in query]
51 singlejobsender('Astrometry', names, cigra, cigdec)
52 singlejobsender('Photom', names, cigra, cigdec)
53
54 # NIGHT 4
55
56 date_start, date_end = [datetime.datetime(2016, 11, 1), datetime.
       datetime(2016, 11, 2)]
57 date_query = ((RawScienceFrame.DATE_OBS>date_start)&(RawScienceFrame.
       DATE_OBS<date_end)&(RawScienceFrame.OBJECT=='STD,ZEROPOINT'))
58 len(date_query)
59 names = [i.filename for i in date_query]
60 len(names)
61 singlejobsender('Reduce', names, cigra, cigdec)
```

```
62 query = ((ReducedScienceFrame.creation_date>datetime.date.today())&(
       ReducedScienceFrame.OBJECT=='STD,ZEROPOINT'))
63 names=[i.filename for i in query]
64 singlejobsender('Astrometry', names, cigra, cigdec)
65 singlejobsender('Photom', names, cigra, cigdec)
66
67 # NIGHT 5
68
69 date_start, date_end = [datetime.datetime(2016, 11, 2), datetime.
       datetime(2016, 11, 3)]
70 date_query = ((RawScienceFrame.DATE_OBS>date_start)&(RawScienceFrame.
       DATE_OBS<date_end)&(RawScienceFrame.OBJECT=='STD,ZEROPOINT'))
71 len(date_query)
72 names = [i.filename for i in date_query]
73 len(names)
74 singlejobsender('Reduce', names, cigra, cigdec)
75 query = ((ReducedScienceFrame.creation_date>datetime.date.today())&(
       ReducedScienceFrame.OBJECT=='STD,ZEROPOINT'))
76 names=[i.filename for i in query]
77 singlejobsender('Astrometry', names, cigra, cigdec)
78 singlejobsender('Photom', names, cigra, cigdec)
79
80 # NIGHT 6
81
82 date_start, date_end = [datetime.datetime(2016, 12, 2), datetime.
       datetime(2016, 12, 3)]
83 date_query = ((RawScienceFrame.DATE_OBS>date_start)&(RawScienceFrame.
       DATE_OBS<date_end)&(RawScienceFrame.OBJECT=='STD,ZEROPOINT'))
84 len(date_query)
85 names = [i.filename for i in date_query]
86 len(names)
87 singlejobsender('Reduce', names, cigra, cigdec)
88 query = ((ReducedScienceFrame.creation_date>datetime.date.today())&(
       ReducedScienceFrame.OBJECT=='STD,ZEROPOINT'))
89 names=[i.filename for i in query]
90 singlejobsender('Astrometry', names, cigra, cigdec)
91 singlejobsender('Photom', names, cigra, cigdec)
92
93 # NIGHT 7
94
```

```
95  date_start, date_end = [datetime.datetime(2016, 12, 3),  datetime.
        datetime(2016, 12, 4)]
96  date_query = ((RawScienceFrame.DATE_OBS>date_start)&(RawScienceFrame.
        DATE_OBS<date_end)&(RawScienceFrame.OBJECT=='STD,ZEROPOINT'))
97  len(date_query)
98  names = [i.filename for i in date_query]
99  len(names)
100 singlejobsender('Reduce', names, cigra, cigdec)
101 query = ((ReducedScienceFrame.creation_date>datetime.date.today())&(
        ReducedScienceFrame.OBJECT=='STD,ZEROPOINT'))
102 names=[i.filename for i in query]
103 singlejobsender('Astrometry', names, cigra, cigdec)
104 singlejobsender('Photom', names, cigra, cigdec)
105
106 # NIGHT 8
107
108 date_start, date_end = [datetime.datetime(2016, 12, 20), datetime.
        datetime(2016, 12, 21)]
109 date_query = ((RawScienceFrame.DATE_OBS>date_start)&(RawScienceFrame.
        DATE_OBS<date_end)&(RawScienceFrame.OBJECT=='STD,ZEROPOINT'))
110 len(date_query)
111 names = [i.filename for i in date_query]
112 len(names)
113 singlejobsender('Reduce', names, cigra, cigdec)
114 query = ((ReducedScienceFrame.creation_date>datetime.date.today())&(
        ReducedScienceFrame.OBJECT=='STD,ZEROPOINT'))
115 names=[i.filename for i in query]
116 singlejobsender('Astrometry', names, cigra, cigdec)
117 singlejobsender('Photom', names, cigra, cigdec)
118
119 # REDUCTION
120
121 query_raw = (RawScienceFrame.OBJECT==target)
122 names=[i.filename for i in query_raw]
123 len(names)
124 singlejobsender('Background', names, cigra, cigdec)
125 # if it gets stuck, rerun singlejobsender from the frame where it
        stopped, e.g. 16:
126 #   singlejobsender('Background',names[16*32:],cigra,cigdec)
127 singlejobsender('Reduce', names, cigra, cigdec)
```

```
128 query_red = select_frames('ReducedScienceFrame', 'OCAM_r_SDSS', cigra
    -0.8, cigra+0.8, cigdec-0.8, cigdec+0.8)
129 names=[i.filename for i in query_red]
130 singlejobsender('Astrometry', names, cigra, cigdec)
131 singlejobsender('Regrid', names, cigra, cigdec)
132
133 # FRAMES VISUALIZATION
134
135 psf = [i.psf_radius for i in query_red]
136 import matplotlib.pyplot as plt
137 plt.hist(psf)
138 medians = [i.imstat.median for i in query_red]
139 plt.hist(medians)
140
141 # GOOD FRAMES SELECTION
142
143 query_all = select_frames('RegriddedFrame','OCAM_r_SDSS', cigra-0.8,
    cigra+0.8, cigdec-0.8, cigdec+0.8)   # all files within 0.8 deg
    radius from the specified coordinates
144 goodseeing = [ ]
145 for i in query_all:
146       if i.psf_radius < 1.2:goodseeing.append(i.filename)   # selects
    only those with seeing below value
147
148 # CO-ADDITION
149
150 dpu.run('Coadd', instrument='OMEGACAM',reg_filenames=goodseeing,
    dpu_aweversion='current', dpu_time = 8*60*60, C=1)
151
152 # FINAL IMAGE
153
154 query_final = (CoaddedRegriddedFrame.OBJECT==target).project_only().
    max('creation_date')
155 query_final.retrieve()
156
157 # DOWNLOAD LINK
158
159 import urllib
160 url = 'http://%s:%s/%s' % (Env['data_server'], Env['data_port'],
    urllib.parse.quote(query_final.filename))
```

```
161 print(url)
```